

Physical Approaches to Cytoskeletal Self-Organization

Dissertation

zur Erlangung des Grades
des Doktors der Naturwissenschaften
der Naturwissenschaftlich-Technischen Fakultät II
–Physik und Mechatronik–
der Universität des Saarlandes

von
Konstantin Doubrovinski

Saarbrücken
2008

Tag des Kolloquiums:

Dekan:

Mitglieder des
Prüfungsausschusses:

Abstract

Two properties of the living cells distinguish them most profoundly from non-living entities: the ability to reproduce and the ability to move. To a large extent, these processes rely on the cytoskeleton - an network of filamentous polymers, that in cells is constantly kept out of thermodynamic equilibrium. Three types of biopolymers constitute the cytoskeleton: microtubules, actin filaments and intermediate filaments. The dynamics of the biopolymers can be regulated by a number of proteins, including molecular motors, which are distinguished by their ability to transform chemical energy into mechanical work. This can be exploited to induce stresses in the meshwork and to transport cargoes, such as cellular organelles, along the cytoskeletal filaments.

A large body of recent experimental evidence indicates that cytoskeleton accomplishes its various biological tasks through self-organization, i.e. internal organization of a system, arising from simple short-range interactions of many identical system constituents. For example, mixtures of purified microtubules and molecular motors in aqueous solutions have been seen to form asters, reminiscent of certain cellular organelles. Another example comes from experiments where certain motile cells were fragmented into pieces that retained the ability to crawl on a substrate. This indicates that cell locomotion arises through local interactions of cytoskeletal constituents and is unlikely to rely on a single organizing unit.

Mesoscopic mean-field descriptions have been applied to study the cytoskeletal pattern formation. This method has a number of strengths: its wide applicability and generality as well as the ability to straightforwardly account for experimentally determined details of molecule structures and interactions. However, when applying mesoscopic mean-field equations to study the cytoskeleton, one is confronted with the following problems. (a) Equations, describing particles with many degrees of freedom are hard to analyze. (b) As cytoskeletal filaments are spatially extended, equations, describing their dynamics are generically non-local. (c) Dealing with the boundary conditions is not straightforward.

In this thesis we develop mesoscopic mean-field descriptions of the cytoskeleton, introducing novel techniques for dealing with the above-mentioned problems. Firstly, we develop a general formalism that allows to explicitly account for dynamic filament length. Within this formalism, we identify a class of systems that admit exact treatment. Then, we introduce an approximation, consisting of moment-expansion, combined with coarse-graining, that

allows to apply our formalism to a broader class of systems. We demonstrate that the results obtained with this approximation agree with those of the exact treatment, provided that cytoskeletal filaments, constituting the pattern, are much shorter than the characteristic scale of the pattern. We apply our methods to describe two biological systems: microtubule organization in fish skin cells and actin wave-dynamics in granulocytes. Finally, we introduce a novel phase-field-like approach for treating interactions of filaments with a boundary. We apply our method to cell locomotion, demonstrating that our equations, describing actin dynamics in granulocytes, exhibit states, reminiscent of those of a motile cells, when combined with moving boundaries.

Zusammenfassung

Zwei Eigenschaften lebender Zellen unterscheiden sie fundamental von unbelebter Materie: Die Fähigkeit sich zu reproduzieren und sich zu bewegen. In einem großen Maße beruhen die beiden Prozesse auf dem Zytoskelett - einem intrazellulären Netzwerk fingerförmiger Polymere, welches beständig aus dem thermodynamischen Gleichgewicht getrieben wird. Das Zytoskelett besteht aus drei Arten von Biopolymeren: Mikrotubuli, Aktin-Filamenten und intermediären Filamenten. Die Dynamik dieser Biopolymere kann von einer Vielzahl von Proteinen reguliert werden. Unter diesen befinden sich insbesondere molekulare Motoren, welche chemische Energie in mechanische Arbeit umwandeln können. Diese kann genutzt werden, um im Filamentnetzwerk Spannungen zu erzeugen oder Lasten entlang von Filamenten zu transportieren, zum Beispiel zelluläre Organellen.

Eine Vielzahl experimenteller Ergebnisse der letzten Jahre deuten darauf hin, dass in vielen wichtigen zellulären Prozessen die Selbstorganisation von Komponenten des Zytoskeletts eine zentrale Rolle spielt. Bei der Selbstorganisation werden die Strukturen eines Systems durch einfache, kurzreichweitige Wechselwirkungen vieler identischer Konstituenten erzeugt. Zum Beispiel ordnen sich aufgereinigte Mikrotubuli und molekulare Motoren *in vitro* ähnlich zu zellulären Strukturen sternförmig an. Ein weiteres Beispiel liefern Experimente an Fragmenten motiler Zellen, die die Fähigkeit, sich auf Oberflächen fortzubewegen, beibehalten. Diese Fragmente haben keinen Kern, der als zentrale organisierende Einheit dienen könnte, so dass Zellfortbewegung allein durch lokale Wechselwirkungen von Zytoskelett-Komponenten entstehen kann.

Molekularfeldbeschreibungen der Dynamik auf mesoskopischen Skalen bilden einen vielversprechenden Ansatz, um physikalische Aspekte der Musterbildung im Zytoskelett zu untersuchen. Die Stärken dieses Zugangs liegen in ihrer weitreichenden Anwendbarkeit und der Möglichkeit, experimentell bestimmte Details molekularer Strukturen und Wechselwirkungen in die Beschreibung einzubeziehen. Bei der Analyse der entsprechenden dynamischen Gleichungen treten allerdings einige Probleme auf: a) Die Gleichungen beschreiben Teilchen mit vielen Freiheitsgraden und sind deshalb numerisch praktisch nicht lösbar. b) Da die Filamente des Zytoskeletts räumlich ausgedehnt sind, sind die Gleichungen nicht-lokal. c) Die Behandlung nichtperiodischer Randbedingungen ist nicht offensichtlich.

In der vorliegenden Arbeit entwickeln und analysieren wir mesoskopis-

che Molekularfeldbeschreibungen des Zytoskeletts. Dabei werden neue Techniken eingeführt, welche die Probleme (a), (b) und (c) lösen. Wir entwickeln einen Formalismus, der es erlaubt Systeme aus Filamenten mit veränderlichen Längen zu beschreiben. Wir bestimmen eine Klasse von Systemen, die eine Analyse der exakten Gleichungen erlaubt. Durch Einführung einer Entwicklung nach Momenten zusammen mit einer grobkörnigen Beschreibung machen wir auch Systeme außerhalb dieser Klasse einer Analyse zugänglich. Wir zeigen, dass die Näherung mit der exakten Lösung übereinstimmt, wenn die mittlere Länge der Filamenten viel kleiner ist, als die charakteristische Größe der Muster, die sie bilden. Wir wenden unsere Methode zur Beschreibung der Mikrotubuli-Organisation in Melanophoren von Fischen und der Dynamik von Aktinwellen in Granulozyten. Schließlich stellen wir eine neue Phasenfeld-Methode vor, um die Wechselwirkung von Filamenten mit Membranen zu beschreiben. Wir wenden diese Methode zur Beschreibung der Zellfortbewegung an und zeigen, dass die Gleichungen, welche die Aktin-Dynamik in Granulozyten beschreiben, Lösungen haben, die stark an kriechende Zellen erinnern.

Contents

1	Self-organization: general aspects	9
2	The cytoskeleton	12
2.1	Cytoskeletal filaments	13
2.1.1	Actin	13
2.1.2	Microtubules	14
2.2	Motor proteins	15
2.2.1	Myosins	16
2.2.2	Kinesins	17
2.2.3	Dyneins	19
2.3	Cytoskeleton associated proteins	19
3	Self-organized structures in the cytoskeleton	21
3.1	Motor-filament <i>in vitro</i> assays	21
3.2	Melanophore fragments	22
3.3	Keratocyte fragments	24
3.4	Actin waves in <i>Dictyostelium discoideum</i>	25
3.5	Actin waves in neutrophils	27
4	Physical approaches to cytoskeletal pattern formation	29
4.1	Molecular dynamics	29
4.2	Mean field mesoscopic descriptions	30
4.2.1	Force balance	31
4.2.2	Boltzmann equations	33
4.3	Phenomenological descriptions	36
4.3.1	Symmetry-based phenomenological descriptions	36
4.3.2	Hydrodynamics	38
5	Dynamics of treadmilling filaments, regulated by actively transported nucleator proteins	41
5.1	Simplified description: constant filament length	41
5.1.1	Dynamic equations	41
5.1.2	Results	44
5.2	Varying length distributions: exact treatment	48
5.2.1	Dynamics of filament length	48
5.2.2	Including space dependence	49

5.2.3	Exact treatment	50
5.2.4	Results	51
5.3	Moment expansion	54
5.3.1	Results	55
5.4	Capping proteins	60
5.5	Varying domain shape	64
5.6	Conclusions and outlook	68
6	Filament treadmilling in presence of cooperatively binding nucleators	70
6.1	Exact treatment	70
6.2	Coarse-grained description	75
6.3	Filaments in a confined domain	79
6.4	Membranous boundary	82
7	Conclusions and outlook	87
A	Dynamic equations for the hierarchy of order parameters	92
B	Aster solution in the limit of zero nucleator diffusion	93
C	Boundary conditions for describing melanophore fragments	94
D	Force balance at a (moving) coarse grained boundary	95
E	Integrating the membrane dynamics	99
E.1	Force density at the boundary	99
E.2	Three subroutines	104
E.2.1	Subroutine <i>closest_distance</i>	104
E.2.2	Subroutine <i>remesh</i>	104
E.2.3	Subroutine <i>shift</i>	105
E.3	The algorithm	106

1 Self-organization: general aspects

The term self-organization refers to phenomena when a system consisting of many identical subsystems ("agents") interacting according to some simple rules exhibits complex behavior which can not be straightforwardly traced back to that of constituent subsystems. A common way of paraphrasing this is stating that the whole is more than a sum of its parts. This concept is traditionally illustrated by the Belousov-Zhabotinsky (BZ) reaction [4, 92]. Quite amazingly, just like many phenomena to be considered in this thesis, the BZ reaction was discovered in the process of developing a biomimetic assay, namely in an attempt of B.P. Belousov to design a simple laboratory version of the citric acid cycle. When mixing citric acid and sulphuric acid together with potassium bromate and iron salt in water a spectacular spiral wave pattern sets in (see Fig. 1).

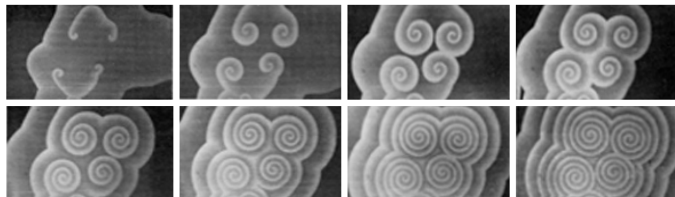


Figure 1: Spiral wave pattern in Belousov-Zhabotinsky reaction. Taken from [93].

Interactions of individual particles ("agents") in a reaction mixture are governed by simple chemical kinetics and diffusion. However, despite the wave-pattern being entirely determined by short-range particle interaction, their detailed knowledge *per se* does not explain the pattern. In fact, understanding spiral waves requires describing ensembles of large number of interacting particles. Other examples of self-organized structures are Rayleigh-Benard convection rolls (a flow pattern, observed in a fluid layer, subjected to temperature gradient) [5, 66], two-dimensional localized excitations in vibrated sand, called oscillons [83], and phase-transitions in liquid crystals [12, 61].

Applicability of the concept of self-organization goes far beyond physics or chemistry. In fact, the idea of self-organization was recognized by philosophers and writers centuries before it started to make its way into the natural

sciences. It seems that the first statement of this principle dates back to the 1790s and is due to Immanuel Kant, who was the first to define life as "self-organized" and "self-reproducing" [36]. Interestingly, the idea of self-organization is central in L. Tolstoy's "War and Peace", where he aimed to comprehend how a country withstands an invasion, using the example of the French-Russian war of 1812. In one of the last novel chapters Tolstoy states: "The movement of nations is caused not by power, nor by intellectual activity, nor even by a combination of the two as historians have supposed, but by the activity of all the people who participate in the events". In other words, the properties of a social systems are due to interactions of all individuals, rather than due to particular decisions of some, i.e. social systems are self-organized.

One of the first applications of self-organization in biology is due to Peter Kropotkin (most known as one of the major ideologist of Russian anarchism). In his book "Mutual Aid: A Factor of Evolution" [41], which was largely influenced by Darwin's ideas, he points out that understanding evolutionary benefit of organizing into communities requires considering self-organized properties of populations. Herewith, it is easily appreciated how ideas of self-organization inspired the ideology of anarchism: much like animal communities, human society might best develop when based on free cooperation among individuals (i.e. self-organization) rather than when ruled by a centralized government.

In the context of using self-organization to explain biological phenomena it is interesting to mention the work of Hans Driesch who devoted his research to explaining development in terms of physical laws. To this end he brought traditional methods of physics into development: instead of exclusively making observations, he started to alter developmental systems (embryos) and to monitor the system's response. In classical experiments in 1895, he fragmented a four-cell sea urchin embryo into two two-cell portions, expecting to observe each portion develop into the part of larva, originating from the respective cell pair in an intact embryo. Strikingly, every cell pair gave rise to pretty normal sea urchin larva. The interpretation of Driesch's experiment requires realizing that the developments of each of the embryo's cells (blastomers) is determined by its interactions with surrounding blastomers, i.e., the development is self-organized (more than the sum of its parts!). However, in the late 19th century the idea of self-organization had not yet made its way into biological sciences and Driesch's experiment was at his time considered to support vitalism. According to vitalism, biological processes in general

and development, in particular, can not be explained in terms of physics and are due to extranatural forces. Indeed, since the development of an embryo proceeds to completion fairly normally despite dramatic alterations introduced by embryologist, it might in fact seem to be guided by some "force", whose nature lies beyond the scope of physics. This example illustrates the bewildering dissimilarity of self-organized phenomena with those, more conventionally considered in the area of physics. So dissimilar they are that the properties of the former have occasionally been attributed to supernatural forces!

In the 20th century, the physics of self-organization received considerable attention, noticeably through the works of I. Prigogine and A. Turing. In particular, Prigogine's work resolved a paradox associated with the existence of oscillating reactions, which in fact long prevented acceptance of Belousov's "supposedly discovered discovery" [64]. Indeed, the second law of thermodynamics implies that, at given conditions, a chemical reaction proceeds in only one direction. At first sight, an oscillating reaction would seem to change its direction with time. This is, however, not so. Whereas concentrations of some solutes in the BZ reaction oscillate in time, others undergo net consumption. Hence, stable oscillation can only be sustained in presence of continuous flux of matter through the system. In 1952, A. Turing (most known as logician, computer scientist and cryptographer) published "The Chemical Basis of Morphogenesis" [82] introducing the idea that spatio-temporal structures generated by similar mechanism as those of the BZ-reaction could be the basis of morphogenesis, as has by now been confirmed by, for example, investigations of vertebrate segmentation (see e.g. Refs. [31, 60]), as well as by investigations of pattern formation in the sea shells of molluscs [53].

The aim of this thesis is to develop theoretical tools, allowing to study self-organized phenomena on subcellular scale, in particular involving the cytoskeleton. The cytoskeleton is an intracellular meshwork of filamentous proteins allowing cells to divide, to move and to organize intracellular transport and must be maintained out of thermodynamic equilibrium in order to fulfill its biological tasks. A short summary of self-organization in the cytoskeleton will be presented below. However, first, a brief introduction to the cytoskeleton is given.

2 The cytoskeleton

Two properties of living cells distinguish them most profoundly from non-living entities: autopoiesis, i.e. the ability of cells to reproduce, and directional motion. These two processes rely heavily on the cytoskeleton [1, 8, 30], see Fig. 2, a meshwork of biopolymers. Three types of biopolymers constitute the cytoskeleton: microtubules, actin filaments, and intermediate filaments. During cell division microtubules make up the mitotic spindle - a structure which segregates chromosomes during mitosis and directs intracellular transport of organelles. Swimming of eukaryotes is driven by flagella that are built around a microtubular structure. Actin is the major constituent of the cell cortex - a crosslinked meshwork localized beneath the cell membrane that determines the cell shape. The migration of cells on substrates is largely determined by the dynamics of the cell cortex. Upon completion of mitosis, cells are pinched in two by a constricting ring of actin filaments encircling the cell. The third type of cytoskeletal filaments, intermediate filaments, are not dynamic, and do not play an active role during cell division and locomotion.

The complex tasks accomplished by cytoskeletal rearrangements require thorough regulation of dynamics of cytoskeletal filaments. For this purpose, cells possess an arsenal of proteins that are capable of binding cytoskeletal filaments and altering their dynamics in a variety of ways. Amongst these, motor proteins are distinguished for their remarkable ability to transform the chemical energy stored in an energy-rich bond of adenosine triphosphate (ATP, the universal "energy currency" of the cell) into mechanical work. This can be exploited for transporting cargos, e.g., organelles, along filaments and to induce stresses in biopolymer network by displacing filaments relatively to each other. Other proteins cross-link filaments or effect filament assembly and disassembly. In the following, cytoskeletal filaments and associated proteins will be described in more detail.

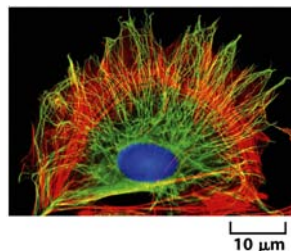


Figure 2: A cell in culture has been fixed and labeled to show two of the major cytoskeletal components, microtubules (in green) and actin filaments (in red). The DNA in the nucleus is labeled in blue. Taken from [1].

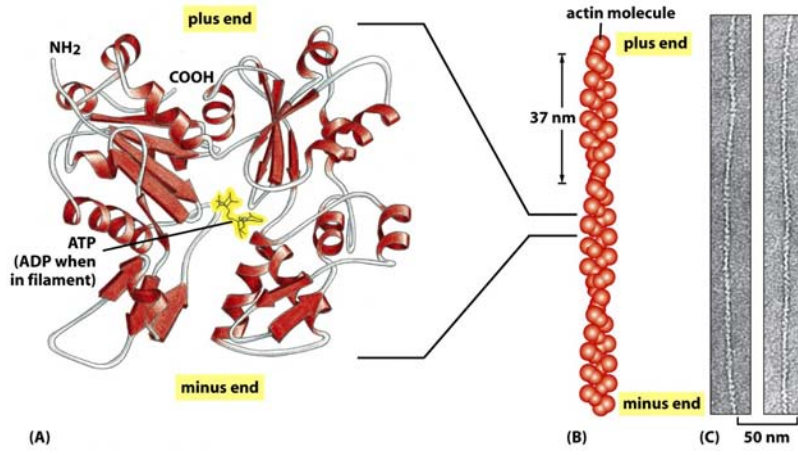


Figure 3: The structures of an actin monomer and an actin filament. (a) Ribbon model of an actin monomer with a nucleotide in its deep cleft. (b) Arrangement of monomers in a filament. (c) Electron micrograph of negatively stained actin filaments. Taken from [1].

2.1 Cytoskeletal filaments

2.1.1 Actin

Actin is a 42 kDa globular protein with a nucleotide binding site in the center of the molecule. In fact, it is the most abundant protein of eukaryotic cells. Actin monomers can polymerize into 7 nm thick filaments which can be described as two distinct protofilaments interwoven into a helix with a pitch of 37 nm, see Fig. 3. The stiffness of filaments can be characterized by the persistence length L_p , which is defined by $\langle \cos(\Delta\theta) \rangle = \exp(-s/L_p)$, where $\Delta\theta$ is the angle between tangent vectors to the polymer chain at points that are distance s apart. The distance s is measured along the chain and angle brackets indicate ensemble average. The persistence length of actin filaments is 15-17 μm [25, 62, 34].

Filament growth initiates upon formation of a nucleus of three monomers. Monomers get incorporated into a growing chain in ATP form, undergoing subsequent hydrolysis upon incorporation into the elongating chain. Actin molecule possesses no symmetry plane. Hence it can be endowed with orientation. All monomers in a polymer chain have the same orientation (polarity), thereby defining polarity of a filament. Hence, an actin filament has

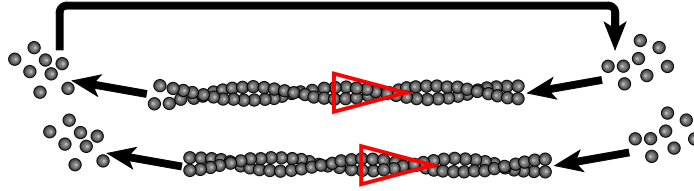


Figure 4: Schematic illustration of treadmilling dynamics. At the filament minus-end, subunits disassociate, replenishing the monomer pool, and re-incorporate at the plus-end. In this way, a filament undergoes effective translation, without displacement of its subunits.

two structurally distinguishable ends. The net polymerization rate (difference of rates of subunit incorporation and removal) may be different at the two filament ends, since polymerization is coupled to ATP hydrolysis. The faster growing end is conventionally referred to as the plus or barbed end and the shrinking end as the minus or pointed end. The difference between the polymerization rates at the two ends may lead to treadmilling. In this case, the filament grows at the plus-end and shrinks at the minus-end, which leads to an effective filament movement without displacement of its constituents, see Fig. 4.

If a polymerizing filament end encounters an obstacle, a force whose magnitude can be derived from thermodynamic considerations will be exerted on the obstacle [28, 16]. This phenomenon plays key role in cell motility - as treadmilling filaments encounter cell's front it exerts a pushing force serving to generate leading edge protrusion.

2.1.2 Microtubules

The organization of microtubules is in many ways similar to that of actin. Tubulin is a heterodimer consisting of an α - and a β -subunit of about 55 kDa each. Microtubules are hollow tubes 25 nm in diameter consisting of thirteen protofilaments. Protofilaments arrange in a helix with a turn, containing 13 tubulin dimers, see Fig. 5. Microtubules are the stiffest polymers in the cell with persistence length of approximately 2 mm [25, 85].

Each tubulin subunit carries a nucleotide binding site. The α -subunit binds GTP, which is never hydrolyzed. The β -subunit is incorporated into a growing chain exclusively in the GTP form and undergoes subsequent hydroly-

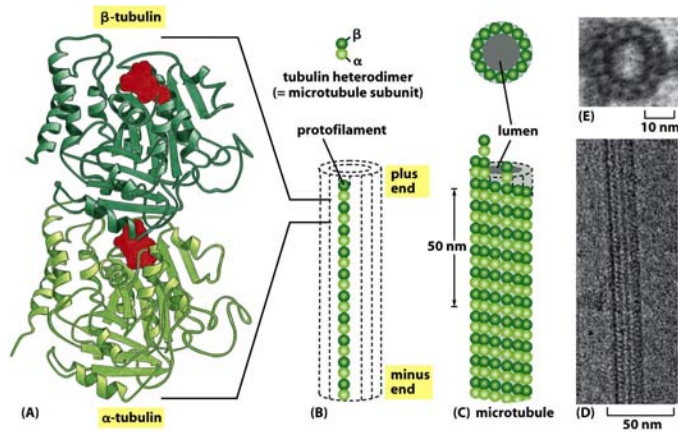


Figure 5: The structure of microtubule and its subunit. **(a)** The subunit of each protofilament is a tubulin heterodimer, formed from very tightly linked pair of α - and β -tubulin monomers. The GTP molecules bound to the subunits are shown in red. **(b)** One tubulin subunit and one protofilament are shown schematically. Each protofilament consists of many adjacent subunits with the same orientation. **(c)** The microtubule is a stiff hollow tube formed from 13 protofilaments, aligned in parallel. **(d)** A short segment of a microtubule, viewed in an electron microscope. **(e)** Electron micrograph of a cross section of a microtubule showing a ring of 13 distinct protofilaments. Taken from [1].

ysis. In this way, newly incorporated subunits form a zone of GTP-tubulin at the growing plus-end, followed by a zone of GDP-tubulin. If the filament elongation rate is slower than that of GTP hydrolysis within the chain, for example due to limited monomer availability, the GDP zone will eventually catch up with the plus-end. As this happens, a rapid depolymerization of microtubule from the plus-end is initiated, an event usually referred to as catastrophe. If elongation resumes before complete filament depolymerization, a rescue event is said to have occurred.

2.2 Motor proteins

Molecular motors are proteins that can bind to either microtubules or actin filaments and move along the polymer chain, while converting chemical energy stored in ATP into mechanical work. Their function is twofold: intra-

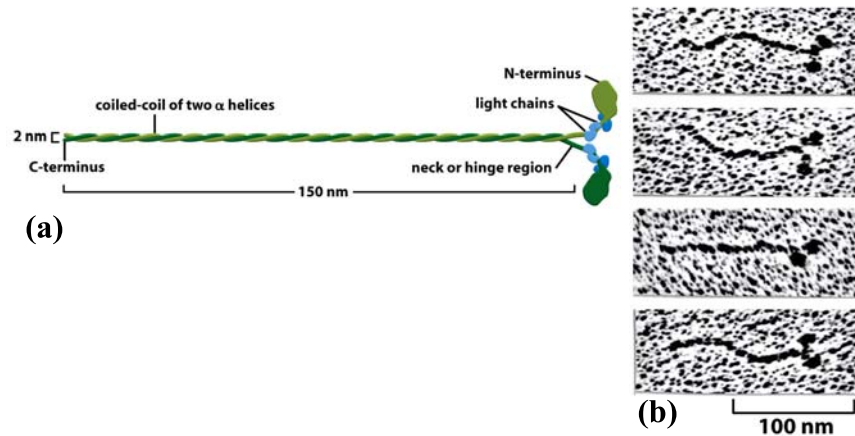


Figure 6: Myosin II. **(a)** A myosin II molecule is composed of two heavy chains (each about 2000 amino acids (green) and four light chains (blue)). The light chains are of two distinct types, and one copy of each type is present on each myosin head. **(b)** The two globular heads and the tail can be clearly seen in electron micrographs of myosin molecules. Taken from [1].

cellular transport and cell contractility. Through motor transport the cell for example distributes organelles in the cytoplasm. Force generation by motors is for example at the origin of cell shape and muscle contraction.

Molecular motors associate with the filaments through a "head", or motor domain, that can bind and hydrolyse ATP. Motors walk along filaments in discrete steps. A motor is said to be processive if the distance, it advances before detaching from filament, is large compared to its step size. Motors can be characterized by a force-velocity relation that specifies the speed at which they walk along a filament as a function of the load force on the motor. The motor velocity drops approximately linearly with an increasing opposing force. Eventually the speed turns negative, meaning that that motor starts to walk backwards. The value of the opposing force, causing a motor to stall is referred to as the stall force [10, 32, 79, 80].

2.2.1 Myosins

Myosins are molecular motors that interact with actin filaments. They were discovered in striated muscle in the beginning of 1950s, where they serve to generate contraction [33].

A molecule of muscle myosin (myosin II, see Fig. 6) consists of two identical subunits, each comprising a heavy chain, and two distinct light chains. Heavy chains consist of a head domain (at the N-terminus) which binds actin, and a tail domain, which can crosslink many motors into a bundle.

Many myosins are non-processive. However, myosin bundles containing large number of motors are: while some motors in a bundle detach, others remain associated with the actin filament. Initially, it was thought that myosin is only present in muscle, but by now it is known that virtually all eukaryotic cells have certain myosin.

Eighteen myosin families have been identified (conventionally designated by roman numerals, e.g. muscle myosin is Myosin II). All myosins except myosin VI walk towards filament's barbed end. The human genome comprises 40 myosin genes [1].

2.2.2 Kinesins

Kinesins are motors that bind tubulin and were discovered in 1985 in squid giant axon where they carry membrane-enclosed organelles away from the neuronal body towards the axon terminal [84]. Most kinesins have their motor domain at the N-terminus and walk towards a microtubule plus-end. However, kinesin-14 (Ncd in *Drosophila* and Kar3 in yeast) is a peculiar exception: it has its head domain at the C-terminus and walks towards microtubule plus-ends, see Fig. 7. Most kinesins are processive, and have speeds up to about $3 \mu\text{m/s}$.

Kinesins serve mainly two biological functions: intracellular transport and reorganization of the microtubule network. Some kinesins, however, serve to regulate microtubule depolymerization dynamics. For example, kinesin-13 family motors move diffusively on a filament and are preferentially associated with the filament plus-end, where they induce filament depolymerization [56]. These molecules are implicated in chromosome segregation during mitosis. Another microtubule depolymerizing motor is Kip3, a member of the kinesin-8 family. Kip3 mutant cells show abnormally long mitotic spindles. Upon binding, this motor moves processively towards the filament plus-end, where it removes precisely one tubulin subunit and falls off [27]. If many Kip3 molecules bind the same filament they will pile up at the tip, forming a gradient, decaying towards the minus-end. The longer a filament is, the more Kip3 it will accumulate, resulting in a higher Kip3 concentration at its

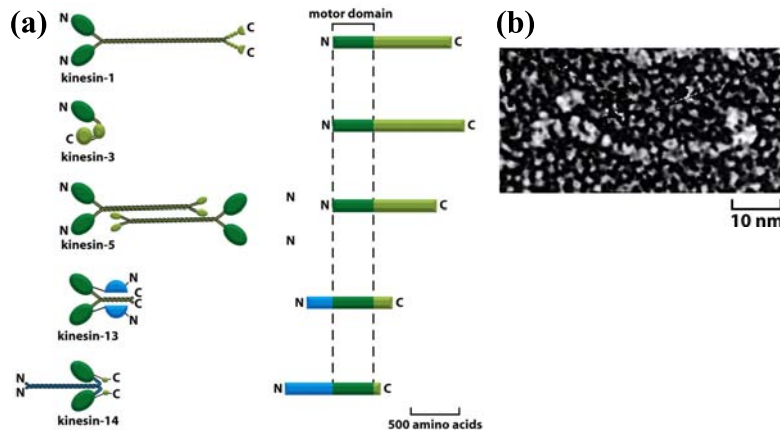


Figure 7: Kinesin and kinesin-related proteins. **(a)** Structures of five kinesin superfamily members. Kinesin-1 has the motor domain at the N-terminus of the heavy chain. The middle domain forms a long coiled-coil, mediating dimerization. The C-terminal domain forms a tail that attaches to cargo, such as membrane-enclosed organelle. Kinesin-3 represents an unusual class of kinesins that seems to function as monomer and move membrane-enclosed organelles along microtubules. Kinesin-5 forms tetramers which are able to slide two microtubules past each other. Kinesin-13 has its motor domain, located in the middle of the heavy chain. It is a member of a family of kinesins that bind to microtubule ends and increase dynamic instability of the microtubules. Kinesin-14 is a C-terminal kinesin that walks towards the minus-end of the microtubule. **(b)** Freeze-etch electron micrograph of a kinesin molecule with the head domains on the left. Taken from [1].

tip and, consequently, higher rate of plus-end depolymerization. In this way the microtubule length can be regulated.

Kinesins and myosins are very different in terms of size and aminoacid sequence. Yet, their three-dimensional structure reveals a similar core containing the ATP binding site that is responsible for conversion of chemical energy into mechanical work. Their structural similarity points towards a common evolutionary origin of the two motors [1].

Kinesins are subdivided into 14 families. The human genome contains 45 kinesin genes [1].

2.2.3 Dyneins

Dyneins are minus-end directed microtubule associated motors, discovered in the 1960s in cilia [24]. Structurally they are different from kinesins and myosins. Dyneins are composed of two or three heavy chains and a large and variable number of intermediate and light chains, see Fig. 8. These are the largest and the fastest molecular motors, capable of advancing along the filament at speeds as fast as $14 \mu\text{m/s}$.

Dyneins are subdivided into three families: cytoplasmic dyneins (involved in vesicle trafficking and reorganization of the Golgi apparatus), axonemal dyneins, which are responsible for the beating of cilia and flagella, and a third minor family involved in the beating of cilia.

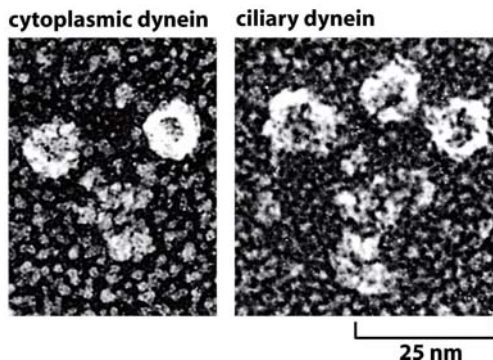


Figure 8: Freeze-etch electron micrographs of a molecule of cytoplasmic dynein and a molecule of ciliary dynein. The former has two heads, the latter has three. Taken from [1].

2.3 Cytoskeleton associated proteins

Myriads of proteins other than molecular motors influence the dynamics of cytoskeletal filaments in a variety of ways. These include crosslinkers that simultaneously bind several filaments and crosslink them into stiff bundles, cappers that attach to the plus-end and prevent filament elongation, agents that induce filament branching, etc. Some important cytoskeleton-associated proteins and their function are listed in Table 1. Around 100 protein types of actin binding proteins have been identified. For up-to-date information on these see <http://www.bms.ed.ac.uk/research/others/smaciver/Encyclop/encycloABP.htm>. For further information on microtubule associated proteins we refer to Ref. [40].

Actin-associated proteins	
Name	Function
Formin	Nucleates filament, remaining associated with the growing plus-end
ARP complex	Induces filament branching
Profilin	Binds free subunits and speeds up filament elongation
Tropomyosin	Stabilizes filaments
Capping proteins	Prevent assembly and disassembly at the plus-end
Gelsolin	Severs filaments and attaches to plus-ends
Cofilin	Accelerates disassembly upon binding to polymeric ADP-actin
α -actinins, fimbrin, filamin	Crosslink filaments
Spectrin, ERM	Attach filaments to membranes
Microtubule-associated proteins	
Name	Function
γ -TuRC	Nucleates assembly and remains attached to the minus-end
Stathmin	Binds subunits, preventing assembly
+TIPs	Remain associated with growing plus-ends and can link them to other structures e.g. membranes
Kinesin-13	Enhances catastrophic disassembly at plus-end
Katanin	Severs microtubules
MAPs	Stabilize microtubules
XMAP215	Stabilizes plus-ends and accelerates assembly
Tau, MAP-2	Crosslink filaments
Plectin	Link microtubules to intermediate filaments

Table 1: Cytoskeleton-associated proteins. Adopted from [1].

3 Self-organized structures in the cytoskeleton

The complexity of cell morphology and behaviors can have two plausible origins. One is the complexity of the genome and the associated regulatory gene expression pathways. In this way, the complexity of individual intracellular constituents, e.g., the chromosomes, directly determines the complexity on a cellular level. The other possible source of complexity is self-organization of intracellular components such as cytoskeletal constituents. Cytoskeletal self-organization is most directly demonstrated in biomimetic assays, i.e., in solutions of purified biomolecules. For example, it has been shown that asters, reminiscent of mitotic spindle poles form spontaneously in mixtures of kinesin motors and microtubules. These cannot be assembled by some complex organizing centers such as centrosomes since these solutions do not contain any. Hence, their structures must be self-organized. Unfortunately, many interesting cellular structures, widely thought to be self-organized, e.g., the cell motility apparatus, have not yet been reconstituted *in vitro*. When studying these, one has to rely on data from experiments with cell fragments or even whole intact cells. This section describes some experimental observations of self-organized processes in the cytoskeleton.

3.1 Motor-filament *in vitro* assays

In order to study the mechanisms, underlying the formation of mitotic spindle, F. Nédélec and co-workers developed an *in vitro* assay that allows to examine pattern-forming properties in kinesin-microtubule solutions [58, 74]. Kinesins can be crosslinked into clusters of several motors, such that each cluster can interact with several microtubules simultaneously. Microtubules in aqueous solutions have been shown to self-organize into asters and vertices in presence of kinesin complexes and ATP. Specifically, at low molecular motor concentrations, the filament distribution remains isotropic. At higher motor densities, a lattice of microtubule vortices appears, see Fig. 9. As the motor concentration is raised further, vortices turn into asters, i.e. microtubule aggregates, in which all filaments emanate radially outwards from one point. Finally, at very high motor concentrations, filaments bundle. The structure of microtubule asters is similar to that of mitotic spindle poles. The structure of motor clusters used in experiments is reminiscent of kinesin-5,

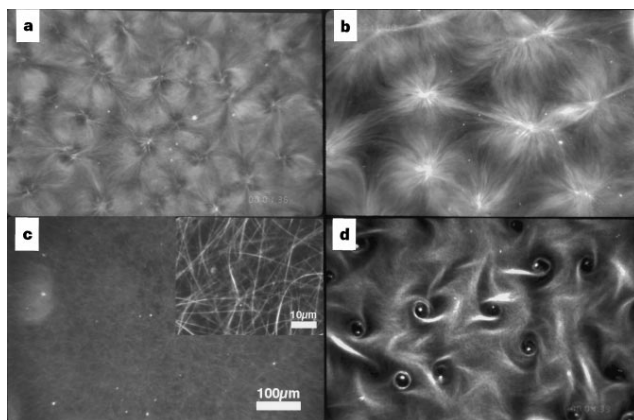


Figure 9: Different large-scale patterns formed through self-organization of purified microtubules and motors. The samples differ in the kinesin concentration. **(a)** A lattice of asters and vortices obtained at 25 mg ml^{-1} kinesin. **(b)** An irregular lattice of asters obtained at 37.5 mg ml^{-1} kinesin. **(c)** Microtubules form bundles at 50 mg ml^{-1} kinesin (scale bar, $100 \mu\text{m}$). Insert, at higher magnification (scale bar, $10 \mu\text{m}$). **(d)** A lattice of vortices obtained at 15 mg ml^{-1} kinesin. Taken from [58].

a motor that forms tetramers, capable of binding several filaments simultaneously and sliding them past one another. Kinesin-5 is required for spindle assembly, for example in the marine brown alga *Silvetia compressa* [63], suggesting that mechanisms of spindle formation are similar to those, underlying pattern-forming properties of *in vivo* motor-filament assays, described in [58].

3.2 Melanophore fragments

Melanophores are skin cells of reptiles and fish that allow them to change color. In this way, animals can hide from predators or avoid being seen by their prey. The cytoplasm of melanophores contains color pigment granules, which can aggregate in the cell center when color needs to be changed and redisperse when skin coloration has to be restored. Granule aggregation and redispersion are controlled by neural signals. Even small melanophore fragments are capable of aggregating granules much like whole intact melanophores: upon pinching off a piece from a larger cell, pigment granules, trapped inside the fragment, gather at the excision site, see Fig. 10. Thereafter, the

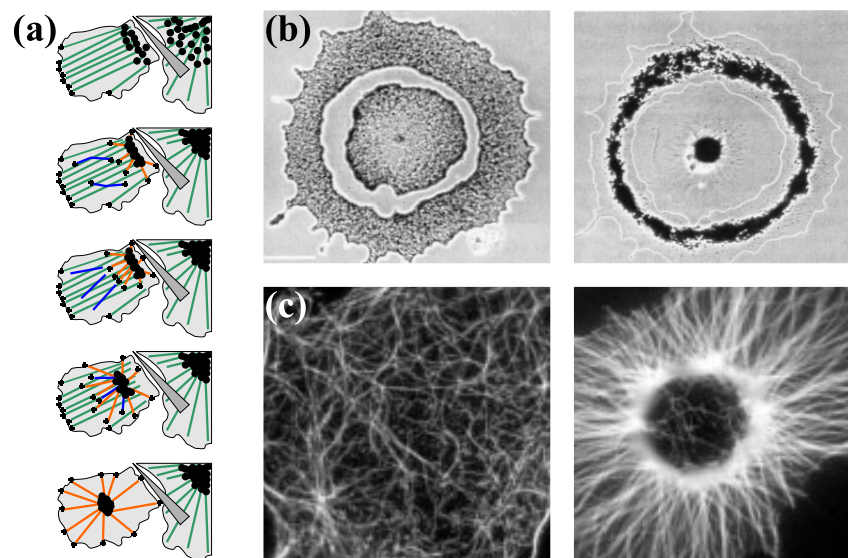


Figure 10: Self-organization of microtubules and motors in fish melanophores. **(a)** Schematic explanation of experiments on melanophore fragments. Upon pinching a fragment off the cell, pigment, trapped in its cytoplasm, aggregates at the excision site. Thereafter granule aggregate relocates to the center of the fragment. Upon completion of pigment centering microtubules arrange in an aster, centered at the middle of the fragment. **(b)** Pigment distribution in melanophore fragments of different shape before (left) and after centering (right). In the disc-shaped middle fragment pigment aggregates in its center. In an annular fragment there forms a "ring" of condensed pigment, concentric with its boundary. Taken from [67]. **(c)** Microtubule distribution in melanophore fragments before (left) and after centering (right). Initially, microtubules are randomly distributed. Subsequently, all filaments point radially, away from the center where pigment aggregate is seen. Taken from [90].

pigment aggregate relocates to the fragment center. Microtubule staining reveals that filaments, trapped inside the cell piece, arrange into an aster, with its center in the middle of the fragment. By treating fragments with taxol (a drug which prevents microtubule depolymerization, leading to complete consumption of tubulin monomer) pigment centering is abolished. Hence,

pigment centering in melanophores is accompanied by and dependent on cytoskeletal rearrangement. This reorganization has two possible explanations: either filaments get displaced by molecular motors, or they move due to treadmilling. In order to distinguish between the two mechanisms, it is possible to stain microtubules heterogeneously, for example by photobleaching a spot in a homogeneously stained filament. It is found that the bleached spot does not displace as microtubule translates [67]. Consequently, microtubules are subject to treadmilling. Despite the fact that motors do not transport microtubules, they have proven to be essential for aster formation in melanophores. When fragments are treated by dynein inhibitors, pigments do not center and the microtubule aster does not form. Presumably, pigment granules are actively transported towards the fragment center along the rays of the filament aster. Importantly, aster assembly requires also the presence of pigment granules: melanophore fragments containing no pigment granules do not assemble radial microtubule arrays. Consequently, the dynamics of microtubules depends on that of the granules. Initially it was supposed that dynein motors re-organize filaments by actively transporting some agent, capable of nucleating microtubules. However, it has now been shown that purified dyneins themselves can serve as microtubule nucleators [67].

3.3 Keratocyte fragments

Keratocytes are cells that constitute a part of the skin of fish and reptiles and are implicated in wound healing. These cells have two main properties, making them a valuable model system for cell locomotion: firstly, they are the fastest crawling cells known today. Moreover, unlike most other cells that can crawl, keratocytes preserve their characteristic fan-like shape when crawling on a substrate [48]. The organization of some cytoskeletal proteins in a crawling keratocyte is shown in Fig. 11. At the cell front actin filaments generate a protrusion by growing against the cell edge. Myosin staining reveals that myosin motors localize at the rear, where they serve to organize filaments into a tightly compressed bundle.

Small fragments of keratocytes can crawl on a surface, assuming a fan-like shape much like intact keratocytes [20, 86]. Hence, cell motility is likely to be self-organized, rather than to be dependent on some organizing center.

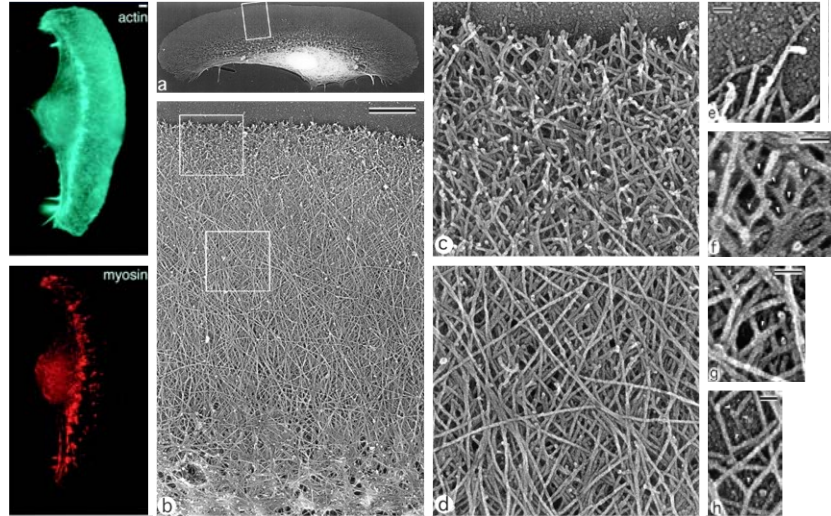


Figure 11: Cytoskeletal organization on keratocytes. Left: myosin and actin staining of a crawling keratocyte. Right: Organization of actin filaments in keratocyte lamellipodia. EM of detergent-extracted cells. (a) Overview of a locomoting cell; (b) actin network in lamellipodia from the leading edge (top) to the transitional zone (bottom); (c) brushlike zone at the leading edge with numerous filament ends; (d) smooth actin filament network in the middle part of lamellipodia; (e-h), T junctions (arrowheads) between filaments at the extreme leading edge (e), within the brushlike zone (f), in the central lamellipodia (g), and close to the lateral edge of the lamellipodia (h). The cell's leading edge is oriented upward in all panels. Boxed region in (a) is enlarged in (b); upper and lower boxed regions in (b) are enlarged in (c) and (d), respectively. Bars: (b) 1 μm ; (e-h) 50 nm. Taken from [75].

3.4 Actin waves in *Dictyostelium discoideum*

Dictyostelids are soil-living amoebas. A particular species, *Dictyostelium discoideum*, has become a model system for studying chemotaxis and development [37, 14]. When subjected to starvation dictyostelids start to aggregate into a single slug of many cells, locating one another by communication through chemotactic signals of cyclic adenosine monophosphate (cAMP) (a school-book example of self-organization in a biological system). After formation, the slug migrates away from the site of limited nutrient availability

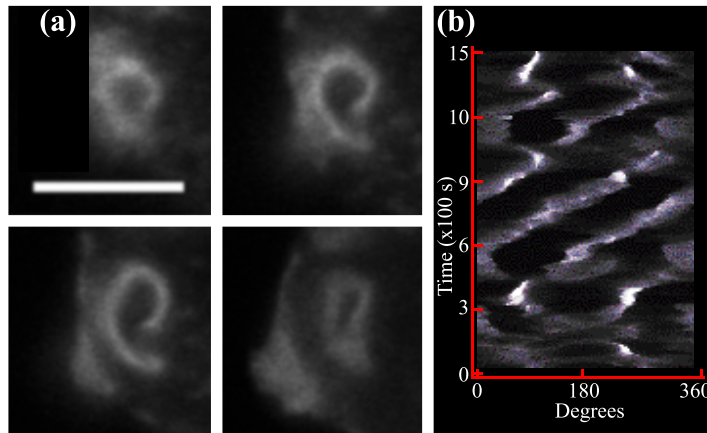


Figure 12: Scroll waves of F-actin in *Dictyostelium discoideum*. **(a)** Four sections through a spiral in a pseudopodium of a cell show that the F-actin pattern may be a segment of a scroll wave extending at least $3 \mu\text{m}$. The first three sections are $0.2 \mu\text{m}$ apart and the fourth is $2.0 \mu\text{m}$ below. The bar indicates $5 \mu\text{m}$. Taken from [89]. **(b)** Space-time plot of cell protrusion showing traveling waves. Taken from [38].

in search of better living conditions. Eventually, it culminates, forming a fruit body that releases spores, subsequently developing into new amoebas.

Dynamics of shape of a single *Dictyostelium discoideum* cell at the first sight appears quite erratic. Thus, one might think it is purely stochastic and is driven by random fluctuations. Quantitative analysis of cell boundary dynamics reveals that it remains coherent on long temporal and spatial scales. Most readily this is seen in a space-time plot of the magnitude of the edge protrusion measured as distance to the cell boundary from the cell's mass center versus an angular coordinate, parameterizing the edge, see Fig. 12. This way a regular pattern of interacting traveling waves is seen [38, 39]. Qualitatively similar membrane waves have been shown to be ubiquitous in spreading cells [17, 18, 22, 23]. Imaging *Dictyostelium discoideum* cells, transformed with GFP-actin reveals that protrusions are generated by radial waves of polymerizing actin that originate from cell's interior [88, 89]. Upon nucleation, an actin wave turns into an expanding ring, leading to a protrusion when encountering the cell edge. Occasionally, actin waves turn unstable, forming spirals reminiscent of those seen in Belousov-Zhabotinsky

reaction, see Fig. 12. These data suggests that the dynamics of dictyostelid cells is driven by self-organized actin patterns.

3.5 Actin waves in neutrophils

Neutrophils are the most abundant white blood cells, forming an integral part of the immune system. These cells undergo chemotaxis, localizing to sites of infection by sensing gradients of interleukins and interferons. Neutrophils are phagocytes: at the site of infection they serve to engulf microbes and other pathogens [49].

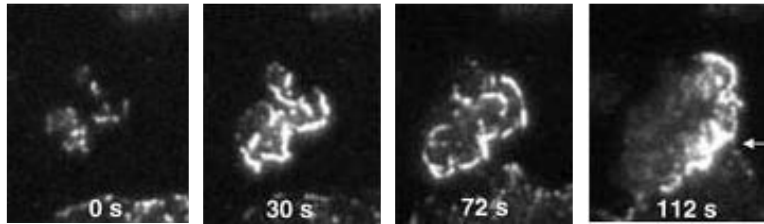


Figure 13: Hem-1 waves in human neutrophils visualized by TIRF microscopy. Taken from [91].

Much like dictyostelids, neutrophils exhibit actin waves that interact with the cytoplasmic membrane [91]. In order to examine molecular mechanism of actin wave dynamics, it proved useful to assess the intracellular localization of protein Hem-1 which is a member of the Scar/WAVE complex that serves to regulate actin polymerization dynamics. Intracellular localization of Hem-1 fused with a yellow fluorescent protein (YFP) tag was visualized by total internal reflection microscopy (TIRF). Hem-1 appeared to aggregate on the membrane forming foci, which subsequently burst in outwardly propagating waves with a speed of propagation of approximately $4 \mu\text{m}/\text{min}$. Two possible mechanisms of wave-propagation could be envisaged: either Hem-waves advance due to translocation of Hem-1 particles along the membrane (i.e. the same protein particles constitute the wave-front at any time instance), or Hem-1 protein at the rear of the wave-front are continuously discarded into the cytoplasm and progressively recruited to the membrane at the leading edge of the wave. Weiner and co-workers distinguished between the two possible modes of wave-propagation by employing photo-bleaching [91]:

bleaching a spot of Hem-1-YFP wave-front, it was observed that the spot was not carried along with the wave, indicating that the front propagates by successive recruitment of Hem rather than by protein translocation. Plausibly, the release of Hem-1 into the cytoplasm must be accomplished by some downstream effector of Hem-1, shown to be F-actin: poisoning neutrophil with latrunculin (a drug promoting actin depolymerization) the life-time of the wave increased approximately 20-fold. This suggests that F-actin could accumulate at the rear of the propagating wave, forming an "inhibition zone" behind the leading edge of the front, serving to expel Hem-1 into the cytoplasm. In accordance with this assumption, one could occasionally observe several fronts, traveling in the same direction behind one another some rather precisely defined distance apart, supposedly corresponding to the typical size of inhibition zone. Upon treating neutrophils with jasplakinolide, a drug inhibiting actin depolymerization, the distance between subsequent Hem-peaks enlarged, in accordance with existence of actin-reach inhibition zone between subsequent Hem-fronts. Finally, it has been shown that Hem-waves allowed neutrophils to sense their environment: the wave extinguished when reaching the leading edge of the cell if the leading edge encountered a mechanical barrier.

4 Physical approaches to cytoskeletal pattern formation

In the previous section we have listed a number of examples of self-organized cytoskeletal phenomena. When developing physical descriptions of cytoskeletal systems, one is naturally confronted with the problem of describing ensembles of particles that each have many degrees of freedom. A number of recently developed theoretical approaches offer ways for dealing with this problem. Roughly, these can be subdivided into three classes: microscopic, mesoscopic and phenomenological macroscopic descriptions. Microscopic formulations (molecular dynamics, MD) describe the dynamics of individual particles. Mesoscopic mean field descriptions treat the system's dynamics in terms of densities, i.e., distributions specifying the probability of finding particles in a certain state at a given time. To every microscopic description corresponds a unique mesoscopic one and *vice versa*. When dealing with systems of particles that each have many degrees of freedom, numerical solution of the corresponding mean-field equations is unfeasible due to current limitation on processor speed, even when exploiting parallel algorithms. Circumventing this problem is sometimes possible by rewriting the mesoscopic equations in terms of averaged quantities, depending on a smaller number of variables. For example, nematic order in liquid crystals is described by nematic order parameter rather than by specifying full distribution of orientations of the liquid crystal molecules. Finally, phenomenological descriptions are formulated in terms of order parameters, like those encountered when simplifying mesoscopic formulations. Within a phenomenological approach, equations are derived on the basis of general considerations such as symmetry arguments rather than from an underlying microscopic picture. This section illustrates the three approaches and discusses their strengths and weaknesses.

4.1 Molecular dynamics

The work of F. Nédélec on theoretical descriptions of motor-filament systems illustrates the microscopic approach [58, 74, 57, 59]. Individual filaments were simulated as rods of finite stiffness, that can grow. Filaments will reach their final length due to limited monomer availability. Motor complexes are described as two motor heads that can bind one filament each and exert forces, resulting in filament displacement. Having advanced all the way to the

filament plus-end, motors were assumed to detach at some prescribed rate. The system was shown to self-organize into asters and vertices much like those, seen in experiments with microtubule-kinesin mixtures. Interestingly, asters turned into vertices upon increasing the rate of motor unbinding from the filament plus-end.

In an MD simulation, the number of simulated molecules rather than the number of degrees of freedom of a single molecule limit the simulation time. Since MD describes individual molecules, experimentally determined details of the molecule structure and of inter-molecule interactions are readily introduced into the description and simulation results are easily interpreted. However, exploration of parameter space that can be done by means of, for example, a linear stability analysis in the case of mesoscopic and phenomenological descriptions is not applicable to microscopic descriptions. Hence, exhaustive characterization of dynamical states, exhibited by the system is seldom feasible. Arguably, the main disadvantage of MD is its insufficient generality. The precise form of equations, determining dynamics of particles in an MD simulation is often too system-specific to reveal similarities and unobvious interconnections between different physical systems.

4.2 Mean field mesoscopic descriptions

Microscopic descriptions can generically be formulated in terms of Langevin equations. The corresponding mesoscopic formulation is given by the corresponding Fokker-Planck equations. Simulating Langevin equations yields a random sequence of transitions between different states of the particles, whereas by simulating the Fokker-Planck equations one obtains the probability of finding the particle in a particular state at a particular time.

Two approaches to mesoscopic descriptions of the cytoskeleton have been established. One is deriving dynamic equations starting from force balance in much the same way as when deriving Navier-Stokes equations by considering forces on a material element of the fluid. The second approach derives dynamics from transition probabilities associated with various state changes of a particle, in much the same way as when deriving hydrodynamic equations starting from the Boltzmann equation [9].

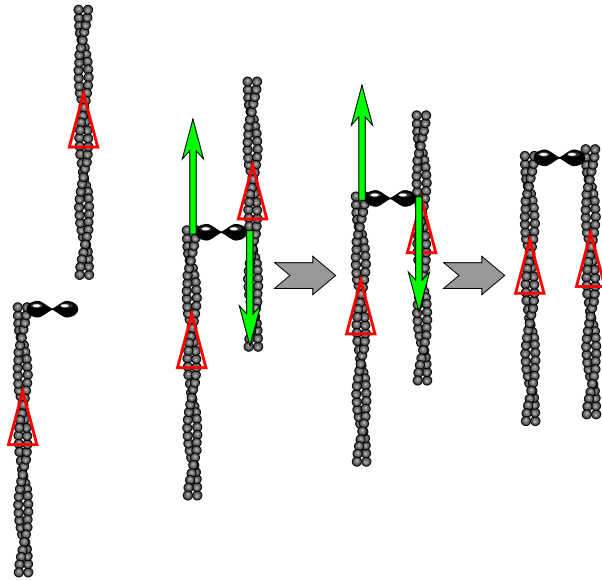


Figure 14: Illustration of possible interactions between parallel filaments. Filaments that do not overlap in space can not interact (left-most filament pair). Green arrows indicate forces on filaments from motors. One motor head is permanently bound to the plus-end of one filament, the other motor head is walking along the other filament. In this way, the two plus-ends eventually converge.

4.2.1 Force balance

As an illustration of the approach through force balance, consider a system of filaments, that are aligned along the same line and compressed into a bundle. Suppose that all filaments in the bundle have the same orientation (determined by their polarity). Suppose further that two-headed molecular motors are present in the bundle, forming active crosslinks between filament. Filaments of the same orientation may interact due to end effects that could for example result in convergence of their plus-ends (see Fig. 14).

Assuming a homogeneous motor density and constant filament length, the force experienced by a filament due to the presence of another one is a function of inter-filament distance ξ alone. Denoting this force by $f(\xi)$, total the force on filament at spatial position x along the bundle is

$$f(x) = -\eta v(x) + \int d\xi c(x + \xi) f(\xi) - \eta D \partial_x \ln(c) \quad (4.1)$$

where $c(x)$ is filament density, v is the filament speed, η is the friction coefficient with the surrounding stationary solvent. The last term is an entropic force, capturing the effects of random fluctuations, see [7, 19]. The integral term sums the force contributions from surrounding filaments. Importantly, $f(\xi)$ is odd in ξ since the force exerted by one filament on another is equal in magnitude and opposite in direction to the force exerted by the latter on the former (Newton's third law). For simplicity, f may be taken to be piecewise constant if the absolute value of ξ is smaller than filament length and zero otherwise. The latter is motivated by the fact that filaments that do not overlap in space can not form a crosslink and hence do not interact, if motors are point objects. Equation (4.1) relies crucially on a mean-field assumption: every filament feels the averaged field of the surrounding filaments. Having specified the forces on a filament, the equation of motion is obtained by equating the force in (4.1) with acceleration times filament mass. After an appropriate dedimensionalization, neglecting inertia and solving for the filament speed v one obtains

$$v = \frac{1}{\eta} \left[\int d\xi c(x + \xi) f(\xi) - \eta D \partial_x \ln(c) \right] \quad (4.2)$$

If filaments are neither created nor destroyed, the filament density obeys the continuity equation

$$\partial_t c = -\partial_x v c \quad (4.3)$$

Combining Eq. (4.3) with Eq. (4.2) gives

$$\partial_t c(x) = -\partial_x \left[\frac{1}{\eta} c(x) \int d\xi c(x + \xi) f(\xi) \right] + D \partial_x^2 c(x) \quad (4.4)$$

This is an elementary description of the density dynamics in a filament bundle. Importantly, this simple equation exhibits an interesting instability: at high enough magnitude of inter-filament interactions f , filaments pile up at one point [45, 46].

The derivation of equation (4.4) outlines the general procedure for constructing a mean-field description from momentum and mass conservation. The starting point is writing down forces between the different particles, as

functions of particle coordinates. Importantly, since inertia can be neglected, these must appear in pairs of equal magnitude and opposite sign to ensure momentum conservation. Particle speeds follow from equating the total force on a particle to zero. Substituting these into the continuity equation and exploiting the mean-field assumption, gives the required description.

A number of works have been based on this method for describing cytoskeletal systems. In [45, 46] equations described myosin-driven contraction of actin filament bundles observed in reconstituted biomimetic assays [76, 77]. Interestingly, it was found that interactions between filaments of opposite orientation can result in traveling wave of propagating density maxima. Generalizations of the approach of [45, 46] to two-dimensions have been presented in [51, 52, 47]. Calculation of the stress distribution in the gel is presented in [47]. Nonlinear analysis and numerical solutions of the equations in [51, 52] can be found in [94], where it was shown that in two dimensions the system can self-organize into periodic patterns of asters or stripes.

4.2.2 Boltzmann equations

This method is inspired by approaches to the dynamics of granular gases [9]. When describing a dilute gas it is admissible to consider only two-particle collisions. Further, it is safe to assume that the statistics of the particle configurations changes on a time-scale which is very much slower than that of inter-particle interactions. Hence, on long time scales, two-particle collisions appear as instantaneous transitions from one state of a particle pair to another, uniquely defined by the initial configuration.

As an illustration consider a system of polar rods that interact by pairwise collisions. Each rod is characterized by its orientation, i.e., the angle θ with a particular coordinate axis. Assuming the system to be spatially homogeneous, it is described by a probability distribution $P(\theta)$ for the filament orientations. Interacting rods align: when two rods with orientation θ_1 and θ_2 collide, they end up both having orientation $(\theta_1 + \theta_2)/2$. Importantly, the mapping, relating filament orientations before and after "collision", must be invariant with respect to interchanging indices 1 and 2 due to the symmetries of the problem. The dynamics of $P(\theta)$ is given by:

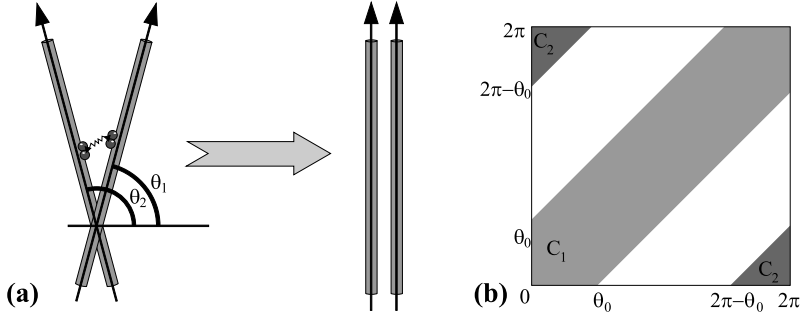


Figure 15: (a) Schematic illustration of rod alignment. (b) Integration domains in equation (4.5). Adopted from [2].

$$\begin{aligned}
\partial_t P(\theta) = & D_r \partial_\theta^2 P(\theta) + g \int_{C_1} d\theta_1 d\theta_2 P(\theta_1) P(\theta_2) \\
& \times [\delta(\theta - \theta_1/2 - \theta_2/2) - \delta(\theta - \theta_2)] \\
+ g \int_{C_2} & d\theta_1 d\theta_2 P(\theta_1) P(\theta_2) \times [\delta(\theta - \theta_1/2 - \theta_2/2 - \pi) - \delta(\theta - \theta_2)]
\end{aligned} \tag{4.5}$$

Here δ is Dirac delta function, g specifies the inter-filament interaction strength, and D_r is rotational diffusion constant, capturing effects of noise. The integration domains C_1 and C_2 are sketched in Fig. 15, chosen in such a way as to ensure that filaments preferentially interact when they are approximately parallel. Rods of orientation θ are generated by collisions of two rods whose orientations sum up to 2θ (first term in both integrands) and disappear due to collisions with rods of any orientations other than θ (second integrand term). Equation (4.5) exhibits an interesting instability: polar order sets in at high enough values of g .

Equation (4.5) can be extended to account for spatial variations in the filament density, see [2]. The resulting equations exhibit patterns of coarsening asters and vortices, much like microtubule-kinesin solutions in experiments of F. Nédélec [58]. A further extension of the approach accounting for the dynamics of the motor distribution is given in [3].

The derivation of equation (4.5) is very similar to the derivation of the dynamic equations describing reaction-diffusion systems: two rods with ori-

orientations θ_1 and θ_2 "react", generating two rods both having orientation $\theta_1/2 + \theta_2/2$. In contrast to what was done in the previous section, the description is formulated without directly exploiting Newton's equations of motion.

In this section we described two methods for deriving mesoscopic equations of motion. The mesoscopic approach has a number of strengths. Since the description is formulated as a set of partial integro-differential equations, conventional methods from the theory of dynamical systems are applicable for examining solutions. For instance, it is possible to explore parameter space by means of a linear stability analysis. Nonlinear expansions can be used to derive analytic expression for solutions in the vicinity of bifurcation. Much like in the case of MD, parameters have a clear microscopic interpretation.

The main weakness of mesoscopic formulations is associated with describing molecules with many degrees of freedom. For example, when describing (bio)molecules that are free to move in three dimensions, to rotate and to change their orientation, the descriptions will contain fields, depending on five variables. Current limitations on processor speed make the method inapplicable for describing molecules with more than three degrees of freedom. This problem may be circumvented by introducing order parameters that are obtained by appropriately averaging the quantities, appearing in the original mesoscopic equations. For example, when studying equation (4.5) one can decompose the angle-dependent rod density P in Fourier modes (these depend on time but not on filament orientation) and solve for dynamics of modes instead of working directly with orientation distribution. A problem with this approach is that generically, for non-linear descriptions, dynamic equation for time-evolution of any one order parameter requires the knowledge of time-evolution of infinitely many other order parameters. For instance, the dynamics of Fourier mode n of filament orientation distribution in (4.5) requires the knowledge of Fourier modes of order higher than n . Hence, expansions in Fourier harmonics need be truncated at some finite n to obtain a closed equation set. Unfortunately, however, up to date, no method guarantees that truncated equations converge to full description in the limit of large n .

The second problem associated with mesoscopic equations is the appearance of integral terms, whose calculation requires long computation time. The integrals can be simplified by using coarse-graining. The idea behind

the technique is the same as that behind the multipole expansion in electrodynamics and fluid mechanics. As an example, consider equation (4.4). Taylor-expanding $\rho(x+\xi)$ in ξ and integrating, the integral term is re-written as $A_1\partial_x\rho(x) + A_2\partial_x^3\rho(x)$ where $A_1 = \int d\xi f(\xi)\xi$, $A_2 = \int d\xi f(\xi)\xi^3/3$ and so on, yielding

$$\partial_t c(x) = -\partial_x [c(x)(A_1\partial_x c(x) + A_2\partial_x^3 c(x))] + D\partial_x^2 c(x) \quad .$$

This approximation is valid only provided that the filament density ρ varies on a scale, much larger than that of integral kernel f which is not always possible to ensure.

4.3 Phenomenological descriptions

As was described in the previous section, mesoscopic equations, involving fields that depend on many variables do not generically yield a closed set of equations when re-written in some appropriate averaged quantities, depending on a smaller number of variables. Phenomenological descriptions derive equations for some suitable averaged quantities from some general principle, such as symmetry considerations. However, it is understood that any phenomenological description can be derived from some mesoscopic formulation, although it is not always clear how. Two major approaches to phenomenological descriptions of the cytoskeleton have been established. One exploits symmetry arguments alone, the other one in addition relies on non-equilibrium thermodynamics.

4.3.1 Symmetry-based phenomenological descriptions

Consider a system of interacting filaments. Describing filaments as rigid polar rods of the same length, the state of the system is fully determined by the filament distribution $c(\mathbf{r}, \hat{\mathbf{u}}, t)$ giving concentration of filaments at spatial position \mathbf{r} , pointing along unit vector $\hat{\mathbf{u}}$ at time t . Integrating c over all filament orientations $\hat{\mathbf{u}}$ defines the scalar filament density ρ . The averaged filament orientation $\int d\hat{\mathbf{u}} \hat{\mathbf{u}} c$ gives the polarization vector \mathbf{p} . Averaging the outer product of $\hat{\mathbf{u}}$ with itself gives a symmetric second rank tensor. Multiplying its anisotropic part by 2 defines symmetric traceless tensor, called nematic order parameter. Importantly, only a finite number of tensors of a given rank may be contracted from these three order parameters and their derivatives if restricting to products and derivatives of some finite

orders. It can be shown that the n th moment of the filament orientation can be written as a function of n th Fourier harmonic of filament concentration which is 2π -periodic in polar coordinates θ and ϕ of filament director $\hat{\mathbf{u}} = [\sin(\phi)\cos(\theta), \sin(\phi)\sin(\theta), \cos(\phi)]$, see Fig. 16. Assuming that the three lowest Fourier modes suffice to describe the system, the time evolution of the density, the polarization and the nematic tensor is determined by these three order parameters alone. The most general expression for the dynamics of any one of these tensorial quantities is obtained by equating its time derivative with linear combination of all possible tensors constructed from them. The expansion coefficients serve as phenomenological parameters.

The main advantage of the method is that it is applicable to pretty much any system since it avoids the problem of truncating moment expansions encountered when systematically deriving dynamics from an underlying mesoscopic formulation. This approach is very general, based on symmetry arguments alone. One major disadvantage is the difficulty of relating results to the underlying microscopic details of the system since phenomenological parameters in general do not have obvious physical interpretation.

This method has been widely applied to descriptions of nematic liquid crystals and animal swarms [12, 61, 81]. In the former case, the dynamic equations are derived by varying the free energy, assuming it can be expressed in terms of nematic order parameter alone. In the latter case, the dynamics is described by a single order parameter, namely the particle speed. In both cases the number of phenomenological parameters is significantly restricted due to these special features. On the contrary, descriptions of cytoskeletal dynamics in general require rather large number of phenomenological parameters and do not follow from free energy variation since the cytoskeleton is an out-of-equilibrium system. Hence, the phenomenological descriptions of cytoskeleton derived

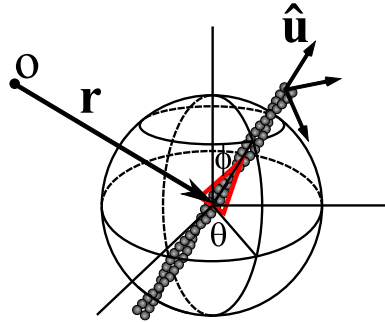


Figure 16: Schematic illustration of degrees of freedom of a filament: three-dimensional mass center-coordinate \mathbf{r} and orientation given either by director $\hat{\mathbf{u}}$ or by azimuthal and polar angles θ and ϕ , respectively, parameterizing the director.

by systematic expansion, may contain many tens of parameters, prohibiting exhaustive exploration of parameter space.

Phenomenological description of motor-filament system exhibiting patterns of asters and vertices was proposed in [50]. An application of the method to describing formation of mitotic ring is given in [97]. Nematic transitions in systems of cytoskeletal polymers were studied phenomenologically in [95].

4.3.2 Hydrodynamics

Much like many equations of continuum mechanics this method derives the dynamics by combining conservation laws with linear constitutive equations. As an illustration consider the derivation of the equations presented in [26], describing the dynamics of the muscle fiber. Equations of motion follow from conservation of mass and momentum:

$$\begin{aligned}\partial_t \rho &= -\nabla \cdot \mathbf{v} \rho \\ \partial_t \rho \mathbf{v} &= \nabla \cdot \boldsymbol{\sigma} + \mathbf{f}_{ext}\end{aligned}\tag{4.6}$$

The inertial term in the momentum balance may be dropped, since inertia effects are negligible in the overdamped limit. Distribution of filament orientations needs not be taken into account since all actin filaments in a muscle fiber are oriented along the same line and there are, on average, equally many filaments pointing in either direction along the line. In order to proceed, constitutive equations are required to relate the stress $\boldsymbol{\sigma}$ and the external force density experienced by the fiber \mathbf{f}_{ext} to the fiber density ρ and velocity \mathbf{v} . To this end, it must be noted that entropy production in the system is given by

$$\frac{d}{dt} F = - \int [\boldsymbol{\sigma} : \nabla \mathbf{v} + r \Delta \mu]\tag{4.7}$$

where r is the rate of ATP hydrolysis and μ is the difference in chemical potential of ATP with its hydrolysis products. The integrand of (4.7) is a quadratic form, each term being a product of a generalized thermodynamic flux with its corresponding generalized thermodynamic force. Provided that the system is close to thermodynamic equilibrium, the relation between the thermodynamic fluxes and thermodynamic forces is linear to a good approximation. Hence

$$\boldsymbol{\sigma} = \zeta \mathbf{I} \Delta \mu + \xi \nabla \mathbf{v} \quad .\tag{4.8}$$

Here \mathbf{I} denotes unity tensor, ζ and ξ are phenomenological parameters. Plausibly, ζ , coupling stress generation to ATP hydrolysis, increases with density ρ , since higher density results in higher motor-filament overlap. Hence, to linear order $\zeta = \zeta_0 + \zeta_1\rho$. External forces may be related to density by $\partial_t \mathbf{f}_{ext} = -\eta_e \partial_t \rho / \rho_0$, describing fiber friction with surrounding stationary fluid. Substituting the constitutive equation (4.8) into the momentum balance in (4.6), linearizing ρ around equilibrium density ρ_0 and using mass conservation one obtains:

$$\rho_0 \Delta \mu \zeta_1 \partial_x^2 \rho - \xi \partial_t \partial_x^2 \rho = \eta_e \partial_t \rho \quad . \quad (4.9)$$

This is a simple hydrodynamic description of muscle dynamics, capable of accounting for active contraction. Equations have been restricted to one dimension since muscle fibres can only contract along their length.

This example illustrates the major ingredients of the approach. Dynamics is derived by combining conservation laws with constitutive relations, that are obtained by assuming linear force-flux relation in the vicinity of equilibrium. The approach is general, allowing to describe a large variety of systems, ranging from muscles to actin-myosin gels [13, 21]. The major weaknesses are those shared by all phenomenological approaches: large number of phenomenological parameters and the difficulty of relating them to microscopic parameters of the system. Further, in many cases assumption of local equilibrium is arguable.

The approach has been applied to descriptions of motor-filament systems in [44, 42], where it was shown that the basic hydrodynamic formulation exhibits patterns of asters, vortices and spirals. This theory was adopted to study contractility and retrograde flow in a lamellipodium, i.e., flat protrusion of a crawling cell, [43], and to shape oscillations in fibroblast cells [71]. The method is extended to a three-fluid systems in [35].

Herewith, all currently available theoretical approaches to the cytoskeleton are covered. Some aspects of cytoskeletal dynamics such as contractility and force generation have received considerable attention on the theoretical side. However, they most certainly do not suffice to describe a great number of fascinating biological processes. A variety of cellular phenomena such as the above-described pigment condensation in melanophore fragments or generation of cellular protrusions such as cilia and microvilli rely on tread-

milling. Generically, treadmilling results in dynamic change of length of a filament. None of the above-mentioned mesoscopic approaches accounts for dynamic filament length though. Applying any continuum cytoskeleton description to cell locomotion requires considering boundary conditions at the gel-membrane interface. However, boundary conditions for mesoscopic coarse grained equations of cytoskeletal dynamics have never been considered. These two problems are the subject of present thesis.

5 Dynamics of treadmilling filaments, regulated by actively transported nucleator proteins

In the previous section we have seen that treadmilling is an important ingredient of many biologically vital processes. In particular it is essential for virtually all forms of cell locomotion. Furthermore, it is implicated in generation of various cellular appendages, e.g. stereocilia [70] and microvilli [29, 65]). In experiments of Rodionov *et. al.* on fish melanophores treadmilling was cleanly separated from other cellular processes that typically influence filament dynamics, making melanophore system particularly suitable for theoretical analysis [67, 90, 54]. Motivated by the experiments of Rodionov *et. al.*, this section treats a system of treadmilling filaments that are nucleated by proteins, actively transported along the filaments. We shall start with considering the filament length dynamics, neglecting spatial variations of filament density. Next we shall introduce length dependence in the filament concentration and consider a system that can be treated exactly. Then we shall develop an approximation, allowing to consider a broader class of systems and compare the results of this approximation to the exact solutions.

5.1 Simplified description: constant filament length

We start our investigations of the effects of filament treadmilling in the presence of nucleating proteins by considering the case of a mono-disperse solution of filaments with length ℓ . Although certain aspects of this model lack physical justification, it is formally much simpler to treat than the full case.

5.1.1 Dynamic equations

With the dynamics of microtubules in mind, which have a persistence length of about a millimeter, we treat the filaments as rigid rods. The position in space of a filament is thus completely specified by the position of one point along the filament, say the plus-end, and its orientation $\hat{\mathbf{u}}$, where $|\hat{\mathbf{u}}|^2 = 1$ points into the direction of the plus-end.

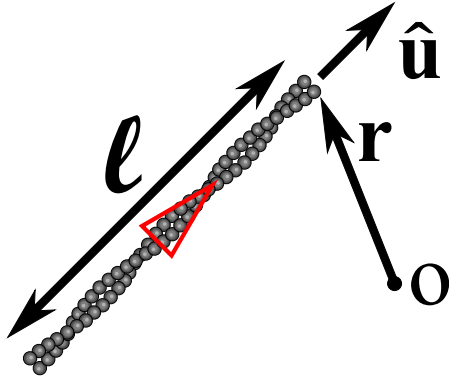


Figure 17: Illustration of coordinates, describing the state of a filament, confined to a plane: coordinate of the plus-end \mathbf{r} , orientation $\hat{\mathbf{u}}$ and length ℓ .

The dynamics of the system will be given in terms of mean-field equations. Correspondingly, the state of the system is given by filament densities. The density $c(\mathbf{r}, \hat{\mathbf{u}}, t)$ denotes the concentration of filament plus-ends at position \mathbf{r} and time t belonging to filaments of orientation $\hat{\mathbf{u}}$ with $\hat{\mathbf{u}}^2 = 1$. Of course, we might also have chosen to localize the filaments by their minus-ends. The evolution in time of the

density c is governed by

$$\partial_t c = -\nabla \cdot \mathbf{j}_f + S \quad , \quad (5.1)$$

where \mathbf{j}_f is the filament current and S combines source and sink terms resulting from filament nucleation and catastrophes.

The filament current \mathbf{j}_f is for one due to treadmilling with velocity v in the direction of the filament axis. Furthermore, there is a diffusion term with effective diffusion constants which account for the fluctuations in the system and are not only due to thermal noise. The expression for the translational current thus reads

$$\mathbf{j}_f = -D\nabla c + v\hat{\mathbf{u}}c \quad , \quad (5.2)$$

where, for simplicity, we consider the case of an isotropic diffusion constant D . Again for simplicity, we will neglect in the following rotational diffusion. We have checked, that our results stay qualitatively the same in the presence of rotational diffusion.

The polymerization-depolymerization dynamics of the filaments also contributes to the source term S in Eq. (6.1). The disassembly of a filament following a catastrophe is captured by degradation of filaments with rate ν_d . This is equivalent to assuming that it occurs on much faster time-scales than the other relevant processes. Nucleation of new filaments is proportional to the local density n of nucleating proteins. This form is justified if filaments reach their final length ℓ in a time that is fast compared to other processes.

We thus have

$$S = -\nu_d c + \nu n \quad , \quad (5.3)$$

where ν is the nucleation rate by a single nucleating protein.

The dynamics of the nucleators is governed by the continuity equation

$$\partial_t n = D_n \nabla^2 n - \nabla \cdot \mathbf{j}_{\text{act}} \quad . \quad (5.4)$$

The diffusion term with the effective diffusion constant D_n accounts for fluctuations in the system, while the current \mathbf{j}_{act} describes active transport of nucleators along filaments with velocity v_n . Within the mean-field approach, the direction of nucleator transport at a given point is determined by the averaged orientation of filaments at this point. For a system in d spatial dimensions, we therefore write

$$\mathbf{j}_{\text{act}}(\mathbf{r}) = v_n n(\mathbf{r}) \int_0^\ell d\xi \int \xi^{d-1} d\hat{\mathbf{u}} \hat{\mathbf{u}} c(\mathbf{r} + \xi \hat{\mathbf{u}}, \hat{\mathbf{u}}) \quad . \quad (5.5)$$

Together, Eqs. (6.1)-(5.5) define a minimal model of filament treadmilling in the presence of nucleators that are transported along filaments.

While it is in principle possible to analyze these equations directly, it is convenient to focus attention on the macroscopic density and polarization fields and to study the large scale behavior by coarse graining. Technically this is achieved by first performing a moment expansion of the density c in $\hat{\mathbf{u}}$. The first two moments are

$$\rho(\mathbf{r}, t) = \int d\hat{\mathbf{u}} c(\mathbf{r}, \hat{\mathbf{u}}, t) \quad (5.6)$$

$$\mathbf{p}(\mathbf{r}, t) = \int d\hat{\mathbf{u}} \hat{\mathbf{u}} c(\mathbf{r}, \hat{\mathbf{u}}, t) \quad . \quad (5.7)$$

where ρ is the density of filament ends and \mathbf{p} the average orientation (or polarization) of filaments. These quantities are determined by the two lowest-order Fourier harmonics of filament density c , which is, by definition, a 2π -periodic function of the filament orientation. Higher moments can be considered but we restrict attention to the first two. This is admissible, provided that filament orientation distribution does not exhibit abrupt variation and is well approximated by two first Fourier harmonics. Knowing all moments, the full distribution can be obtained. In the following we will restrict attention to

systems in two dimensions. In this case, the filament distribution is approximately given by $c(\mathbf{r}, \mathbf{p}) \simeq \{\rho(\mathbf{r}) + 2\hat{\mathbf{u}} \cdot \mathbf{p}(\mathbf{r})\} / 2\pi$. After coarse graining, the dynamic equations for the density and the polarization then read

$$\partial_t \rho = \nabla^2 \rho - \bar{v} \nabla \cdot \mathbf{p} + \bar{v} n - \rho \quad (5.8)$$

$$\partial_t \mathbf{p} = \nabla^2 \mathbf{p} - \frac{\bar{v}}{2} \nabla \rho - \mathbf{p} \quad . \quad (5.9)$$

Here, we have expressed the equations in dimensionless form with densities $\bar{\rho} = \ell^{-2} \rho$, $\bar{\mathbf{p}} = \ell^{-2} \mathbf{p}$, and $\bar{n} = \ell^{-2} n$, where in the above equations we have omitted the bars for simplicity. The dimensionless parameters are $\bar{v} = v / (D\nu_d)^{1/2}$ and $\bar{v} = 2\pi\nu / \nu_d$. Time has been scaled by ν_d and space by $(D/\nu_d)^{1/2}$.

Next, the moment expansion is applied to the evolution equation (5.4) of the nucleator density. After coarse graining, it reads in dimensionless form

$$\partial_t n = \bar{D}_n \nabla^2 n - \nabla \cdot \bar{\mathbf{j}}_{\text{act}} \quad (5.10)$$

with the active nucleator current given by

$$\bar{\mathbf{j}}_{\text{act}} = \frac{1}{2} \bar{v}_n n \left\{ \mathbf{p} + \frac{\bar{\ell}}{3} \nabla \rho + \frac{\bar{\ell}^2}{16} \nabla \cdot \gamma \right\} \quad . \quad (5.11)$$

The dimensionless parameters are $\bar{D}_n = D_n / D$, $\bar{v}_n = v_n / (4D\nu_d)^{1/2}$, and $\bar{\ell} = \ell(\nu_d / D)^{1/2}$. The tensor γ has components

$$\gamma_{ij} = \frac{\partial p_i}{\partial x_j} + \frac{\partial p_j}{\partial x_i} + \delta_{ij} \nabla \cdot \mathbf{p} \quad , \quad (5.12)$$

where $i, j = 1, 2$, and $(\nabla \cdot \gamma)_j = \partial \gamma_{1j} / \partial x_1 + \partial \gamma_{2j} / \partial x_2$. Equations (5.8)-(5.12) describe the evolution of the filament density and polarization and of the nucleator density on large length scales.

5.1.2 Results

We start our analysis of Eqs. (5.8)-(5.12) by noting that the homogeneous isotropic state with $n \equiv n_0 = \text{const}$, $\rho \equiv \rho_0 = \bar{v} n_0$, and $\mathbf{p} = 0$ is a stationary solution. The stability of this state against small perturbations is assessed by a linear stability analysis. To this end we form the vector $\mathbf{E} = (n, \rho, p_x, p_y)$. Assuming periodic boundary conditions and substituting a solution of the

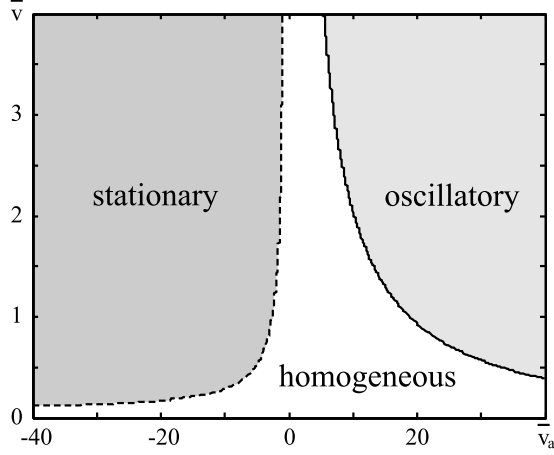


Figure 18: Stability diagram of treadmilling filaments of constant length in the presence of nucleators. The homogeneous isotropic state is stable in the white region. Along the dashed line the system encounters a stationary instability, oscillatory instabilities are encountered along the full line. In both cases, the instability is sub-critical and long wave-length. In the dark-gray shaded region asters are generated, oscillatory states are found in the region shaded in light gray. Parameters are $\bar{v} = 1.41 \cdot 10^3$, $\bar{D}_n = 0.2$, $\bar{\ell} = 1.64 \cdot 10^{-2}$, $n_0 = 0.908$.

form $\mathbf{E} = \mathbf{E}_0 + \mathbf{A} \exp\{i(k_1 x + k_2 y + \omega t)\}$, where $\mathbf{E} = (n_0, \rho_0, 0, 0)$, the amplitude \mathbf{A} is determined up to linear order by the eigenvalue equation $\lambda \mathbf{A} = \Lambda \mathbf{A}$. The matrix Λ has components

$$\begin{aligned} \Lambda_{11} = \Lambda_{22} = \Lambda_{33} &= 1 - k_1^2 - k_2^2 & \Lambda_{44} &= -\bar{D}_n(k_1^2 + k_2^2) \\ \Lambda_{12} = 2\Lambda_{21} &= -i\bar{v}k_1 & \Lambda_{13} = 2\Lambda_{31} &= -i\bar{v}k_2 & \Lambda_{14} &= \bar{v} \\ \Lambda_{23} = \Lambda_{24} = \Lambda_{32} = \Lambda_{34} &= 0 \\ \Lambda_{41} &= \frac{1}{3}\bar{v}_n n_0 \bar{\ell}(k_1^2 + k_2^2) \\ \Lambda_{42}/k_1 = \Lambda_{43}/k_2 &= i\bar{v}_n n_0 \left[\frac{3}{16}\bar{\ell}^2(k_1^2 + k_2^2) - 1 \right] \end{aligned}$$

If for all modes $\text{Re}\lambda < 0$, then a small perturbation will decay and the homogeneous isotropic state is stable. If $\text{Re}\lambda > 0$ for some mode, then the corresponding mode will grow and a heterogeneous and/or anisotropic state will appear.

In Figure 18 we present the stability diagram as a function of the pa-

rameters \bar{v} and \bar{v}_n . For sufficiently large negative motor velocities \bar{v}_n , i.e., if nucleators are transported sufficiently fast towards the shrinking filament end, a real eigenvalue λ becomes positive.

At the dashed line indicated in the diagram, the system exhibits a long-wave instability: the wave-vector of the critical eigenmode has a modulus of $2\pi/L$, where L is the system size. The four independent modes corresponding to wave-vectors $\mathbf{k} = (k_x, k_y) = (\pm 2\pi/L, 0)$ and $(0, \pm 2\pi/L)$ simultaneously become unstable. The four-fold degeneracy is a consequence of the mirror symmetry $\mathbf{x} \rightarrow -\mathbf{x}$ and $\mathbf{p} \rightarrow -\mathbf{p}$ exhibited by the dynamic equations (5.8)-(5.12). The critical eigenmode is such that the polarization vector \mathbf{p} points into the same direction as the wave-vector \mathbf{k} . The filament density ρ is in phase with the nucleator density n , but shifted a quarter period with respect to the non-vanishing component of the polarization. There is a second critical value $\bar{v}_{n,c}$ of the velocity \bar{v}_n for which the homogeneous isotropic state becomes unstable, but with $\bar{v}_n > 0$, see the full line in Fig. 18. In this case, an oscillatory solution emerges as indicated by the non-vanishing imaginary part of the critical eigenvalue λ . The linear analysis indicates a standing wave solution.

Numerical integration of the dynamic equations (5.8)-(5.12) confirms the linear analysis. In the light gray region presented in Fig. 18 the system evolves into a stationary state with the nucleators accumulated at one point. The filaments accumulate at the same point pointing radially outwards from the point of maximum density, see Fig. 19.

These solutions we call asters. Similar structures have been found in systems of filaments and motors, where motors induce active cross-links between filaments that move filaments with respect to each other [58, 74, 15, 87]. Initially, several asters may be formed but with time the pattern coarsens and eventually one aster remains. In the dark gray region shown in Fig. 18, oscillatory solutions are present, see Fig. 20. At some point in time they look like asters, but with the polarization vectors pointing towards the maximum nucleator and filament density. Then, the distribution broadens and the densities simultaneously decrease in the middle of the aster, such that the whole structure gradually deforms into a ring. The ring expands and, due to the periodic boundary conditions, a new peak is formed, now with the polarization vector pointing outwards of the aster. Then, the process repeats.

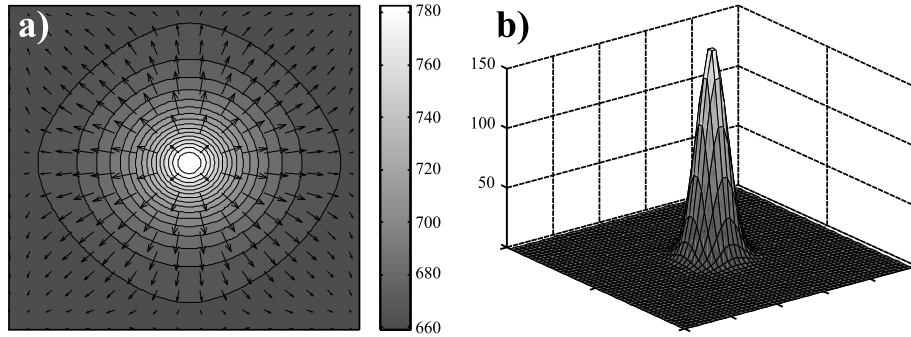


Figure 19: Stationary solution to the dynamic equations (5.8)-(5.12). **(a)** filament density ρ and polarization \mathbf{p} . **(b)** Density of nucleators n . Parameters are as in Fig. 18, $\bar{v} = 6.7$, $\bar{v}_n = 13.4$, the system is quadratic with periodic boundary conditions and length $\bar{L} = 0.89$.

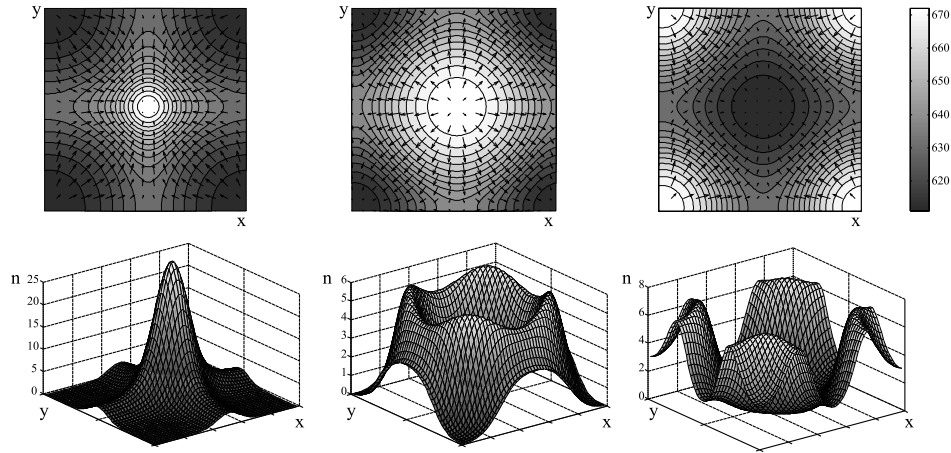


Figure 20: Oscillatory solution to the dynamic equations (5.8)-(5.12). Density of nucleators n (lower panel), filament density ρ and polarization \mathbf{p} (upper panel) for three successive time points. The right state is the same as the left, but half a system size shifted in x - and y -direction. Parameters are $\bar{v} = 1.41 \cdot 10^3$, $\bar{D}_n = 0.5$, $\bar{\ell} = 2.59 \cdot 10^{-2}$, $n_0 = 0.908$, $\bar{v} = 10.6$, $\bar{v}_n = 21.2$ and the system is quadratic with periodic boundary conditions and length $\bar{L} = 1.41$.

5.2 Varying length distributions: exact treatment

We will now turn to the case, where the two ends of a filament may vary independently of each other. This requires to keep track of the distribution of filament lengths at each point in space and for each filament orientation. The corresponding density of filament plus-ends will be denoted by $c(\mathbf{r}, \hat{\mathbf{u}}, \ell, t)$. We will first discuss the dynamics of filament lengths independently of the spatial dynamics of the filaments. We will then introduce equations, describing the dynamics of the full filament distribution, which depends on the location in space, the filament orientation, and the filament length. We finally analyze the dynamics of such a system in the presence of nucleating proteins.

5.2.1 Dynamics of filament length

The filament length changes by addition and removal of subunits, which we assume to lengthen or shorten the filament by an amount δ . For simplicity, we will focus on the case that at the plus-end, subunits can only be added, while at the minus-end, they are only removed. In absence of any other effects on polymerization and depolymerization, filaments would thus grow indefinitely if the rate of subunit addition exceeds that of subunit removal, while they would shrink to zero length in the opposite case. Motivated by microtubule catastrophes, which cause a rapid depolymerization at the plus-end, we will consider that filaments instantaneously dissolve at rate ν_d as introduced in the previous section.

The filament length distribution is naturally described by a discrete distribution c_i , $i = 0, 1, 2, \dots$. Here, c_0 is the number of filament nuclei and c_i the number of nuclei with i subunits attached. If monomers attach to the plus-end at rate k_a and detach at rate k_d , then the length of a filament changes as

$$\frac{d}{dt}c_i = -k_a c_i + k_a c_{i-1} - k_d c_i + k_d c_{i+1} - \nu_d c_i \quad (5.13)$$

for $i > 0$. In general, the rates k_a and k_d depend on the concentration of free subunits, the concentrations of other cytoskeletal proteins affecting subunit attachment and detachment, as well as physical parameters like temperature or pH. In the following, we will assume that the dynamics occurs in presence of a subunit reservoir as well as under constant physical conditions and take these rates to be constant.

It remains to fix the number of polymerization nuclei c_0 . The formation of a nucleus depends on a number of parameters as the number of subunits forming a nucleus, possible substeps necessary for its formation, the presence of nucleating proteins and so on. In this section, we consider a situation in which there are processes that keep the density of nuclei at a fixed ratio of the density n of nucleating proteins, i.e., $c_0 = \alpha n$, where without loss of generality we choose $\alpha = 1$.

On length scales much larger than the elongation δ upon addition of a subunit, the set of equations (5.13) can be approximated by the following partial differential equation

$$\partial_t c = -\partial_\ell(v_a - v_d)c - \nu_d c \quad , \quad (5.14)$$

where $v_a = k_a \delta$ and $v_d = k_d \delta$ are the growth and shrinkage velocities of the plus- and the minus-end, respectively. The boundary condition at $\ell = 0$ is $c(0) = n$. The stationary solution of Eq. (5.14) is given by

$$c(\ell) = n \exp\left(-\frac{\nu_d}{v_a - v_d} \ell\right) \quad . \quad (5.15)$$

The average length $\langle \ell \rangle = (v_a - v_d)/\nu_d$ is inversely proportional to the catastrophe rate ν_d and proportional to the difference of the growth and the shrinkage velocity $v_a - v_d$. If $v_d > v_a$ then filaments do not grow and are all of length zero.

5.2.2 Including space dependence

We are now in a place to give the equations governing the time evolution of the density c of plus-ends depending on the space coordinate \mathbf{r} , the filament orientation $\hat{\mathbf{u}}$, and the filament length ℓ . We write

$$\begin{aligned} \partial_t c(\mathbf{r}, \hat{\mathbf{u}}, \ell, t) = & D(\ell) \nabla^2 c(\mathbf{r}, \hat{\mathbf{u}}, \ell, t) - \nabla \cdot v_a \hat{\mathbf{u}} c(\mathbf{r}, \hat{\mathbf{u}}, \ell, t) \\ & - \partial_\ell(v_a - v_d)c(\mathbf{r}, \hat{\mathbf{u}}, \ell, t) - \nu_d c(\mathbf{r}, \hat{\mathbf{u}}, \ell, t) \quad . \end{aligned} \quad (5.16)$$

In this expression ∇ is the gradient operator in space. The diffusion constant D depends on the filament length ℓ , but as in the previous section we have assumed for simplicity that it is isotropic. The boundary condition in ℓ -space is chosen to be $c(\mathbf{r}, \hat{\mathbf{u}}, \ell = 0) = n(\mathbf{r})$, where n is the density of nucleating proteins.

We now specify the dynamics of the nucleating proteins. As in the previous section, we assume that the nucleating proteins are linked to motor molecules that transport them along filaments. Therefore, the evolution in time of n is again governed by Eq. (5.4), but the expression of the active current \mathbf{j}_{act} now has to account for the distribution of filament lengths:

$$\mathbf{j}_{\text{act}}(\mathbf{r}) = v_n n(\mathbf{r}) \int_0^\infty d\ell \int_0^\ell d\xi \int \xi^{d-1} d\hat{\mathbf{u}} \hat{\mathbf{u}} c(\mathbf{r} + \xi \hat{\mathbf{u}}, \hat{\mathbf{u}}, \ell) \quad . \quad (5.17)$$

As before v_n denotes the velocity of nucleating proteins bound to filaments.

5.2.3 Exact treatment

Analyzing Eqs. (5.4), (5.16), (5.17) directly by means of finite differences is unfeasible, since this would require discretizing equations on a four-dimensional grid and computing the triple integral in Eq. (5.17). However, as we shall show, Eqs. (5.4), (5.16), (5.17) can be substantially simplified without approximations, allowing for straight-forward treatment. To this end we define a new order parameter $J(\mathbf{r}, \hat{\mathbf{u}})$ according to

$$J(\mathbf{r}, \hat{\mathbf{u}}) = \int_0^\infty d\ell \int_0^\ell d\xi \xi c(\mathbf{r} + \xi \hat{\mathbf{u}}, \hat{\mathbf{u}}, \ell, t) = \int_0^\infty d\xi \int_\xi^\infty d\ell \xi c(\mathbf{r} + \xi \hat{\mathbf{u}}, \hat{\mathbf{u}}, \ell, t)$$

Substituting expression for J into (5.16) one arrives at

$$\partial_t J(\mathbf{r}, \hat{\mathbf{u}}, t) = \nabla^2 J - \nabla \cdot \hat{\mathbf{u}} \bar{v}_a J + (\bar{v}_a - \bar{v}_d) \omega - J \quad (5.18)$$

where

$$\omega(\mathbf{r}, \hat{\mathbf{u}}, t) = \int_0^\infty d\xi \xi c(\mathbf{r} + \xi \hat{\mathbf{u}}, \hat{\mathbf{u}}, \xi)$$

Henceforth, we shall render equations dimensionless with $\bar{J} = J$, $\bar{n} = \lambda^{-2}$. The dimensionless parameters are $\bar{v}_{a,d} = v_{a,d}/(D\nu_d)^{1/2}$. Time has been scaled by ν_d and space by $\lambda = (D/\nu_d)^{1/2}$. For clarity we omit writing out the bars over dynamic quantities. Substituting the expression for J into (5.16) and using

$$\int_0^\infty d\xi \xi \partial_\ell c(\mathbf{r} + \xi \hat{\mathbf{u}}, \hat{\mathbf{u}}, \xi) = \int_0^\infty \xi \left[\frac{d}{d\xi} c - \nabla \cdot \hat{\mathbf{u}} c \right] =$$

$$- \int_0^\infty c(\mathbf{r} + \hat{\mathbf{u}} \xi, \xi) - \nabla \cdot \hat{\mathbf{u}} \omega$$

we arrive at

$$\partial_t \omega = \nabla \omega + (\bar{v}_a - \bar{v}_d) s - \bar{v}_d \nabla \cdot \hat{\mathbf{u}} \omega - \omega \quad , \quad (5.19)$$

where s is

$$s(\mathbf{r}, \hat{\mathbf{u}}, t) = \int_0^\infty d\xi c(\mathbf{r} + \hat{\mathbf{u}} \xi, \hat{\mathbf{u}}, \xi, t) \quad .$$

The time-evolution for s is derived analogously, yielding

$$\partial_t s(\mathbf{r}, \hat{\mathbf{u}}, t) = \nabla^2 s + (\bar{v}_a - \bar{v}_d) c_0 - \bar{v}_d \nabla \cdot \hat{\mathbf{u}} s - s \quad . \quad (5.20)$$

Here, as before, $c_0 \equiv c(\mathbf{r}, \hat{\mathbf{u}}, \ell = 0, t)$ is determined by the boundary condition $c_0 = \bar{\nu} n$, implying that the rate of nucleation of filaments is proportional to the concentration of nucleators. The dimensionless nucleation rate is $\bar{v}_d = 2\pi\nu/\nu_d$. Noting that motor flux can be written in terms of J as

$$\mathbf{j}(\mathbf{r}, \hat{\mathbf{u}}, t) = -\bar{D}_n \nabla n + \bar{v}_n n \int d\hat{\mathbf{u}} J(\mathbf{r}, \hat{\mathbf{u}}, t)$$

we arrive at a closed set of equations (5.4), (5.18)-(5.20), specifying the exact time-evolution of the order parameters J , ω , s as well as of the motor density n . The dimensionless diffusion constant is $\bar{D}_n = D_n/D$ and the nucleator velocity is $\bar{v}_n = v_n/(D\nu_d)^{1/2}$. Note, that these equations contain neither fields, depending on filament length ℓ nor integrals in ℓ or \mathbf{r} , greatly simplifying the treatment.

5.2.4 Results

Equations (5.4), (5.18)-(5.20) admit a unique homogeneous isotropic stationary solution $n = n_0$, $s = c_0(\bar{v}_a - \bar{v}_d)$, $\omega = s(\bar{v}_a - \bar{v}_d)$, $J = \omega(\bar{v}_a - \bar{v}_d)$, where the homogeneous motor density n_0 is determined by the total amount of

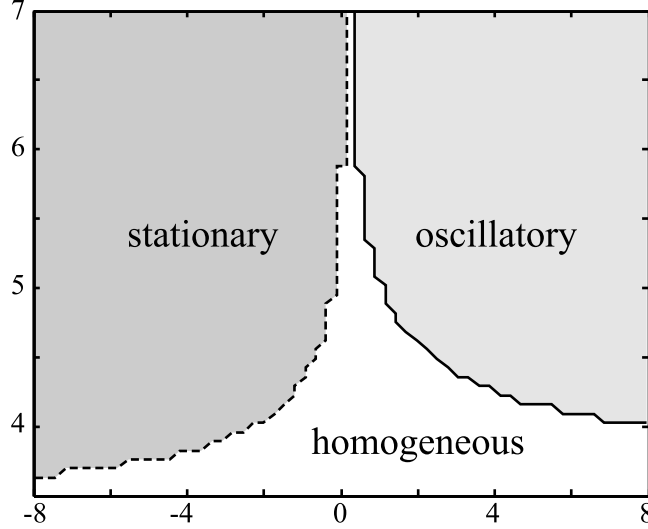


Figure 21: Stability diagram of isotropic homogeneous distribution of Eqs. (5.4), (5.18)-(5.20) for varying values of motor speed v_n and elongation speed of filament plus-end \bar{v}_a . Parameters are: $\bar{v}_d = 3.0$, $\bar{D}_n = 4.0$, $\bar{\nu} = 2\pi$, $\bar{n}_0 = 0.01$.

nucleators in the system. Linearizing dynamic equations around this state, stability diagram may be constructed, see Fig. 21. Since we wish to analyze equations (5.4), (5.18)-(5.20) exactly, we shall not coarse-grain them with respect to filament orientation θ . Hence, linearization yields one linear PDE for every θ -dependent Fourier harmonic of filament density distribution. This is easily solved by discretizing orientation θ .

Figure 21 can be compared to Fig. 18, which reports stability of the isotropic homogeneous state in the system of treadmilling filaments of constant length. Qualitatively, the results are very similar. In both cases, the homogeneous state is stable for small motor and treadmilling velocities. When the direction of motor transport coincides with that of treadmilling, the instability is oscillatory, whereas it is stationary if motors move towards the shrinking filament end.

Next, we turn to results of numerical simulations. Figure 22 shows the asymptotic state for the case of minus-end directed motor transport. It is an aster solution very similar to that, obtained in the case of constant filament

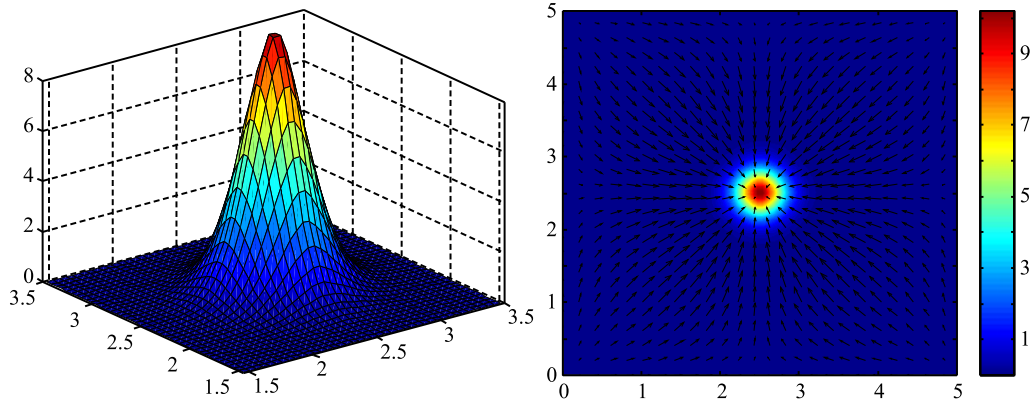


Figure 22: Aster solution of Eqs. (5.4), (5.18)-(5.20). Left: nucleator density. Right: Color plot of nucleator density superimposed with vector field $\int d\hat{\mathbf{u}}\hat{\mathbf{u}}J$, determining the nucleator flux. Parameters are $\bar{v}_d = 0$, $\bar{v}_a = 2$, $\bar{D}_n = 0.480$, $\bar{v}_n = -4.0$, $\bar{\nu} = 6.5$, $\bar{n}_0 = 1.0$, domain is square with side length 5.0.

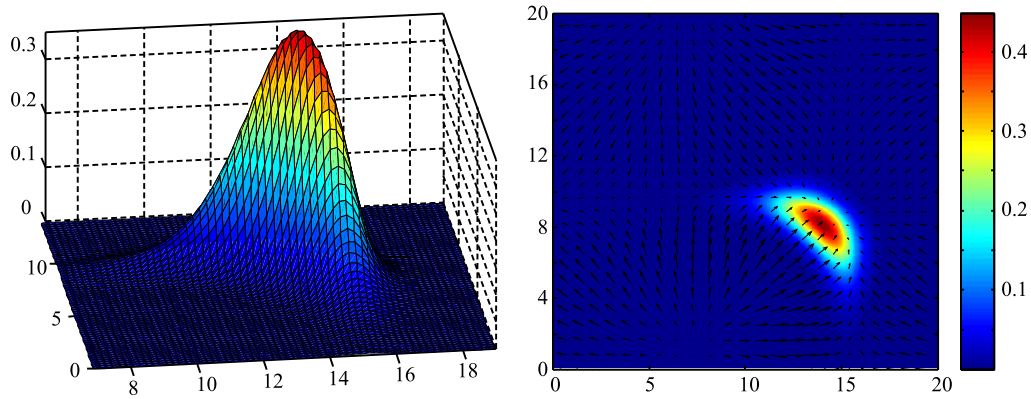


Figure 23: Solitary wave solution of Eqs. (5.4), (5.18)-(5.20). Parameters are: $v_a = 6$, $v_d = 3$, $D_n = 4$, $v_n = 1$, $\nu = 4.5$, $n_0 = 0.01$.

length. Nucleators aggregate in a peak, filaments assemble in an aster, whose center coincides with the maximum of the pigment density.

If pigment transport is directed towards filament plus-end, oscillatory states result. An example is shown in Fig. 23 (see supplementary movie M5.2.1, available at <http://www.uni-saarland.de/fak7/kruse/Konstantin/>

thesis_movies.html). In this simulation, the initial nucleator distribution was taken to be homogeneous with a small rotationally invariant gaussian perturbation in the center of the domain. The filament concentration at time $t = 0$ was set to zero. Initially, a very long-lived standing wave transient sets in. This state is qualitatively very similar to oscillatory solutions in the case of constant filament length shown in Fig. 20. After a sufficiently long time, however, the symmetry of the standing wave breaks spontaneously, turning the wave into a solitary moving crescent-shaped blob.

5.3 Moment expansion

Equation (5.16) could be treated exactly since it is linear: the dynamics of nucleators determined that of filaments through a boundary condition on c . This, however, might not hold in many applications. For example, in a system where the filament depolymerization speed v_d depends on the nucleator density n , non-linearities appear on the right-hand-side of Eq. (5.16). Thus, an exact treatment, according to the previous section is impossible. However, the equations can still be treated approximately by expanding the filament length-distribution in moments. Explicitly, we define a hierarchy of order parameters

$$\rho_i(\mathbf{r}, t) = \int_0^\infty d\ell \ell^i \int d\hat{\mathbf{u}} c(\mathbf{r}, \hat{\mathbf{u}}, \ell, t) \quad (5.21)$$

$$\mathbf{p}_i(\mathbf{r}, t) = \int_0^\infty d\ell \ell^i \int d\hat{\mathbf{u}} \hat{\mathbf{u}} c(\mathbf{r}, \hat{\mathbf{u}}, \ell, t) \quad , \quad (5.22)$$

with $i = 0, 1, 2, \dots$. Higher moments in the filament orientation could also be considered.

The different hierarchy levels i correspond to the density, the average filament length, the corresponding variance and so on. If all filaments had the same length ℓ_0 , then $c(\mathbf{r}, \hat{\mathbf{u}}, \ell, t) = c(\mathbf{r}, \hat{\mathbf{u}}, t)\delta(\ell - \ell_0)$, where δ denotes the Dirac distribution. In this case, $\rho_i = \ell_0^i \rho_0$ and $\mathbf{p}_i = \ell_0^i \mathbf{p}_0$, such that ρ_0 , \mathbf{p}_0 and the higher moments in $\hat{\mathbf{u}}$ completely describe the filament distribution.

From Eq. (5.16) we obtain the equations governing the time evolution of

density and polarization fields. They read

$$\partial_t \rho_i = \nabla^2 \rho_i - \bar{v}_a \nabla \cdot \mathbf{p}_i + i(\bar{v}_a - \bar{v}_d) \rho_{i-1} - \bar{v}(\bar{v}_a - \bar{v}_d) \delta_{i0} n - \rho_i \quad (5.23)$$

$$\partial_t \mathbf{p}_i = \nabla^2 \mathbf{p}_i - \frac{\bar{v}_a}{2} \nabla \rho_i + i(\bar{v}_a - \bar{v}_d) \mathbf{p}_{i-1} - \mathbf{p}_i \quad , \quad (5.24)$$

as is derived in App. A. In this expression, δ_{ij} is the Kronecker delta and we have rendered the densities dimensionless: $\bar{\rho}_i = \lambda^{2-i} \rho_i$, $\bar{\mathbf{p}}_i = \lambda^{2-i} \mathbf{p}_i$, and $\bar{n} = \lambda^{-2} n$ (for simplicity, the bars have been omitted in the above equations). The dimensionless parameters are $\bar{v}_{a,d} = v_{a,d}/(D\nu_d)^{1/2}$ and $\bar{v} = 2\pi\nu/\nu_d$. Time has been scaled by ν_d and space by $\lambda = (D/\nu_d)^{1/2}$. The dynamics of the nucleators is again given by Eq. (5.10), but now with the current

$$\bar{\mathbf{j}}_{\text{act}} = \frac{1}{2} \bar{v}_n n \left\{ \mathbf{p}_2 + \frac{1}{3} \nabla \rho_3 + \frac{1}{16} \nabla \cdot \gamma_4 \right\} \quad , \quad (5.25)$$

where the tensor γ_4 has components

$$\gamma_{4,ij} = \frac{\partial p_{4,i}}{\partial x_j} + \frac{\partial p_{4,j}}{\partial x_i} + \delta_{ij} \nabla \cdot \mathbf{p}_4 \quad (5.26)$$

with $i, j = 1, 2$ and dimensionless parameter $\bar{v}_n = v_n/(D\nu_d)^{1/2}$. As can be seen, the hierarchy of order parameters can be truncated at any order yielding a closed system of dynamic equations. For a consistent truncation of the moment expansion and the coarse graining, order parameters up to degree $n + 2$ have to be considered for a coarsening of degree n . Note, that if the filament distribution is approximately exponential, its n th moment is $\sim \langle \ell \rangle^n n!$ where $\langle \ell \rangle$ is mean filament length. In the moment expansion (5.25), the n th moment enters with a prefactor, resulting from Taylor-expansion of c , that falls off as $1/n!$ with increasing n . Hence, the n th term scales as $\sim \langle \ell \rangle^n$, implying that expansion converges for sufficiently small mean filament length.

5.3.1 Results

We start the analysis of Eqs. (5.10) and (5.23)-(5.26) by investigating the linear stability of the homogeneous isotropic state $n = n_0$, $\rho_0 = n_0 \bar{v} (\bar{v}_a - \bar{v}_d)$, $\rho_i = i(\bar{v}_a - \bar{v}_d) \rho_{i-1}$, for $i \geq 1$, and $\mathbf{p}_i = 0$ for $i \geq 0$. Applying the same procedure as in Sec. 5.1.2, the stability diagram is obtained, see Fig. 24. For plus-end directed nucleator velocities, $\bar{v}_n > 0$, there is a critical value $\bar{v}_{a,c}$ of

the growth velocity \bar{v}_a , at which the system encounters an oscillatory instability of the homogeneous isotropic state. For minus-end directed nucleator velocities, $\bar{v}_n < 0$ one can distinguish between two cases. For $\bar{v}_n > \bar{v}_{n,c}$ the system again encounters an oscillatory instability for some $\bar{v}_{a,c}$. For $\bar{v}_n < \bar{v}_{n,c}$, however, the instability is no longer oscillatory, but stationary heterogeneous non-isotropic states emerge.

Comparing the stability diagram of the coarse grained equations, Fig. 24, to that of the full description, Fig 21, one assesses the validity of the coarse-grained approximation. One difference is apparent: the exact description does not admit oscillatory solutions in the case of minus-end directed nucleator transport. However, in the parameter range where coarse-grained equation exhibit a fake transition, mean filament length turns comparable to characteristic scale of the pattern. Thus, in the corresponding parameter range, coarse-graining breaks down. The validity of the coarse-grained approximation can be assessed with the following "rule of thumb". One can express total number of filaments at a point in terms of the moments and their derivatives in much the same way as the pigment flux. This quantity can be calculated from solutions of coarse grained equations and is positive by definition. In the parameter range, where the coarse grained total filament density is negative, coarse grained equations are inapplicable. This is the case for values of plus-end elongation slightly above $v_{a,c}$. In parameter range, where $v_a \approx v_d$ mean filament length is very much smaller than the scale of the pattern. In this limit, the stability boundaries converge to the line $v_a = v_d$ asymptotically in the coarse-grained as well as in exact descriptions. As we shall see below, the simulations of the coarse grained equations agree very well with those of the full description in the fully nonlinear regime. In conclusion, coarse graining does converge to the full description in the case of significant scale separation, when mean filament length is well below the characteristic length of the patterns formed.

For $\bar{v}_{n,c} < \bar{v}_n < 0$, the instability occurs for a mode of a critical wavelength $|\mathbf{k}_c| \neq 0$, that is, the dynamics defines an intrinsic length scale. For nucleator velocities outside this range, we find a long-wave instability. Consequently, the wave-length of the bifurcating stationary solution is determined by the system size rather than being intrinsic to the system. Therefore, the system is likely to exhibit coarsening as will be discussed below. As in the system where filaments had constant length, the eigenmodes are fourfold degenerate due to the isotropy and space inversion symmetry of the dynamic equations. The eigenmodes are plane waves with the polarization being parallel to the

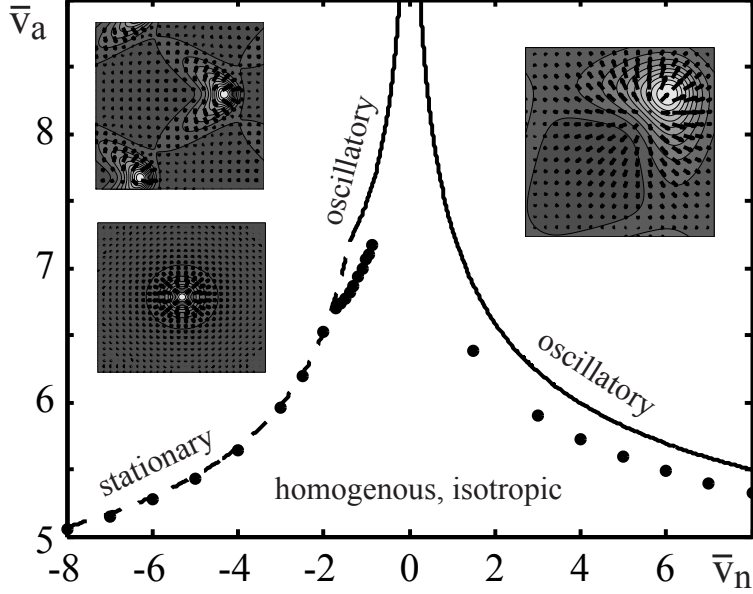


Figure 24: Stability diagram of the stationary homogeneous isotropic state of Eqs. (5.23)-(5.26) as a function of the nucleator and the polymerization velocities, \bar{v}_n and \bar{v}_a . The full lines indicate oscillatory, the dashed line stationary instabilities. Dots indicate back transitions. Insets illustrate emergent states in the non-linear regime by their filament densities and polarization fields. Parameter values are $\bar{v}_d = 3$, $\bar{D}_n = 4$, $\bar{\nu} = 2\pi$, and $n_0 = 0.01$.

mode's wave-vector, the nucleator density and the density fields ρ_i are in phase but shifted by a quarter period with respect to the polarization fields \mathbf{p}_i . The polarization fields are directed away from points of maximal density. Note, that the linear stability analysis does not hint towards isotropic heterogeneous or homogeneous anisotropic solutions.

As we have already mentioned, for $\bar{v}_n < \bar{v}_{n,c}$ the homogeneous isotropic state loses stability through a long-wave instability. Beyond the instability coarsening is expected. This is indeed the case, see Fig. 25.

Initially many small asters may be present. Eventually, however, the system will always form a single aster. In the course of time, these asters will fuse and the pattern coarsens, see Fig. 25. We investigated the coarsening in more detail by studying two interacting asters in the limiting case of vanishing

nucleator diffusion, $\bar{D}_n = 0$. In that case, the equations for the stationary state can be solved analytically by means of the Fourier-Bessel transform if one assumes rotational symmetry of the fields and that the polarization vector always points radially, see App. B for details. Furthermore, the nucleator density is assumed to be given by a δ -distribution at the center of each aster. We find solutions for all values of $\bar{v}_n < 0$.

Since Eqs. (5.23)-(5.26) are linear in this case, the fusion of two asters can be studied by calculating the velocity of the δ -peaked nucleator distribution of one aster in the filament density and polarization fields of the other aster. The result of such a calculation is presented in Fig. 25 and shows very good agreement with the numerical solution to the full equations.

For sufficiently fast plus-end directed nucleator transport and sufficiently fast plus-end elongation speeds, an oscillatory instability results. The unstable eigenfunctions are plane sine-waves with wave-numbers given by $\mathbf{k} = \{(\pm 2\pi/L, 0), (0, \pm 2\pi/L)\}$. The result of the corresponding simulation is shown in Fig. 26. The dynamics lead to formation of a localized solitary wave. Here the nucleators form a peak moving along the domain at some constant speed. The distribution of filaments is similar to that of filament concentration, see Fig. 26.

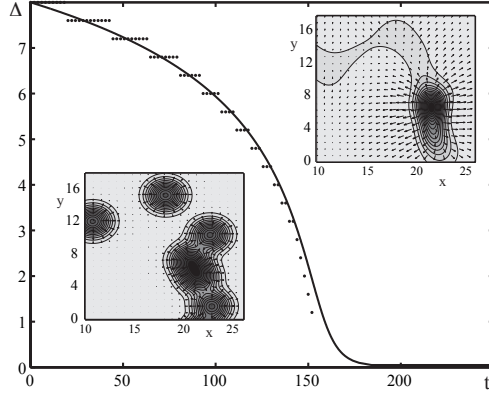


Figure 25: Coarsening in a system of treadmilling filaments. Insets: Initial state with many asters (left) and state at a later time (right). All asters have fused into one. Parameter values are $\bar{v}_a = 7$ and $\bar{v}_n = -3$. Other values are as in Fig. 24. The domain size is 30×30 . Main panel: Distance Δ of two asters as a function of time. Solid curve: analytical result for $\bar{D}_n = 0$, dots: numerical result for $\bar{D}_n = 0.03$. In both cases $\bar{v}_a = 1$, $\bar{v}_d = 0$, $\bar{v}_n = -1$, $n_0 = 1.6$.

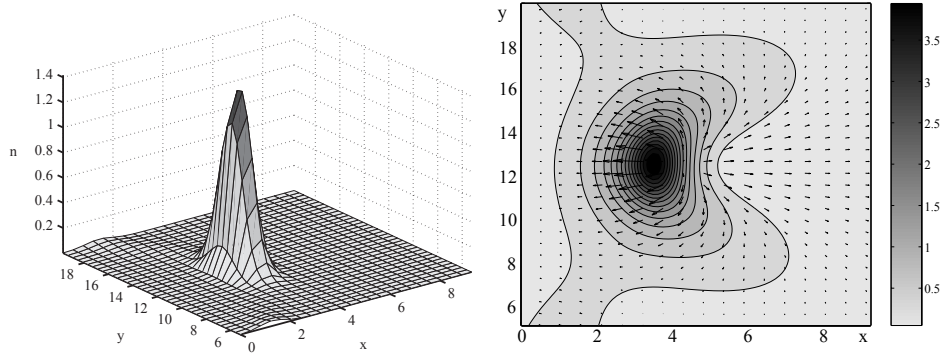


Figure 26: Snapshot of a crescent-shaped solitary wave solution to Eqs. (5.23)-(5.26). Left: nucleator density, right: grey scale coded filament density ρ_0 and polarization field \mathbf{p}_0 . The wave moves to the left. The polarization field has a singularity at the rear end, the nucleators are predominantly localized at the leading edge of the filament spot. Parameter values are $\bar{v}_a = 7$ and $\bar{v}_n = 1$. Other values are as in Fig. 24. Periodic boundaries have been employed. The domain size is 20×20 .

5.4 Capping proteins

Moment-expansion method that we have introduced above to treat systems with varying distributions of filament length can be used also to describe situations in which proteins affecting filament growth other than nucleators are present. In the following we will give the example of proteins that stabilize the minus-end by reducing the rate of subunit removal at the minus-end. In particular, we shall assume that actively transported molecules can bind (capp) the filament minus-end. As long as the minus-end is capped, polymerization does not proceed. Depolymerization resumes upon disassociation of the capping molecule from the minus-end. Dynein-dependent stabilization of microtubule minus-end by this capping mechanism has been experimentally demonstrated in [54].

The density of these proteins will be denoted s in the following. Let us first determine the fraction of time a filament end is occupied by a stabilizing protein. Let p denote the probability that this site is occupied, then $\dot{p} = \omega_a s(1 - p) - \omega_d p$, where ω_a and ω_d characterize the rates at which an empty site gets occupied and at which an occupied site gets free, respectively. Assuming that these rates are fast as compared to the other relevant processes, we can assume that locally, the probability p is in steady state. This implies $p = \omega_a s / (\omega_d + \omega_a s)$. Now, if subunits are removed only when the last site of the filament is not occupied by a stabilizing protein, then the depolymerization velocity $v_d = \delta k_d$, where k_d is the rate of subunit removal and δ the corresponding change in filament length, is given by

$$v_d(s) = \frac{v_d^0}{1 + \kappa s} \quad . \quad (5.27)$$

Here v_d^0 is the shrinkage velocity in the absence of stabilizing proteins and $\kappa = \omega_a / \omega_d$.

For convenience, the filament distribution will in the following be characterized by the density $c(\mathbf{r}, \hat{\mathbf{u}}, \ell, t)$ of minus-ends of filaments of length ℓ with orientation $\hat{\mathbf{u}}$.

The time evolution of c is governed by

$$\begin{aligned} \partial_t c(\mathbf{r}, \hat{\mathbf{u}}, \ell, t) = & \nabla^2 D c(\mathbf{r}, \hat{\mathbf{u}}, \ell, t) - \nabla \cdot v_d \hat{\mathbf{u}} c(\mathbf{r}, \hat{\mathbf{u}}, \ell, t) \\ & - \partial_\ell (v_a - v_d) c(\mathbf{r}, \hat{\mathbf{u}}, \ell, t) - \nu_d c(\mathbf{r}, \hat{\mathbf{u}}, \ell, t) \quad , \end{aligned} \quad (5.28)$$

which is essentially the same as Eq. (5.16). Importantly, however, the depolymerization velocity v_d is now given by expression (5.27) and the nucleation

rate is constant, reflecting a constant rate of spontaneous nucleation, i.e. $c(\mathbf{r}, \hat{\mathbf{u}}, \ell = 0) = c_0$. The evolution in time of the density s is given by the continuity equation $\partial_t s + \nabla \cdot \mathbf{j}_{\text{mot}} = 0$, where

$$\mathbf{j}_{\text{mot}} = v_n s(\mathbf{r}) \int_0^\infty d\ell \int_0^\ell d\xi \int \xi^{d-1} d\hat{\mathbf{u}} \hat{\mathbf{u}} c(\mathbf{r} - \xi \hat{\mathbf{u}}, \hat{\mathbf{u}}, \ell) \quad . \quad (5.29)$$

describes the transport of capping molecules by motors.

Performing a moment expansion with respect to the filament length ℓ and the orientation $\hat{\mathbf{u}}$, we arrive at a hierarchy of order parameters as in Sect. 5.3. In dimensionless form the corresponding coarse grained dynamic equations read

$$\begin{aligned} \partial_t \rho_i &= \nabla^2 \rho_i - \nabla \cdot \frac{\bar{v}_d^0}{1+s} \mathbf{p}_i + i(\bar{v}_a - \frac{\bar{v}_d^0}{1+s}) \rho_{i-1} - \\ &\quad c_0 (\bar{v}_a - \frac{\bar{v}_d^0}{1+s}) \delta_{i0} - \rho_i \quad (5.30) \\ \partial_t \mathbf{p}_i &= \nabla^2 \mathbf{p}_i - \frac{1}{2} \nabla \frac{\bar{v}_d^0}{1+s} \rho_i + i(\bar{v}_a - \frac{\bar{v}_d^0}{1+s}) \mathbf{p}_{i-1} - \mathbf{p}_i \quad , \end{aligned}$$

see App. A. In this expression, δ_{ij} is the Kronecker delta and we have rendered the densities dimensionless: $\bar{\rho}_i = \lambda^{i-2} \rho$, $\bar{\mathbf{p}} = \lambda^{i-2} \mathbf{p}$, and $\bar{n} = \kappa n$ (for simplicity, the bars have been omitted in the above equations). The dimensionless parameters are $\bar{v}_a = v_a / (D\nu_d)^{1/2}$, $\bar{v}_d^0 = v_d^0 / (D\nu_d)^{1/2}$ and $\bar{\nu} = 2\pi\nu / \nu_d$. Time has been scaled by ν_d and space by $\lambda = (D/\nu_d)^{1/2}$. The dynamics of the nucleators is again given by Eq. (5.10), but now with the current

$$\bar{\mathbf{j}}_{\text{act}} = \frac{1}{2} \bar{v}_n s \left\{ \mathbf{p}_2 - \frac{1}{3} \nabla \rho_3 + \frac{1}{16} \nabla \cdot \gamma_4 \right\} \quad , \quad (5.31)$$

where the tensor γ_4 has components

$$\gamma_{4,ij} = \frac{\partial p_{4,i}}{\partial x_j} + \frac{\partial p_{4,j}}{\partial x_i} + \delta_{ij} \nabla \cdot \mathbf{p}_4 \quad (5.32)$$

with $i, j = 1, 2$ and dimensionless parameters $\bar{v}_n = v_n / (D\nu_d)^{1/2}$. As before the hierarchy of order parameters can be truncated at any order yielding a closed system of dynamic equations. For consistent truncation of the moment expansion and the coarse graining, order parameters up to degree $n+2$ have to be considered for a coarsening of degree n .

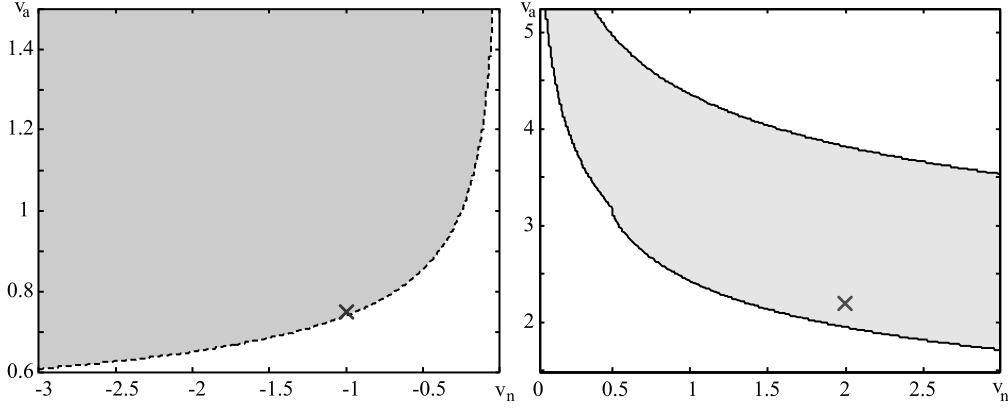


Figure 27: Stability of the homogeneous isotropic state in a system of tread-milling filaments with minus-end capping. Right: oscillatory instabilities (solid lines), in the case of plus-end directed transport of capping proteins. Note that homogeneous isotropic state is stable for sufficiently large value growth at the plus-end \bar{v}_a . Parameters are: $\bar{v}_d^0 = 0.88$, $\bar{D}_n = 1.5$, $\bar{c}_0 = 1$. The gray cross corresponds to parameter values for simulation in Fig. 29. Left: stationary instabilities (dashed line), for minus-end directed motor transport. Parameters are: $\bar{v}_d^0 = 0.5$, $\bar{D}_n = 1$, $\bar{c}_0 = 1$, $\bar{n}_0 = 3$. Gray cross corresponds to parameter values for simulation in Fig. 28.

The results of linear stability analysis of Eqs. 5.30, 5.31 are shown in Figure 27. As with regulatory protein promoted nucleation, we see long wave stationary instabilities in the case of minus-end directed regulatory protein current and oscillatory instabilities when assuming that the active current is plus-end directed. The corresponding numerical simulations are shown in Figs. 28 and 29. In the case of minus-end directed flux of regulatory proteins coarsening asters appear. Regulatory proteins condense into a single peak, the maximum of which is co-localized with the center of the filament aster. Interestingly, asters are different from those seen when assuming regulatory protein dependent filament nucleation: in the latter case filament polarization pointed outwards, away from the middle of the aster, whereas in the former case filament polarization is directed inwards.

Reversing the direction of active current of regulatory proteins spatially extended traveling waves much like those seen when assuming constant filament length appear (see Fig. 29).

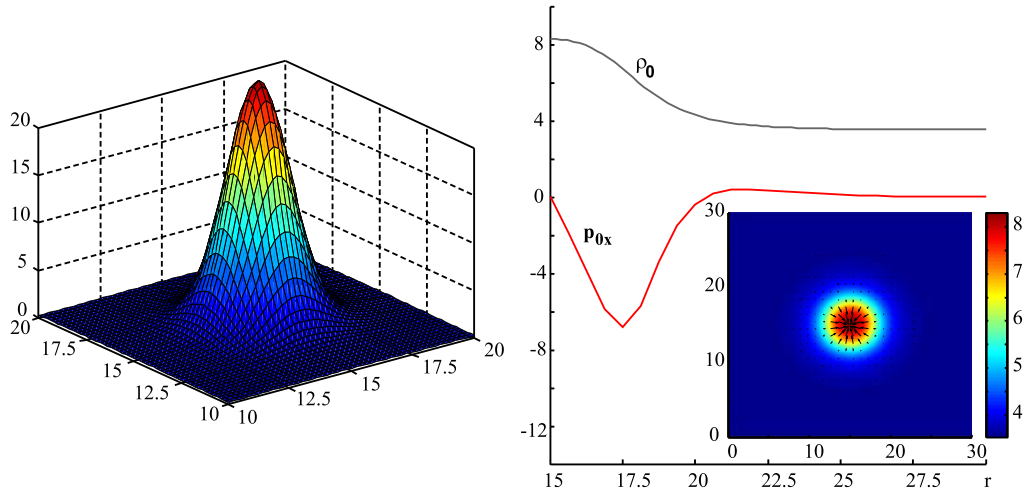


Figure 28: Aster solution in a system of treadmilling filaments, regulated by minus-end capping. Left: distribution of capping proteins. Right: profiles of filament density ρ_0 and x -component of polarization \mathbf{p}_0 versus r . Inset shows colorplot of filament density superimposed with polarization distribution. Parameters are: $\bar{v}_d^0 = 0.5$, $\bar{D}_n = 1$, $\bar{c}_0 = 1$, $\bar{n}_0 = 0.3$, $\bar{v}_n = -1$, $\bar{v}_a = 0.75$. Domain is square with side length 30.

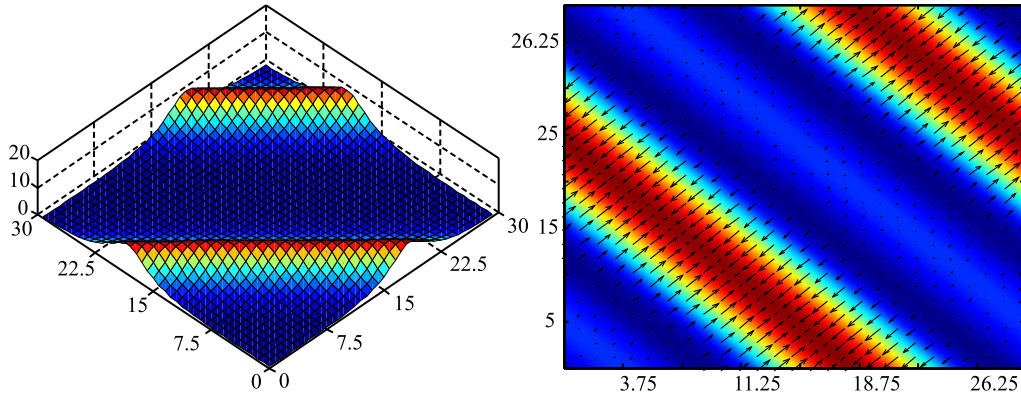


Figure 29: Plane waves in a system of treadmilling filaments and capping proteins. Left: pigment distribution. Right: colorplot of filament density, superimposed with polarization field. Parameters are: $\bar{v}_d^0 = 0.88$, $\bar{D}_n = 1.5$, $\bar{c}_0 = 1$, $\bar{n}_0 = 3$, $\bar{v}_n = 2$, $\bar{v}_a = 2.2$. Domain is square with side length 30.

5.5 Varying domain shape

In experiments with melanophores, it proved possible to examine the effects of fragment geometry on the pigment centering by manufacturing fragments of different shape [67, 68]. Motivated by this work, we shall consider descriptions of filament treadmilling regulated by actively transported proteins in varying domain geometries. We start with Eqs. (5.23), (6.7), (5.25) where actively transported molecules served filament nucleators. For convenience, we shall characterize the filament distribution by the density of filament minus-ends, rather than by the density of plus-ends as was done in section 5.3. Thus, Eqs. (5.23), (6.7), (5.25) have to be modified according to

$$\begin{aligned}\partial_t \rho_i &= \nabla^2 \rho_i - \bar{v}_d \nabla \cdot \mathbf{p}_i + i(\bar{v}_a - \bar{v}_d) \rho_{i-1} \\ &\quad - \bar{v}(\bar{v}_a - \bar{v}_d) \delta_{i0} n - \rho_i \\ \partial_t \mathbf{p}_i &= \nabla^2 \mathbf{p}_i - \frac{\bar{v}_d}{2} \nabla \rho_i + i(\bar{v}_a - \bar{v}_d) \mathbf{p}_{i-1} - \mathbf{p}_i \quad .\end{aligned}\tag{5.33}$$

The pigment flux is given by Eq. (5.31).

Introducing boundaries requires considering nucleator and filament fluxes through the domain walls. For nucleator density, we use reflecting boundary conditions, which amounts to requiring nucleator particle conservation. Supposing that filaments, facing the domain wall with their plus-ends do not polymerize, domain boundary serves an effective sink of the filament density, whose strength is determined by the treadmilling velocity. For the details on boundary conditions, used when describing dynamics in fragments of various shape, see App. C.

Figure 30 shows asymptotic density profiles obtained by integrating the equations on a disc-shaped domain. Much like in the case of periodic boundaries, filaments assemble an aster in the center of the domain whereas nucleators form a peak whose maximum coincides with polarization field singularity. As is seen from Fig. 30, the characteristic size of the nucleator as well as the filament distribution are very much smaller than the domain, implying that boundary effects are negligible in the corresponding parameter range. Hence, the state in Fig. 30 is very similar to that in the system with periodic boundaries, Fig. 22.

Figure 31 shows simulations on a dumbbell-shaped domain. The lower panel of the same figure shows corresponding experimental results, where the pigment dynamics was studied in a fragment, consisting of two larger subportions, joined by a thin "neck". Interestingly, in the experiments as well as

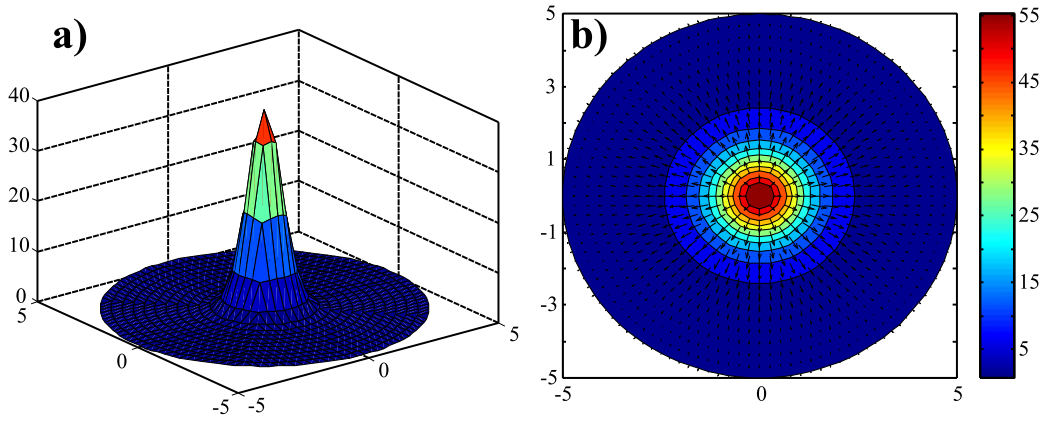


Figure 30: Aster solution on disc-shaped domain. **(a)** Nucleator density. **(b)** Colorplot of filament density superimposed with polarization distribution. Parameters are: $\bar{v}_d = 1$, $\bar{v}_a = 2$, $\bar{D}_n = 1$, $\bar{v}_n = -1$, $\bar{\nu} = 2\pi$, $n_0 = 1$.

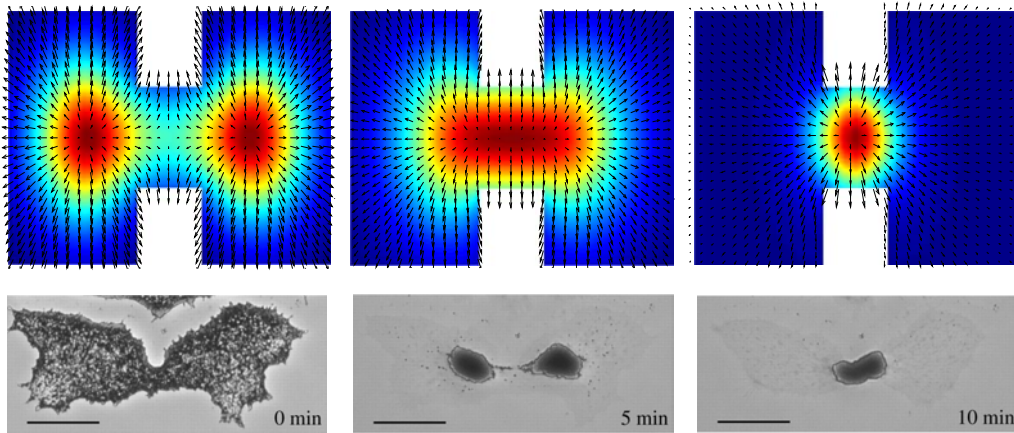


Figure 31: Colorplots of nucleator density together with polarization distributions showing dynamics in a system with actively transported nucleators in a dumbbell-shaped domain (upper panel). The three snapshots correspond to times $t = 3$, $t = 9$ and $t = 39$ (left to right). Parameters are as in Fig. 30. Lower panel illustrates the corresponding experimental results, taken from [11].

in the simulation one initially sees transient formation of two separate nucleator aggregates. Thereafter, the two blobs merge at the "neck", joining the

two larger fragment subportions. Thus, the simulation of dumbbell-shaped fragment shows good qualitative agreement with experiment. Interestingly, for sufficiently low values of nucleator diffusion and sufficiently small width of the "neck", the two asters, initially formed in the two larger subdomains, do not merge. Hence, one-aster state exhibits a bifurcation upon varying either of the two control parameters.

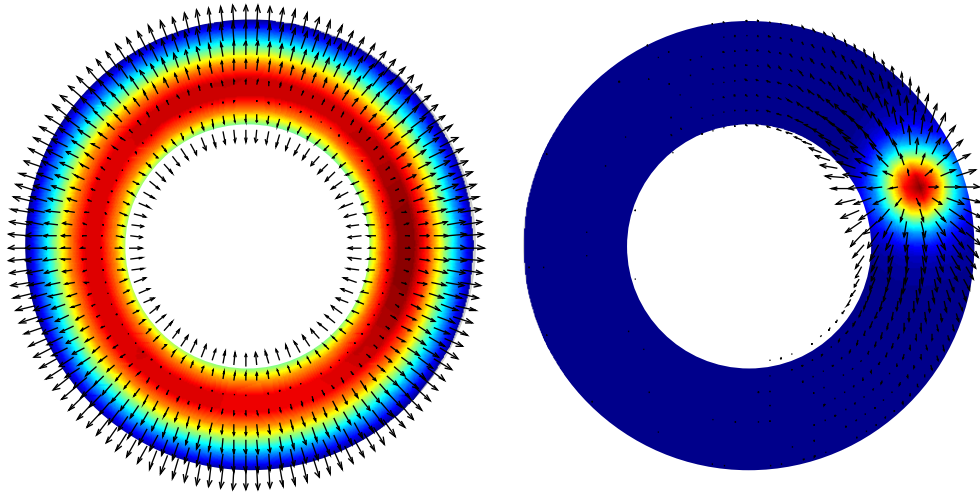


Figure 32: Nucleator density and polarization in a system with actively transported nucleators in an annular domain. Snapshots correspond to times $t = 3$ (left) and $t = 93$ (right). Initially, pigments aggregate in a ring, concentric with domain boundaries, in agreement with experimental data, shown in Fig. 10. Parameters are as in Fig. 30.

Figure 32 shows the dynamics in the case of an annular fragment geometry. Initially, nucleators are homogeneously distributed over the domain. Subsequently, they move away from the domain edges, accumulating in a ring, concentric with the boundaries. Eventually nucleator ring breaks symmetry contracting into a single blob. Corresponding experiments are shown in Fig. 10. Initially, a pigment ring forms, in accordance with experimental findings. Subsequent coarsening observed in the simulation has not been experimentally confirmed. However, time-scale of coarsening is about ten times slower than that of ring-formation. Hence, simulation results suggest that experimental observation time would need to be increased to hour in order

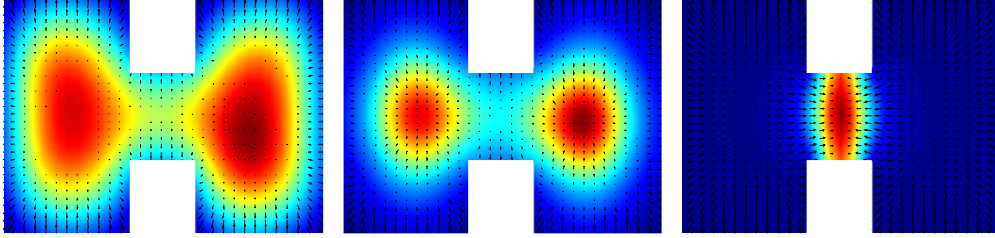


Figure 33: Density of capping molecules and polarization distribution in a system with actively transported minus-end capping proteins in a dumbbell-shaped domain. Snapshots correspond to times $t = 3$, $t = 9$ and $t = 54$ (left to right). Parameters are: $\bar{v}_d^0 = 0.5$, $\bar{D}_n = 1$, $\bar{c}_0 = 1$, $\bar{v}_n = -1$, $\bar{v}_a = 0.75$, $\bar{n}_0 = 1$.

to observe symmetry breaking causing ring contraction.

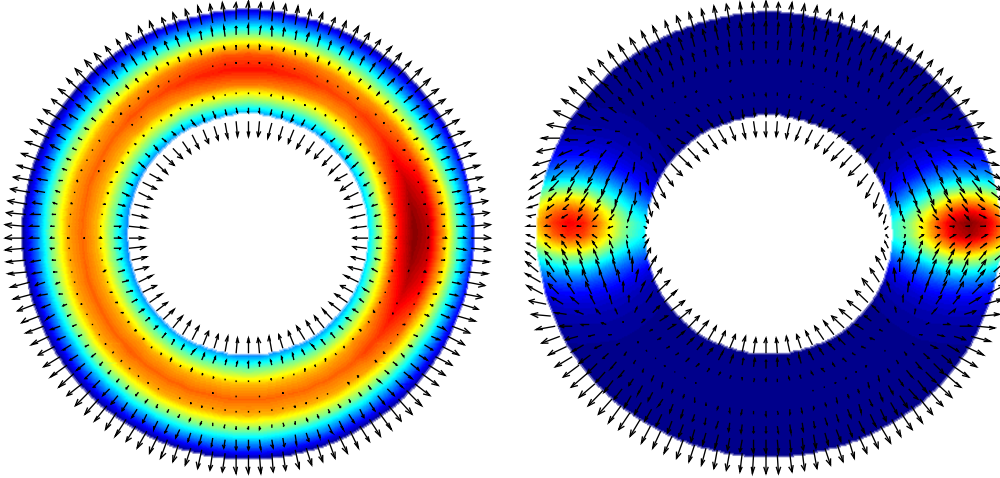


Figure 34: Density of capping proteins and polarization in a system with actively transported capping proteins in an annular domain. Parameters are as in Fig. 33.

In order to compare the description where actively transported molecules served filament nucleators to the one where they stabilized filaments by minus-end capping, we simulated Eqs. (5.30), (5.31), (5.4) in various domain geometries. Figure 33 shows simulation results for the dumbbell-shaped

domain. Initially, much like in the description with actively transported nucleators, see Fig. 31, dynamics starts with formation of two separate peaks of regulatory proteins in the two larger subportions, subsequently coarsening into a single blob at the "neck". The polarization field defects are, however, different from those shown in Fig. 31: in the vicinity of the point defect polarization points towards the maximum of regulatory protein density.

Finally, we consider simulations on an annular domain. Initially, a ring of capping proteins forms. Thereafter, the ring breaks up into several density maxima, co-localized with point defects. Again, the dynamics is rather similar in both descriptions, whereas the structure of point defects appears rather different, see Fig. 34.

5.6 Conclusions and outlook

In this section, we considered pattern formation in a system of treadmilling filaments, regulated by actively transported proteins that either nucleate filaments or that stabilize the depolymerizing minus-end. The former case admitted exact treatment due to linearity of equations governing filament dynamics. The latter case could be treated approximately by exploiting moment expansion, provided that characteristic scale of the pattern is sufficiently larger than mean filament length. Both mechanisms considered in this section are thought to be involved in pigment centring, observed in experiments with fish melanophores. Dyneins, implicated in pigment transport in melanophores, have been shown to catalyze microtubule nucleation as well as to inhibit depolymerization at the minus-end in assays *in-vitro*. Since our descriptions account for all the processes implicated in pigment dynamics in fish melanophores, it is of interest to compare simulations results to structures *in vivo*. Both mechanisms reproduce the pigment-centring effect as long as active transport is minus-end directed. If active transport is plus-end directed, simulations predict traveling waves in the case of pigment-dependent nucleation as well as in the case of pigment-dependent minus-end capping. In fact, as described in Ref. [69], it is possible to control the direction of pigment transport experimentally: if melanophore fragments are stimulated with adrenalin, pigments are transported towards the minus-end, whereas they are transported towards the plus-end upon stimulation with caffeine. It is thought that granules carry minus-end-directed dyneins as well as plus-end-directed kinesins. Reversal of transport direction upon treatment with either drug is assumed to result either from stimulation of one motor type

or inhibition of activity of the other. Caffein stimulation triggering plus-end motor transport does not result in emergence of traveling waves. This observation, however, does not contradict our findings - waves are only seen in simulations with periodic boundary conditions. When integrating the equations in confined domain, waves do not survive boundary collisions. Instead, actively transported proteins pile up along the domain rim showing no oscillatory dynamics. It would be of great interest to check experimentally for existence of traveling waves in systems of treadmilling filaments for example by reconstituting the melanophore system in a chamber whose size is much larger than that of self-organized structures, making it possible to disregard the boundary effects. Also, it would be interesting to test our predictions quantitatively, for example by comparing the simulated filament end distribution to that seen in experiments, obtained by selectively decorating microtubule plus-ends.

6 Filament treadmilling in presence of cooperatively binding nucleators

In the previous section, we considered a system where proteins that nucleate new filaments underwent directional active transport along the filaments. However, many vital biological systems exhibiting pattern-formation due to filament treadmilling are not thought to involve active transport of regulatory proteins. For example, in the experiments with human neutrophils presented in Sec. 3.5, it was shown that Hem-1, a protein that is involved in actin nucleation was not transported by a motor. Supposedly, mechanisms similar to those responsible for wave generation in neutrophils are implicated in wave generation in many other motile cell types, e.g. dictyostelids. Motivated by experimental findings of Weiner and co-workers, we turn to developing a description of treadmilling filaments, regulated by proteins that undergo cooperative binding to the membrane.

6.1 Exact treatment

The dynamics of actin and Hem-1 is schematically presented in Fig. 35. We assume that Hem-1 is inactive unless bound to the membrane adjacent to the substrate. We further suppose that binding to the membrane occurs cooperatively: the binding rate increases with the amount of Hem-1 already bound to the membrane. Active Hem-1 molecules nucleate new actin filaments, which treadmill. Finally, the presence of actin filaments on the membrane induces detachment of Hem-1 proteins. While the general form of these processes are based on the findings in Ref. [91], the actual processes in neutrophils might be different. We have checked that the basic results are independent of many of the details of the molecular interactions. For example, if the actin filaments detach together with the Hem-1 molecules from the membrane, we find qualitatively the same behavior as in the case when actin filaments stay attached to the membrane after release of Hem-1. As we will see, though, cooperative binding of Hem-1 to the membrane is indispensable for wave generation. Furthermore, we should note at this point that the process we ascribe here to Hem-1 does in fact involve a number of other proteins, as Hem-1 leads to actin filament nucleation only by activating the WAVE complex which contains, in particular, the Arp2/3 complex.

As mentioned above, in our description, we focus on the dynamics on the

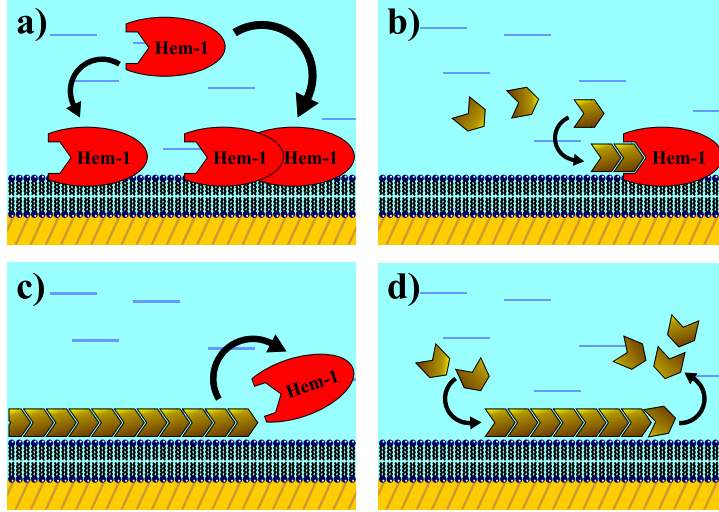


Figure 35: Illustration of Hem-1/actin dynamics. **(a)** Binding of Hem-1 to the membrane is cooperative: membrane-bound Hem-1 promotes further binding of Hem-1 proteins. **(b)** Membrane-bound Hem-1 catalyzes the nucleation of actin-filaments. **(c)** Membrane-bound Hem-1 detaches in presence of actin filaments. **(d)** Filaments on the membrane treadmill.

membrane, leading to an essentially two-dimensional system. The cytosol above the membrane is assumed to provide a reservoir of actin monomers. We describe the dynamics of treadmilling actin filaments on the membrane using the framework developed in Sec. 5. The distribution of actin filaments is given by the density c of filament plus-ends, which depends on the position \mathbf{r} , on the orientation $\hat{\mathbf{u}}$, where $|\hat{\mathbf{u}}|^2 = 1$, and on the filament length ℓ as well as on the time t . The dynamic equation for c reads

$$\partial_t c = D\Delta c - v_a \nabla \cdot \hat{\mathbf{u}} c - \partial_\ell (v_a - v_d) c - \nu_d c \quad , \quad (6.1)$$

where v_a is the polymerization velocity at the plus-end, v_d the depolymerization velocity at the minus-end, D an effective diffusion constant that accounts for fluctuations in the system, and ν_d the filament detachment rate. We do not consider rotational diffusion, which is negligible if the filament concentration is large enough. The nucleation of new filaments is accounted for by the boundary condition at $\ell = 0$. We assume that the density of nuclei is fixed by the amount of nucleators and write $c(\mathbf{r}, \hat{\mathbf{u}}, \ell = 0, t) = \nu n_b(\mathbf{r}, t)$, where n_b is the density of nucleating proteins bound to the membrane. That

is, only nucleators bound to the membrane are active. The parameter ν is a constant.

The densities n_b and n_f of proteins nucleating new filaments (Hem-1) bound and not bound to the membrane, respectively, evolve according to the equations

$$\partial_t n_f = D_f \Delta n_f - \omega_a (1 + \omega_1 n_b^2) n_f + \omega_d T_{tot} n_b \quad (6.2)$$

$$\partial_t n_b = D_b \Delta n_b + \omega_a (1 + \omega_1 n_b^2) n_f - \omega_d T_{tot} n_b \quad (6.3)$$

Here, ω_a and ω_d , respectively, denote the rates of attachment to and detachment from the membrane. The term $\omega_1 n_b^2$ accounts for cooperativity during binding of nucleators to the membrane. As we will show below, this term is the lowest order term that is able to generate an instability of the homogeneous isotropic state. The parameters D_f and D_b are again effective diffusion constants that account for fluctuations in the system. Finally, $T_{tot}(\mathbf{r})$ denotes the amount of actin filaments overlapping with a point \mathbf{r} in space

$$T_{tot} = \int_0^\infty d\ell \int_0^\ell d\xi \int d\hat{\mathbf{u}} c(\mathbf{r} + \xi \hat{\mathbf{u}}, \hat{\mathbf{u}}, \ell) \quad (6.4)$$

This completes the specification of the dynamic equations.

Eq. (6.1) does not involve products of functions of ℓ or \mathbf{r} . Thus, an exact treatment as presented in Sec. 5.2 is possible, yielding equations, determining time evolution of T_{tot} that read

$$\begin{aligned} \partial_t T(\mathbf{r}, \hat{\mathbf{u}}) &= D \nabla^2 T - \nabla \cdot v_a \hat{\mathbf{u}} T + \omega v_a - \nu_d T \\ \partial_t s(\mathbf{r}, \hat{\mathbf{u}}) &= D \nabla^2 s + \nu v_a n_b - \nu_d s \end{aligned} \quad (6.5)$$

where $T = \int_0^\infty d\ell \int_0^\ell d\xi c(\mathbf{r} + \hat{\mathbf{u}}\xi, \ell)$, $s = \int_0^\infty d\xi c(\mathbf{r} + \hat{\mathbf{u}}\xi, \xi)$. Note that the total number of filaments T_{tot} in Eq. (6.4) is obtained from T by $T_{tot}(\mathbf{r}) = \int d\hat{\mathbf{u}} T(\mathbf{r}, \hat{\mathbf{u}})$.

From now on, we will use a rescaled version of the dynamic equations containing only dimensionless quantities. To this end space is scaled by $(D_f/\nu_d)^{1/2}$, time by ν_d^{-1} , the density of filament centers by $\nu_d^2/\omega_d D_f$, and the nucleator concentrations by $\nu_d^3 (D_f/\nu_d)^{1/2}/v_a \nu \omega_d D_f$.

We start our investigations of the dynamic Eqs. (6.2), (6.3) and (6.5) by assessing the linear stability of the isotropic homogeneous stationary

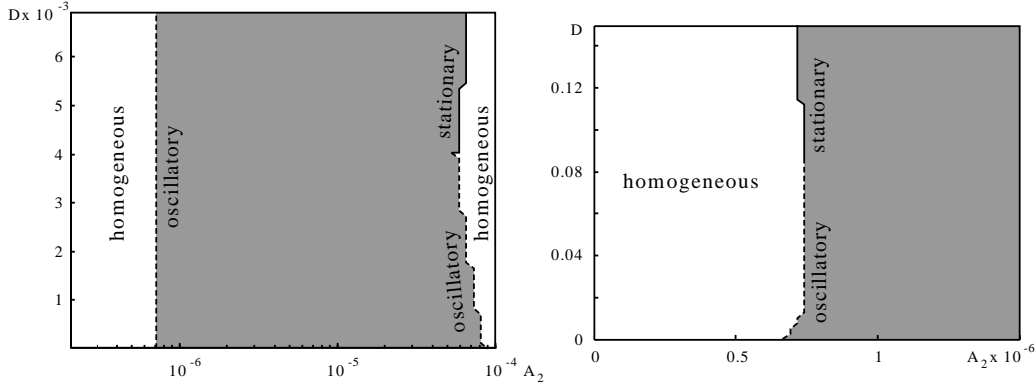


Figure 36: Stability diagram of the homogeneous isotropic stationary state in the full description. Regions of stability are indicated in light gray, regions of instability in dark gray. Dashed lines mark oscillatory instabilities, full lines stationary instabilities. The right panel is a magnification of the lower left corner of the left panel. Parameters are $D_b = 0.01$, $\omega_a = 0.170$, $v_a = 1.4 \cdot 10^{-3}$, the mean nucleator concentration is $8.2 \cdot 10^3$.

state. This state is given by $s^0 = \nu v_a / \nu_d$, $T^0 = s^0 v_a / \nu_d$, and $n_f^{(0)} = \omega_d \rho_1^{(0)} n_b^{(0)} / (\omega_a (1 + \omega_1 n_b^{(0)2}))$, where the constant value of $n_b^{(0)}$ is a free parameter that fixes the amount of nucleators in the system. In the following, we will assume periodic boundary conditions.

In Figure 36, we present the stability of the homogeneous isotropic stationary state as a function of the dimensionless diffusion constant $\bar{D} = D/D_f$ of actin filaments and the dimensionless cooperativity parameter $\bar{\omega}_1 = \omega_1 \nu_d^5 / (v_a^2 \nu^2 \omega_d^2 D_f)$, where for convenience the bars are omitted in the following. For sufficiently small values of ω_1 , the homogeneous isotropic state is stable, but it turns unstable when the cooperativity exceeds a critical value. Remarkably, there is reentrant behavior: for sufficiently large values of ω_1 it is again stable. Note, that we did not find instabilities when assuming a linear dependence of the nucleator binding rate on bound nucleators instead of a quadratic dependence as in Eqs. (6.2) and (6.3). For both marginal lines there is a critical value of D below which the bifurcation is oscillatory, while it is stationary for larger values.

Figure 37 presents an example of an oscillatory solution (see supplementary movie M6.1.1). At time $t = 0$, the free nucleator concentration was chosen homogeneous and the profile of the bound nucleator concentration

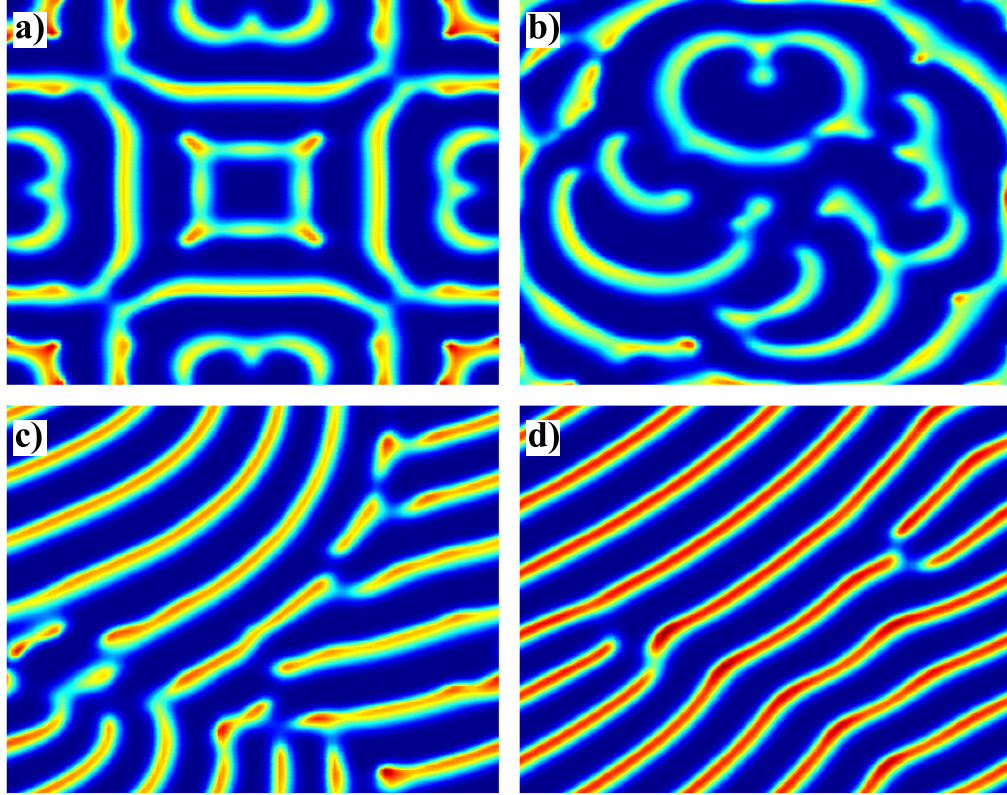


Figure 37: Traveling wave in a system of treadmilling filaments in presence of nucleators that undergo cooperative binding to substrate. Parameters are $D_b = 0.045$, $D = 0$, $\omega_1 = 3.5 \cdot 10^{-6}$, $\omega_a = 0.017$, $\omega_d = 0.021$, $v_a = 0.22$. The domain is square with side length 13.4. Snapshots correspond to times $t = 120$ (a), $t = 240$ (b), $t = 360$ (c) and $t = 480$ (d). The wave fronts in (d) propagate in the direction of the left lower corner.

was taken to be a small rotationally-invariant gaussian peak. Initially, no filaments are present in the system. The dynamics starts with a long-lived standing wave transient that break symmetry and turns into an array of traveling fronts. Transition from standing to traveling wave is associated with transient emergence of a spiral wave pattern.

6.2 Coarse-grained description

Since Equation (6.1) did not involve products of functions of ℓ or \mathbf{r} , it could be treated exactly. However, in general this is not the case. For example, if polymerization rate v_a in Eq. 6.1 would itself depend on the nucleator concentration, exact treatment would not have been possible and one would have to resort to considering the corresponding coarse-grained equations. Also, coarse-grained equations are much easier to integrate numerically. In this section we will analyze the corresponding coarse-grained description in order to check the validity of the coarse-graining approximation. As in Sec. 5.3, we introduce a hierarchy of order parameters. For convenience, we will describe filament distribution by coarse-grained density of filament mass centers rather than of plus-ends. After coarse-graining one arrives at:

$$\begin{aligned} \partial_t \rho_i &= D \Delta \rho_i - \frac{1}{2}(v_a + v_d) \nabla \cdot \mathbf{p}_i \\ &\quad + (v_a - v_d)(\delta_{i0} n_b + i \rho_{i-1}) - \nu_d \rho_i \end{aligned} \quad (6.6)$$

$$\begin{aligned} \partial_t \mathbf{p}_i &= D \Delta \mathbf{p}_i - \frac{1}{4}(v_a + v_d) \nabla \rho_i \\ &\quad + i(v_a - v_d) \mathbf{p}_{i-1} - \nu_d \mathbf{p}_i \end{aligned} \quad (6.7)$$

with

$$\rho_i(\mathbf{r}, t) = \int_0^\infty d\ell \ell^i \int d\hat{\mathbf{u}} c(\mathbf{r}, \hat{\mathbf{u}}, \ell, t) \quad (6.8)$$

$$\mathbf{p}_i(\mathbf{r}, t) = \int_0^\infty d\ell \ell^i \int d\hat{\mathbf{u}} \hat{\mathbf{u}} c(\mathbf{r}, \hat{\mathbf{u}}, \ell, t) \quad , \quad (6.9)$$

for $i = 0, 1, 2, \dots$. After coarse-graining, the overlap integral T_{tot} , Eq. (6.4), turns into

$$T_{tot} = \rho_1 + \frac{1}{48} \Delta \rho_3 + \dots \quad (6.10)$$

The stability diagram for the coarse-grained equation is presented in Fig. 38. The stability boundaries, obtained from the coarse-grained equations, are almost identical to those of the full description. Thus, the coarse graining approximation works well in the present parameter range.

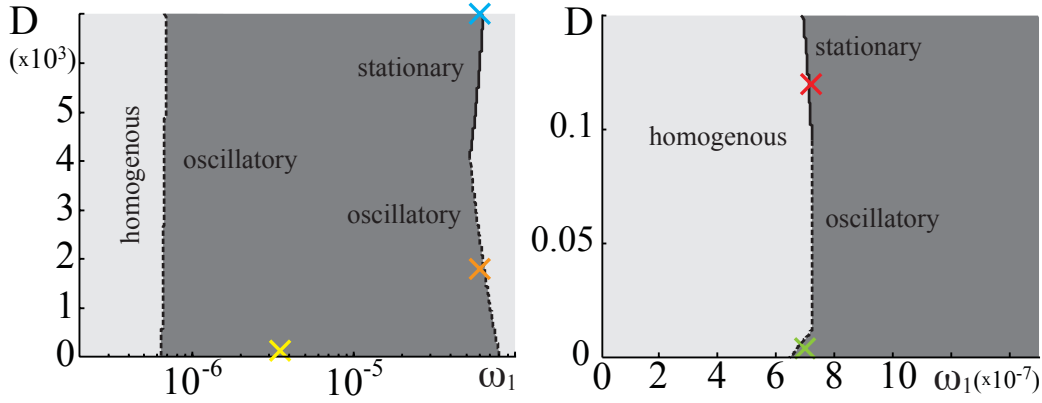


Figure 38: Stability diagram of the homogeneous isotropic stationary state. Regions of stability are indicated in light gray, regions of instability in dark gray. Dashed lines mark oscillatory instabilities, full lines stationary instabilities. The right panel is a magnification of the lower left corner of the left panel. The cyan cross indicates parameter values used for calculating the state in Fig. 39a, the green cross for Fig. 39b and the yellow for Fig. 39d. States corresponding to the red and orange crosses are discussed in the text. Parameters are as in Fig. 36.

Integrating the coarse-grained equations numerically, we find that the stationary states consist of a regular lattice of "asters" with minima in the filament density that are associated with a singularity in the polarization field, see Fig. 39a. The different asters are linked by regions of high filament density with the polarization vector pointing along the connection between two maxima in the filament density.

Let us now turn to the oscillatory solutions, which, in a system with periodic boundary conditions, are traveling waves. For large mean nucleator densities, these waves are essentially planar, see Fig. 39d. There is a zone of nucleators at the leading edge of a front, and a zone of filaments at the trailing edge. With decreasing amounts of nucleators in the system, the wave fronts become unstable and they break up into a number of isolated moving spots (see supplementary movie M6.2.1). In Figure 39b, we present a state for low values of the total nucleator amount. The system then evolves into an irregular arrangement of spots moving with different velocities. The polarization field associated with a spot has a singularity that lags behind the maxima of the filament and the nucleator densities in the direction of

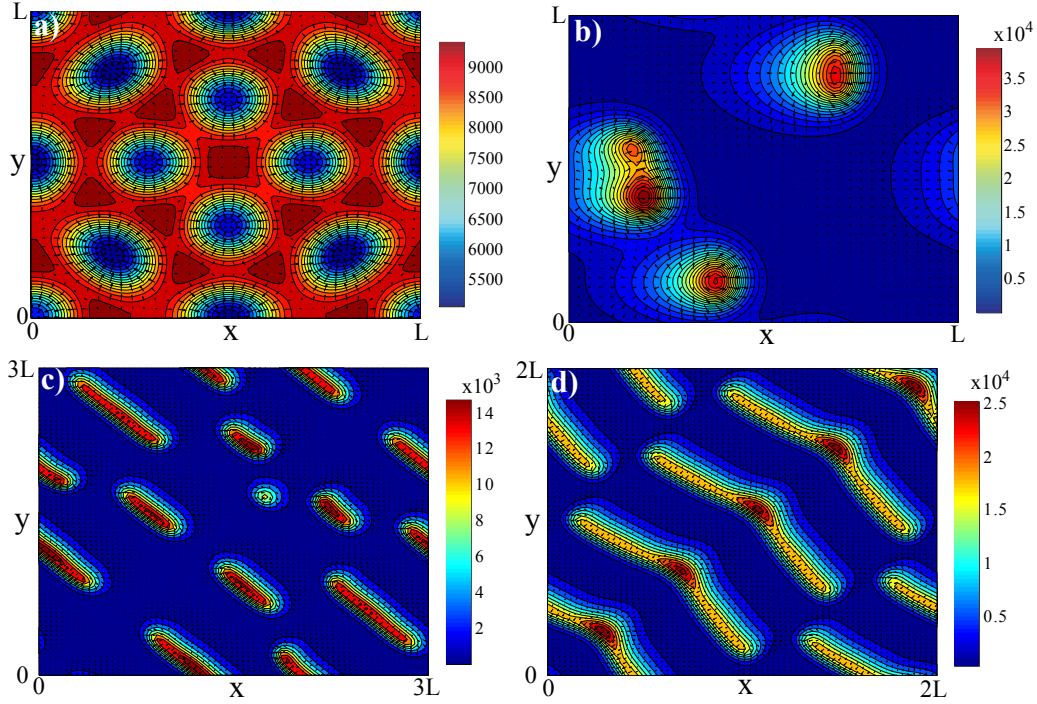


Figure 39: Examples of asymptotic solutions to the dynamic equations for periodic boundary conditions. Red indicates high, blue low values of ρ_0 . The black arrows indicate the polarization \mathbf{p}_0 . **(a)** Stationary state for $D = 0.007$ and $\omega_1 = 6 \cdot 10^{-5}$. The structure has a square symmetry. **(b)** Traveling spots for $D = 0.004$ and $\omega_1 = 7 \cdot 10^{-7}$. All spots move to the right with different velocities. They fuse if getting too close as can be seen in the center structure. **(c)**, **(d)** Broken up planar waves for increasing amounts of Hem-1 for $D = 10^{-4}$, $\omega_1 = 3.5 \cdot 10^{-6}$, and $n^{(0)} = 3.5 \cdot 10^3$ (c) and $n^{(0)} = 7.3 \cdot 10^3$ (d). The direction of motion is from the upper-right to the lower-left corner. In all cases $L = 1.63$.

movement. The nucleator density of such a spot has a similar form as the filament density but is shifted into the direction of motion with respect to the latter.

The overall structure is thus similar to the moving spot solutions for treadmilling filaments in the presence of nucleators that are transported by molecular motors even though there is no active directional transport of nucleators. For higher amounts of nucleators, the spots start to arrange into

a more regular pattern, see Fig. 39c and d, and finally turn into plane waves. When two wave fronts move towards each other, they annihilate each other upon collision. This is a consequence of the zone of filaments forming at the trailing edge of a wave front. Due to the terms proportional to ω_d in Eqs. (6.2) and (6.3), this zone is essentially void of nucleators such that the colliding fronts mutually inhibit further advancement, see Fig. 40.

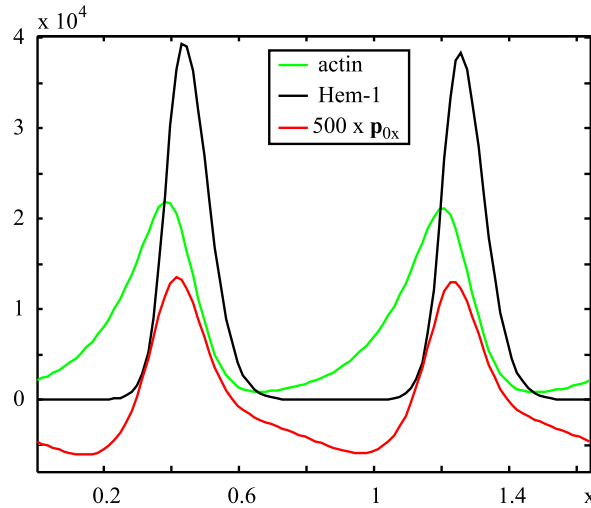


Figure 40: Traveling wave in a system of treadmilling filaments in presence of cooperatively binding nucleators. All fields are constrained to vary in the x -direction alone, yielding a one-dimensional description. The wave propagates in the positive x -direction. Peaks of actin (green) lag behind the peaks of nucleators (black). At the wave rear, actin expels nucleators into the cytosol, at the front nucleators re-bind to the membrane. Thus, the wave advances by recycling nucleators from the rear to the front. Parameters are: $D = 1 \cdot 10^{-3}$, $D_b = 1 \cdot 10^{-2}$, $\omega_a = 0.17$, $\omega_1 = 0.36 \cdot 10^{-5}$, domain length is 1.64, total amount of nucleators is $1.2 \cdot 10^4$.

We have investigated the asymptotic solutions also for other parameter values. In addition to the states discussed so far, the system can self-organize into a standing wave for parameters corresponding to the orange cross in Fig. 38. For the red cross we find an aster where the nucleator and the filament densities are radially symmetric and decrease from a common center. The polarization field has a singularity at the center and points radially outwards.

Careful inspection of the system's dynamics in the oscillatory part of the phase diagram reveals that prior to the formation of planar waves, transient spiral waves can be observed. These are similar to transient Hem-1 spiral waves observed in human neutrophils, see Ref. [91], movie S12.

Eventually, however, in our calculations, spirals do not persist. They seize, because due to the periodic boundary conditions, the rotating spiral starts to interact with itself. To further investigate the possible existence of persistent spiral waves, we considered the dynamics of the system in a confined domain.

6.3 Filaments in a confined domain

Consider a region in space that is limited by a boundary S . In order to confine the filament density c and the nucleator densities n_f and n_b to this region, one could supplement the dynamic equations (6.1)-(6.4) by reflecting boundary conditions along S . In that case, the component of any currents normal to S vanishes. These boundary conditions, however, do not translate into boundary conditions for the fields ρ_i and \mathbf{p}_i in the coarse grained description, see Eqs. (6.8) and (6.9). The reason for this is that close to a reflecting boundary, the filament and nucleator densities will necessarily vary on small length scales. Consequently, they are not well described by the lowest orders in the hierarchy of order parameters ρ_i and \mathbf{p}_i . In Sec. 5.5 we dealt with this problem by restricting the expansion of the nucleator flux to the first order derivatives. More generally, however, this approach is inapplicable. In particular, in systems with interacting particles, omitting the higher order corrections to the coarse-grained flux results in equations whose fields do not remain bounded at all times for bounded initial conditions, and can therefore not serve an approximation of the full non-local description [96].

Thus, we shall account for the presence of the boundary in terms of a potential V , which is essentially a phase field approach similar to the one used previously in a description of the growth of stereocilia [65]. Through the potential, the dynamics of the filaments is influenced in two ways: first of all, the polymerization velocity v_a is reduced by a factor $\exp\{-\hat{\mathbf{u}}\nabla V/f_0\}$, where f_0 is a characteristic force [16]. Secondly, the filaments experience a force $-\nabla V$. At a distance d from the boundary, the potential V has the value

$$V(d) = \alpha \left[\frac{1}{2} + \frac{1}{2} \tanh(\beta d) \right] . \quad (6.11)$$

In this expression, α determines the maximum value of the potential, while β determines the steepness in the potential rise. The value of β^{-1} should be of the order of the mean filament length to allow for meaningful coarse graining. Other functional forms of the potential, in particular, unbounded functions, can be chosen. The potential (6.11), though, turns out to be convenient for numerical analysis.

As, eventually, we will coarse grain the fields, the exact part at which the force is applied to a filament does not matter. Thus we evaluate the force on a filament by calculating the derivative of V at the position of filament center \mathbf{r} . The force field resulting from the potential at a point \mathbf{r} is given by $-\nabla V(d)$, where d is given by $d = \min_{\mathbf{r}_b \in S} |\mathbf{r} - \mathbf{r}_b|$. From this force field, we obtain additional terms on the right hand sides of the coarse grained dynamic equations (6.6) and (6.7), that read $\nabla(\eta\rho_i\nabla V)$ and $\nabla(\eta\mathbf{p}_i\nabla V)$, respectively. Here, η is the mobility of the filaments, which we assume to be independent of the filament length. For simplicity, we will neglect in the following the dependence of v_a on the potential. This is appropriate as long as the forces resulting from interactions with the domain boundary, i.e., ∇V , are small compared to the characteristic force f_0 .

We now present the dynamics of the actin-nucleator system in a circular domain. For the same parameter values as in Fig. 39b, the solution is presented in Fig. 41 (see supplementary movie M6.3.1). In the asymptotic state the circular symmetry of the system is spontaneously broken. It consists of a pair of counter rotating spirals in the vicinity of the boundary. From this spiral pair, wave fronts emanate that move towards the opposite boundary, where they vanish. The traveling waves are similar to the wave fronts of Fig. 39d.

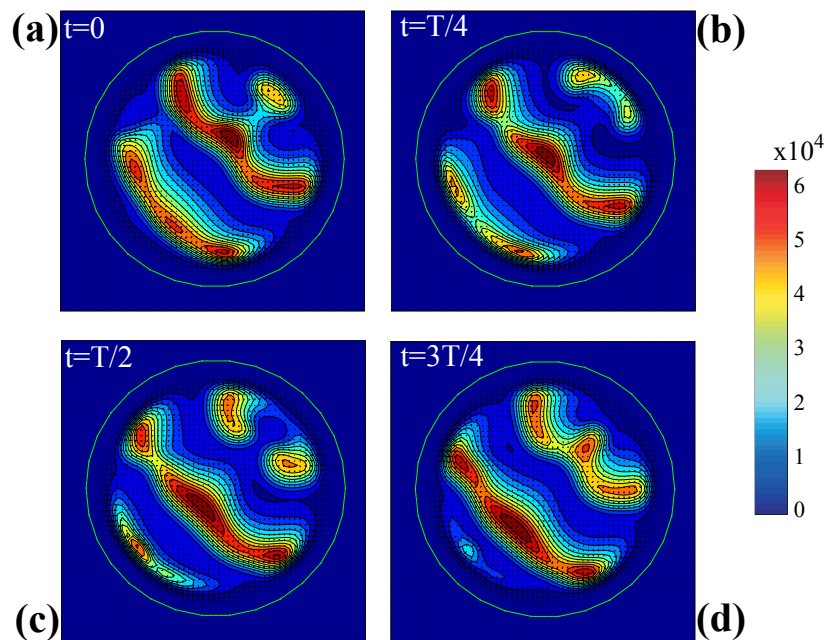


Figure 41: Subsequent snapshots of Hem-dynamics in a circular domain. The domain boundary is indicated by the green line. A pair of counter-rotating spirals forms that send out traveling waves which vanish at the opposing end. Red indicates high, blue low values of ρ_0 . The black arrows indicate the polarization \mathbf{p}_0 . The four snapshots correspond to times $t = 0$ (a), $t = T/4$ (b), $t = T/2$ (c), and $t = 3T/4$ (d), where $T = 4.2$ is the period of the state that is periodic in time. Parameters are as in Fig. 39d, the radius of the domain is $r = 0.6$.

6.4 Membranous boundary

The previous section introduced a description of treadmilling filaments, nucleated by molecules that underwent cooperative binding to the substrate. We have shown that such a system could self-organize into traveling waves, reproducing the phenomena, observed in experiments on human neutrophils. Importantly, experiments in Ref. [91] suggest that actin wave dynamics in neutrophils serve a vital biological purpose, determining the cell shape and generating leading edge protrusion, thereby enabling cell locomotion. In general, cell crawling as well as generation of many vital cellular organelles such as e.g. filopodia and stereocilia relies on interactions of the cytoskeleton with the cell membrane. Devising a physical description of such phenomena requires introducing a moving boundary, representing the cell membrane. This is the subject of the present section.

We shall develop a description of membrane vesicle, propelled by treadmilling filaments, by combining equations, introduced in the previous section, with moving boundary conditions. Clearly, treadmilling filaments can not propel the vesicle unless they make contact with the substrate as momentum conservation would be violated otherwise. Thus, we suppose that filaments in the interior of the vesicle are anchored to the substrate via adhesion complexes, see Fig. 42. Assuming that bonds between the adhesion molecules and the filaments have finite life time, on sufficiently large time-scale, interactions of filaments with adhesion complexes can be described as effective friction with the substrate beneath the membrane, see [78].

We assume that the domain boundary is a fluid membrane. Deriving equations of motion for vesicle surface requires specifying the forces on the membrane. These will have the following contributions. Deformation forces due to finite bending rigidity of the membrane can be derived from the Helfrich free energy $\int \kappa/2H^2 dS$, where H is the mean curvature and κ an effective bending modulus[72, 73]. The forces associated with finite surface tension and finite external pressure follow from the corresponding membrane energy contribution, reading $\tau S + PV$, where τ is surface tension, S is the surface area of the vesicle, V is vesicle volume and P is external pressure. Finally, the filaments exert forces on the membrane. These forces are equal any opposite to the force exerted by the membrane on the filaments. Hence total energy, associated with the membrane, is

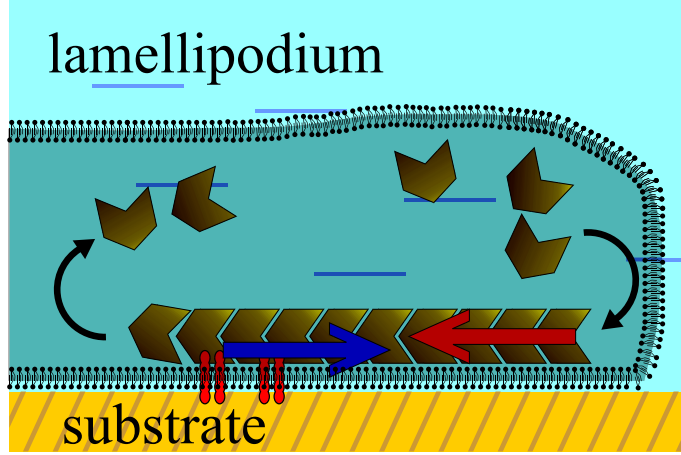


Figure 42: Schematic illustration of forces acting on a filaments that is interacting with the boundary. The red arrow indicates the force from the boundary due to polymerization at the barbed end facing the boundary surface. The blue arrow indicates adhesion forces with the substrate, described as effective friction, see text.

$$\mathcal{F} = \int_{\partial\Omega} \kappa H^2/2 + \tau S + PV + \int d\mathbf{r} \rho_0(\mathbf{r}) V(\mathbf{r}) \quad . \quad (6.12)$$

Henceforth we shall be assuming that fictitious force $-\nabla V$ on a filament from the boundary is applied at the plus-end rather than at the center of mass. Hence $\rho_0(\mathbf{r})$ in Eq. (6.12) is the density of filament tips rather than that of mass centers.

Finally, we assume that the vesicle is very flat meaning that its shape is fully determined by a one-dimensional curve Γ that traces out the vesicle rim. Thus, in (6.12) S will denote the length of the vesicle rim, V shall be vesicle surface (contact area with the substrate), H^2 denotes square curvature of the rim. The force density at the boundary is determined by functional derivative of the total free energy with respect to the boundary $\delta\mathcal{F}/\delta\Gamma$. Importantly, this will automatically satisfy the force balance, i.e. total force on the filaments from the boundary is equal to the total force on the boundary from the filament tips (see Appendix D). We shall suppose that a point at the vesicle edge moves with the speed $\mathbf{v} = (1/\zeta)\delta\mathcal{F}/\delta\Gamma$ where $1/\zeta$ is ef-

fective edge mobility. This expression amounts to neglecting hydrodynamic interactions between different surface elements of the boundary.

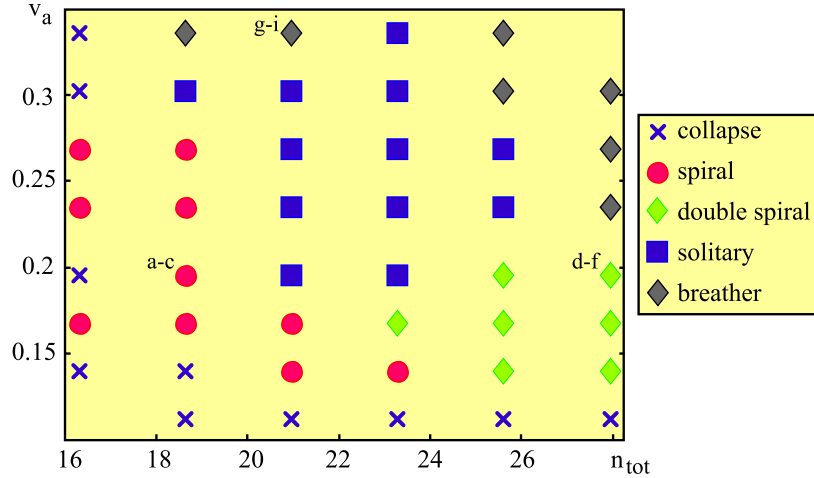


Figure 43: Phase diagram for equations, describing treadmilling filaments, in presence of nucleators that bind the substrate cooperatively. Red circles indicate spiral solutions. Green diamonds correspond to double spirals. Blue squares are solitary moving vesicles. Gray diamonds are "breathers", i.e. solutions that exhibit periodic vesicle expansion-contraction with mass center remaining approximately stationary. Blue crosses correspond to "vesicle collapse", when inner pressure due to filament treadmilling is small so that the vesicle contracts into a small spot that remains stationary. Lower-case letters next to three labels indicate parameter values that correspond to simulation in Fig. 44. Parameters are: $\omega_a = 8.5 \cdot 10^{-3}$, $\omega_1 = 64.5$, $D = 0$, filament mobility $\eta = 0$, $P/\zeta = 0.1$, $\sigma/\zeta = 3.35 \cdot 10^{-3}$, $\kappa/\zeta = 1.34 \cdot 10^{-5}$.

The different dynamical states, exhibited by the system with moving boundaries are summarized in phase diagram, presented in Fig. 43 and illustrated in detail in Fig. 43. Note that in these simulations the volume of the vesicle is unconstrained and is determined by e.g. the total amount of nucleators. If vesicle size is small, nucleators concentrate, resulting in dynamical instability, generating traveling waves that expand the vesicle upon encountering the membrane. Vesicle expansion causes effective dilution of nucleators, abolishing wave dynamics. Stationary vesicle size is selected when inhibition of wave-dynamics due to effective dilution precisely counterbal-

ances the expansion.

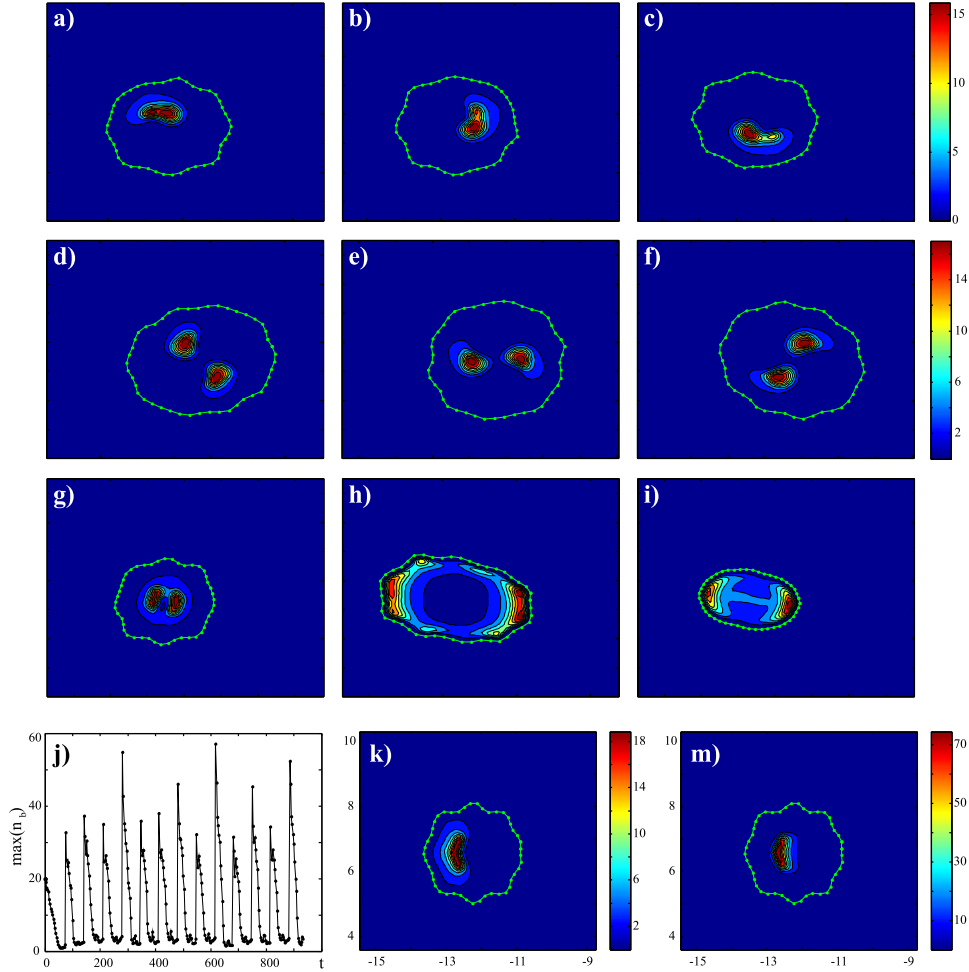


Figure 44: The different dynamic states in the system of treadmilling filaments nucleated by proteins that undergo cooperative binding to the substrate with moving boundary. **(a)-(c)** Spiral. **(d)-(f)** Double spiral. **(g)-(i)** "Breather": the vesicle undergoes periodic contractions and expansions. **(j)** Maximal value of bound nucleator density in the "breather" state **(g)-(i)**, showing persistent periodic oscillations. **(k)** Density of bound nucleators in a solitary moving vesicle. **(m)** Total filament density corresponding to **(k)**. Parameters are as in Fig. 43.

If the total amount of nucleators as well as the filament treadmilling speed are very low, the interior pressure due to filaments, treadmilling against the surface of the vesicle, cannot withstand constant outer pressure P causing the vesicle to collapse. As this would usually result in numerical instability in our simulations, we do not discuss the asymptotic state in the corresponding parameter range. Increasing either nucleator amount or treadmilling speed spirals are obtained (see supplementary movie M6.4.1). In this case inner pressure due to filament treadmilling suffices to prevent vesicle collapse, but does not suffice to sustain persistent unidirectional motion. For larger nucleator amounts and not too high treadmilling speeds spirals turn into double spirals (see Fig. 44 and supplementary movie M6.4.2). Increasing treadmilling speed, solitary moving states bifurcate out of double spirals, see supplementary movie M6.4.3. Finally, low nucleator amounts and large treadmilling speed leads to states that we called "breathers". These are characterized by persistent oscillations of vesicle size with rather uniform expansion followed by contraction (see Fig. 44 and supplementary movie M6.4.4).

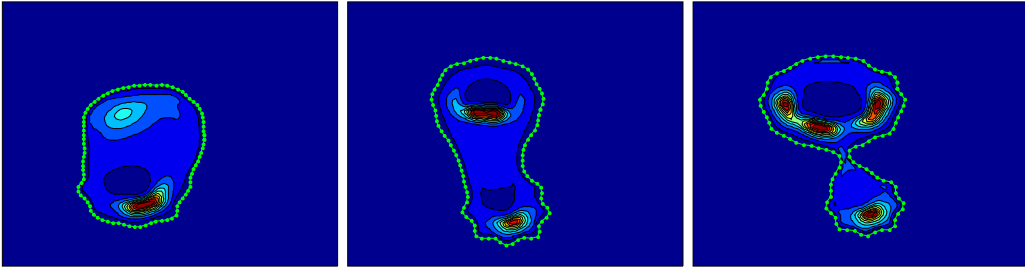


Figure 45: Fragmentation of a vesicle. Parameters are: $\omega_a = 0.017$, $\omega_1 = 64.5$, $v_a = 0.335$, $D = 0$, filament mobility $\eta = 0$, $P = 0.1$, $\sigma = 3.35 \cdot 10^{-3}$, $\kappa = 1.34 \cdot 10^{-5}$, total nucleator amount $n_{tot} = 48.5$, domain is square with side length 13.4.

We examined behavior of the system for total nucleator amounts that are much larger than those, used in simulations, presented in Fig. 44. Two possible regimes could be identified. Either the vesicle fragmented into small pieces, each setting out in solitary motion in a random direction, or the vesicle remained intact, exhibiting oscillatory dynamics with a spiral defect at its center. Thus, our simulation suggest that the vesicle size does not simply increase with increasing total nucleator amount: at some point too large a

vesicle fragments into smaller pieces, see Fig. 45 and supplementary movie M6.4.5.

7 Conclusions and outlook

In this thesis, we introduced a general framework for describing the dynamics of treadmilling filaments where the rates of filament nucleation, polymerization, and depolymerization can be regulated by other molecules. Treadmilling is a central feature of the cytoskeletal dynamics and plays a key role in various cell processes including generation of various cellular appendages (e.g. stereocilia and filopodia), microtubule structures in melanophores as well as virtually all forms of cell crawling. The results of our work indicate that self-organization of treadmilling filaments is an important aspect of cytoskeletal dynamics.

The framework is formulated in terms of mesoscopic equations, specifying the dynamics of filaments and regulatory proteins. Our description circumvents the weaknesses of the previously developed phenomenological approaches: parameters are few and they all have straight-forward interpretations in terms of molecular properties. In contrast to MD simulations, our descriptions generically admit exhaustive exploration of the phase space and are general. In particular, our equations can be compared to the phenomenological hydrodynamic descriptions of the cytoskeleton. An interesting subject of future research will be to explore in detail the connection between our mesoscopic and the previously developed hydrodynamic and microscopic descriptions.

Our mesoscopic equations, even numerically, can not be solved. In order to be able study dynamic equations, describing the time evolution of the filament density, we introduced a number of novel methods. In order to discuss their applicability, it is appropriate to distinguish between the following three equation types. (I) Equations, describing filament density dynamics, that are linear in the densities and with constant coefficients. (II) Equations, that are linear in the filament densities and with space- or/and length-dependent parameters. (III) Equations that are nonlinear in the filament densities. Note that the equations, describing the dynamics of the regulatory proteins that might influence the rates of filament nucleation, polymerization and depolymerization, may be arbitrary.

We have shown that in equations of type (I) we can integrate out the length dependence. Furthermore, they can be reformulated in quantities such that the equations become pure PDEs without any integrals.

Type (II) equations do not admit exact treatment, like type (I) equations do. In order to treat type (II) equations we rewrote them in terms of

moments of the filament length distribution and performed coarse-graining. This technique can be applied when the system exhibits scale separation, i.e., when the size of the pattern is much larger than mean filament length.

The two methods cannot be applied to treat type (III) equations. Generically, type (III) equations may be re-written in terms of moments of the filament length distribution, but equations for any one moment involves infinitely many other moments. Hence, a closed set of equation can, in general, not be obtained.

Motivated mainly by experiments on fish melanophores, we applied our framework to treadmilling filaments that are nucleated by molecules and are actively transported along filaments. We found that filaments self-organized into asters when active transport is directed towards the shrinking filament minus-end (as in melanophore), whereas they formed traveling waves when the nucleator transport is plus-end directed. The latter situation captures the essential part of the dynamics of nucleating proteins in keratocyte, where WASP protein that promotes actin filament nucleation, localizes to the cell's leading edge, where filament plus ends concentrate.

In the light of these results, it appears plausible that cytoskeletal rearrangements involved in e.g. cell motility are essentially rooted in self-organization of a few cytoskeletal constituents. For example, it is likely that cell locomotion arises due to intrinsic instability of the actin cortex, resulting in motion in a randomly chosen direction. In the course of any symmetry breaking, the system turns infinitely sensitive to perturbations that determine the symmetry of the bifurcating state. Thus, a chemotactic signaling pathway might serve to select the direction of the cell motion by influencing the course of an intrinsic spontaneous instability rather than being its cause *per se*.

Returning to the case of melanophores, our treatment reproduced the formation of stationary asters in the case of minus-end directed motor transport. Moreover, since aster solutions bifurcated from a long-wave instability, they exhibited coarsening, in agreement with experimental findings. We further examined the effects of the domain shape on the aster formation. It appeared that our simulations satisfactorily reproduced experimental observations. For instance, in simulations of a dumbbell-shaped domain one could observe formation of two separate asters that eventually merged at the "neck", joining the two larger fragment subportions much like was seen in experiments. Finally, we analyzed the merging of two asters, deriving an analytic approximation of the dependence of the inter-aster separation on time.

It would be interesting to check this prediction by quantitative experiments, measuring the distance between two interacting asters as a function of time.

Motivated by findings on the locomotion of human neutrophils, we then analyzed treadmilling filaments nucleated by molecules that undergo cooperative binding with the membrane. We demonstrated that a minimal degree of cooperativity is required in order to generate an instability of the homogeneous isotropic state. The corresponding equations are of type (I) and admit exact treatment. It thus served as a test case for the applicability of our approximations, employed for treating the type (II) equations. We showed that stability boundaries in the coarse-grained description coincided with exact ones. We further analyzed equations in the fully nonlinear regime, identifying a variety of patterns, including aster arrays, traveling and standing waves, as well as transient spirals.

Our work on mesoscopic mean-field descriptions of the cytoskeleton leaves two major open problems. Firstly, it is essential develop methods to treat type (III) equations. Secondly, it would be desirable to extend the treatment of type (II) equations to situations without scale-separation. Indeed, the lengths of the cytoskeletal filaments are in many cases comparable to the sizes of the cellular structures they constitute. Hence, their interactions are intrinsically non-local and should therefore not be described by local theories.

An important aspect of cytoskeletal dynamics is the interaction of treadmilling filaments with a membrane. In particular, a great variety of vital cellular processes, e.g. previously mentioned examples with the various cellular appendages as well as cell locomotion, rely on interactions of the cytoskeletal filaments with the boundary. In this case, the boundary effects may definitely not be disregarded. Incorporation of boundary conditions into a mesoscopic description is, however, not straightforward. We developed a method, allowing to account for the boundary conditions in a coarse-grained description. When performing coarse-graining one assumes that filament concentration varies on spatial scales that are much larger than the mean filament length. This assumption is not valid in the vicinity of the boundary, where concentration generically has a discontinuity. Hence, we argued that accounting for a reflecting boundary in a coarse-grained description is possible exclusively by replacing the boundary by a fictitious force that confines the filaments to the interior of the domain. As long as this force varies on a length-scale that is sufficiently larger than mean filament length but is well below the scale of the pattern, qualitative aspects of the dynamics cannot depend on the particular choice of the fictitious force and must therefore provide a good

approximation to the exact dynamics with a reflecting boundary.

We exploited this approach to combine our equations, describing actin wave-dynamics in neutrophils with a membraneous moving boundary, obtaining a description of a vesicle, deformed and propelled by treadmilling filaments in its interior. We found that the system self-organized into a variety of states, including spirals and persistently oscillating "breathers", whose center of mass remained approximately stationary, as well as into solitary moving states. Being mesoscopic, our description involves no parameters without a clear physical meaning. Furthermore, our approach suggests solutions to some long-standing problems, associated with cell locomotion.

It turned out that all of the motion modes in our vesicle description are seen in motile cells: spirals and "breathers" have been seen in *Dictyostelium discoideum* [6], whereas persistent unidirectional motion is typical of, e.g., keratocytes. Importantly, these states, all relying on the same processes, correspond to different choices of the parameters in the same description, rather than to different model variants.

Secondly, it is not known what determines the size of a cell. Experiments indicate that the exchange of water through the membrane by means of active pumps contributes to cell size regulation. However, cytoskeletal components cannot be pumped in or out of the cell. Microtubular structures are known to be implicated in the regulation of the cell size. Nevertheless, these can not determine the cell size *per se*, presumably regulating the cell volume by influencing the state of the actin cortex. In other words, the cell size is actually that of the cell cortex rather than that of the water volume in cell interior. Thus, understanding why cells are as large as they are, one needs to understand the mechanisms, regulating the cortex size. In all earlier descriptions of cell locomotion cell size was either constrained to remain constant (an unphysical assumption of incompressible cell), or relied on some heuristic rules that could not be interpreted in terms of some physical processes. Our description involves no assumptions of this kind. Instead, we hypothesize that the vesicle size might be determined by the competition of the expansion that tends to increase the volume with the resulting nucleator dilution, that inhibits edge protrusion

Our description suggests a possible unified approach to cell locomotion. Up to date, the different states, exhibited by motile cells, have conventionally been interpreted to correspond to the different variants of the cell's transduction pathways or to modifications of transduction pathway constituents. We propose to consider cell motility apparatus as a self-organized entity, and

to interpret the different locomotion modes as the different dynamical states of the corresponding dynamical system.

A Dynamic equations for the hierarchy of order parameters

In the following, we derive Eqs. (5.23)-(5.26) starting from Eqs. (5.4), (5.16), and (5.5) describing a system of filaments with varying lengths in the presence of nucleators. We start by introducing a hierarchy of densities defined as

$$\Lambda_i(\mathbf{r}, \hat{\mathbf{u}}, t) = \int_0^\infty d\ell \ell^i c(\mathbf{r}, \hat{\mathbf{u}}, \ell, t) \quad (\text{A.1})$$

For filaments of orientation $\hat{\mathbf{u}}$, $\Lambda_0(\mathbf{r}, \hat{\mathbf{u}})$ is the density of filaments, $\Lambda_1(\mathbf{r}, \hat{\mathbf{u}})/\Lambda_0(\mathbf{r}, \hat{\mathbf{u}})$ the average filament length, and $\Lambda_2(\mathbf{r}, \hat{\mathbf{u}})/\Lambda_0(\mathbf{r}, \hat{\mathbf{u}}) - (\Lambda_1(\mathbf{r}, \hat{\mathbf{u}})/\Lambda_0(\mathbf{r}, \hat{\mathbf{u}}))^2$ the variance of the filament length distribution at \mathbf{r} . Analogous interpretations can be given to Λ_i for $i > 2$. Multiplying Eq. (5.16) by ℓ^i and integrating with respect to ℓ from 0 to ∞ the dynamic equations for the densities Λ_i are obtained:

$$\begin{aligned} \partial_t \Lambda_i(\mathbf{r}, \hat{\mathbf{u}}) &= \int_0^\infty d\ell \ell^i D(\ell) \nabla^2 c(\mathbf{r}, \hat{\mathbf{u}}, \ell) - v_a \nabla \cdot \hat{\mathbf{u}} \Lambda_i(\mathbf{r}, \hat{\mathbf{u}}) \\ &+ i(v_a - v_d) \Lambda_{i-1}(\mathbf{r}, \hat{\mathbf{u}}) - (v_a - v_d) \delta_{i0} n(\mathbf{r}) - \nu_d \Lambda_i(\mathbf{r}, \hat{\mathbf{u}}) \quad . \end{aligned} \quad (\text{A.2})$$

Here, we have used that $c(\mathbf{r}, \hat{\mathbf{u}}, \ell) \rightarrow 0$ for $\ell \rightarrow \infty$. The integral in the first term can in general not be expressed in terms of the densities Λ_i . To this end a Taylor expansion of $D(\ell)$ can be used. In this case, the time evolution of all Λ_i couple to each other. However, $D(\ell)$ denotes an effective diffusion constant. Its value is dominated by active processes rather than thermal diffusion, as active contributions – at least for sufficiently long filaments – dominate. Therefore, we assume $D(\ell) = \text{const.}$ in the following. Then, the term can be written as $D \nabla^2 \Lambda_i(\mathbf{r}, \hat{\mathbf{u}})$. The equations now close in the moments, that is, the time evolution of Λ_i only depends on Λ_j with $j \leq i$.

In the next step, we perform a moment expansion with respect to the orientation and express Λ_i through the quantities ρ_i and \mathbf{p}_i defined in Eqs. (6.8) and (6.9). Explicitly, we write

$$\Lambda_i = \frac{1}{2\pi} \{ \rho_i + 2\hat{\mathbf{u}} \cdot \mathbf{p}_i \} \quad . \quad (\text{A.3})$$

If needed, higher moments can be included. Multiplying Eq. (A.2) by $\hat{\mathbf{u}}^k$ and integrating with respect to $\hat{\mathbf{u}}$, the dynamic equations (6.6) and (6.7) are obtained.

Finally, the current \mathbf{j}_{act} , Eq. (5.5), has to be expressed in terms of the fields ρ_i and \mathbf{p}_i . To this end, we first coarse grain by Taylor expanding c with respect to ξ in the integral. Then the integrals in Eq. (5.5) can be performed eventually resulting in expressions (5.25) and (5.26).

B Aster solution in the limit of zero nucleator diffusion

Assuming that the polarization is always radially oriented, $\mathbf{p}_i = p_i \hat{\mathbf{e}}_{\mathbf{r}}$, where $\hat{\mathbf{e}}_{\mathbf{r}}$ is the radial normal vector, the stationary equations for the densities ρ_i and the polarization fields p_i read in polar coordinates

$$\begin{aligned} \left(\frac{1}{r}\partial_r + \partial_r^2\right)\rho_i - \bar{v}_a \left(\frac{1}{r} + \partial_r\right)p_i + i(\bar{v}_a - \bar{v}_d)\rho_{i-1} - \bar{v}\delta_{i0}(\bar{v}_a - \bar{v}_d)n - \rho_i &= 0 \\ \left(\frac{1}{r}\partial_r + \partial_r^2 - \frac{1}{r^2}\right)p_i - \frac{\bar{v}_a}{2}\partial_r\rho_i + i(\bar{v}_a - \bar{v}_d)p_{i-1} - p_i &= 0 \end{aligned} \tag{B.1}$$

In the limit of small nucleator diffusion D_n , pigments aggregate in a two-dimensional delta-source at the origin, i.e. $n = n_0\delta^2$. Applying the Fourier-Bessel transform $\rho_i(r) = \int \tilde{\rho}_i(\omega)J_0(\omega r)\omega d\omega$, $p_i(r) = \int \tilde{p}_i(\omega)J_1(\omega r)\omega d\omega$ and using $\tilde{\delta}^2 = 1/2\pi$ we obtain

$$\begin{aligned} -\omega^2\tilde{\rho}_i - \bar{v}_a\omega\tilde{p}_i + i(\bar{v}_a - \bar{v}_d)\tilde{\rho}_{i-1} - \tilde{\rho}_i &= \bar{v}(\bar{v}_a - \bar{v}_d)n_0\delta_{i0}/2\pi \\ -\omega^2\tilde{p}_i + \frac{\bar{v}_a}{2}\omega\tilde{\rho}_i + i(\bar{v}_a - \bar{v}_d)\tilde{p}_i - \tilde{p}_i &= 0 \end{aligned} \tag{B.2}$$

Solving for $\tilde{\rho}_i$ and \tilde{p}_i and taking inverse transform one arrives at explicit expressions for moments of aster-solution

$$\begin{aligned}
\rho_0 &= \int_0^\infty d\omega \frac{J_0(\omega r) \omega (\omega^2 + 1) (\bar{v}_a - \bar{v}_d) n_0}{(2\omega^4 + 4\omega^2 + \bar{v}_a^2 \omega^2 + 2)\pi} \\
p_0 &= \int_0^\infty d\omega \frac{1}{2} \frac{J_1(\omega r) \bar{v}_a \omega^2 (\bar{v}_a - \bar{v}_d) n_0}{(2\omega^4 + 4\omega^2 + \bar{v}_a^2 \omega^2 + 2)\pi}
\end{aligned} \tag{B.3}$$

The integrands in the expressions for higher moments contain rather lengthy rational functions of ω and are, therefore, omitted. Any number of asters can be superimposed due to the linearity of equations in the present limit. Any one aster moves with the speed \mathbf{j}_{act}/n where \mathbf{j} is active nucleator current given by Eq. 5.25, and is determined by the filament density distribution due to surrounding asters.

C Boundary conditions for describing melanophore fragments

In the following we discuss the boundary conditions in a system of treadmilling filaments with actively transported nucleators. One boundary condition is obtained by requiring that the nucleator flux at the boundary is zero. Since the active part of the nucleator flux (5.25) contains the γ -term which involves derivatives of order higher than one, one boundary condition does not suffice to determine nucleator dynamics. However, as we have checked in simulations with periodic boundaries, the γ -term is negligible, provided that the mean filament length is significantly smaller than the characteristic size of the simulated pattern. Restricting the current to the two leading terms in (5.25), the boundary condition for nucleator density field is $-D\nabla n - v_n (\frac{1}{2}\mathbf{p}_2 + \frac{1}{6}\nabla\rho_3) = 0$. Finally, we assume that filaments facing the boundary with their plus-end can not polymerize. A filament that points with its plus-end out of the boundary and has its minus-end at the boundary is of length zero and must depolymerize in the next time instance. Hence, the boundary acts a sink of the filament and polarization density of strengths $v_d \int_{\hat{\mathbf{u}} \cdot \hat{\mathbf{n}} > 0} d\hat{\mathbf{u}} c \approx v_d(\rho/2 + 2\hat{\mathbf{n}} \cdot \mathbf{p}/\pi)$ and $v_d \int_{\hat{\mathbf{u}} \cdot \hat{\mathbf{n}} > 0} d\hat{\mathbf{u}} \hat{\mathbf{u}} c \approx v_d(\rho\hat{\mathbf{n}}/\pi + \mathbf{p}/2)$, respectively, where $\hat{\mathbf{n}}$ is the normal to the boundary, with $|\hat{\mathbf{n}}|^2 = 1$. Multiplying these expressions by ℓ^i and integrating over ℓ yields fluxes of moments ρ_i 's and \mathbf{p}_i 's.

D Force balance at a (moving) coarse grained boundary

As we shall see in this section, the procedure of coarse-graining the boundary, outlined in Sec. 6.3, suggests a natural way of deriving force density at the boundary due to filaments, treadmilling against its surface. According to assumptions of the previous section total energy of the system due to interactions of filaments with external fictitious force $-\nabla V$ is $\mathcal{F} = \int d\mathbf{r} V(\mathbf{r}) \rho_0(\mathbf{r})$. Let us parameterize the boundary of domain Ω by a hypersurface $\Gamma(\mathbf{s})$ where $\mathbf{s} = [s_1, s_2]$ in the case of three-dimensional domain Ω and $\mathbf{s} = s$ if Ω is two-dimensional. Taking variation of the potential with respect to the surface,

$$\mathbf{f}(\mathbf{s}) = -\frac{\delta\mathcal{F}}{\delta\Gamma} \quad (\text{D.1})$$

gives the force at the boundary. Importantly, this is guaranteed to respect force balance, i.e.:

$$\int d\mathbf{r} \rho_0(\mathbf{r}) \nabla V(\mathbf{r}) = - \int_{\partial\Omega} dS \frac{\delta\mathcal{F}}{\delta\Gamma} \quad (\text{D.2})$$

In order to see this it is most convenient to consider the case when the curve parameterizing domain boundary is discretized (as is most relevant for numerical implementation). Thus, we assume that the boundary of domain Ω , confining the filaments, is piecewise linear, i.e. it is a polygon with vertices $\{\mathbf{s}_i\}$ (henceforth the braces shall indicate sets).

With every vertex \mathbf{s}_i we associate a portion of domain boundary consisting of two line segments joining \mathbf{s}_i with mid-points of its two adjacent edges (see figure 46). The length of boundary portion, corresponding to vertex \mathbf{s}_i given by $\|\mathbf{s}_i/2 - \mathbf{s}_{i+1}/2\| + \|\mathbf{s}_i/2 - \mathbf{s}_{i-1}/2\|$ will be denoted s_i . Total energy associated with potential V is:

$$\mathcal{F} = \int_{\Omega} d\mathbf{r} V(\mathbf{r}; \{\mathbf{s}_i\}) \rho_0(\mathbf{r}) \quad (\text{D.3})$$

Note that now potential $V = H[d(\mathbf{r}; \{\mathbf{s}_i\})]$ depends implicitly on $\{\mathbf{s}_i\}$ (the distance from point \mathbf{r} to domain boundary $\partial\Omega$ is determined by parameterization of the boundary). Discrete variant of (D.1) reads

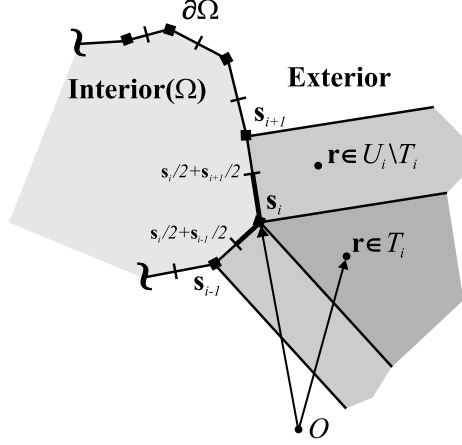


Figure 46: Schematic sketch of a two-dimensional domain parameterization by a piecewise linear curve. $\{\mathbf{s}_i\}$ are vertices of domain interior (polygon Ω). Shaded regions illustrate sets, referred to in the text.

$$\mathbf{f}_i = -\frac{1}{s_i} \partial_{\mathbf{s}_i} \mathcal{F}(\{\mathbf{s}_i\}) \quad (\text{D.4})$$

We shall show that (D.4) implies force balance, i.e. total force on the boundary from filament tips equals total force on the filaments from the boundary, formally

$$\sum_i s_i \mathbf{f}_i = - \int d\mathbf{r} \nabla V(\mathbf{r}) \rho_0(\mathbf{r}) \quad (\text{D.5})$$

Let $U_i[\{\mathbf{s}_j\}]$ denote the set of points \mathbf{r} whose closest point of boundary manifold $\partial\Omega$ (parameterized by positions of vertexes $\{\mathbf{s}_j\}$) is either \mathbf{s}_i or some point on one of the boundary edges adjacent to \mathbf{s}_i . According to (D.4), x -component of $s_i \mathbf{f}_i$ is

$$\lim_{ds \rightarrow 0} \frac{\int d\mathbf{r} \rho_0(\mathbf{r}) H[d(\mathbf{r}; \{\mathbf{s}'_j\})] - \int d\mathbf{r} \rho_0(\mathbf{r}) H[d(\mathbf{r}; \{\mathbf{s}_j\})]}{ds} \quad (\text{D.6})$$

where $\mathbf{s}'_j = \mathbf{s}_j + [ds, 0]$ if $j = i$ and $\mathbf{s}'_j = \mathbf{s}_j$ otherwise. Denote $U_i[\{\mathbf{s}'_i\}]$ by U'_i , $\rho_0(\mathbf{r}) H[d(\mathbf{r}; \{\mathbf{s}_i\})]$ by Φ and $\rho_0(\mathbf{r}) H[d(\mathbf{r}; \{\mathbf{s}'_i\})]$ by Φ' . We write

$$\int_{\Omega} d\mathbf{r}\Phi' = \int_{\cup_j U'_j} d\mathbf{r}\Phi' = \sum_j \int_{U'_j} d\mathbf{r}\Phi' = \sum_j \int_{U'_j \cap U_j} d\mathbf{r}\Phi' + \sum_{j \neq k} \int_{U'_j \cap U_k} d\mathbf{r}\Phi' \quad (\text{D.7})$$

Upon interchanging the roles of primed and unprimed variables in (D.7) and subtracting the result from (D.7)

$$\begin{aligned} & \sum_j \int_{U_j \cap U'_j} d\mathbf{r} [\Phi' - \Phi] + \sum_{j \neq k} \int_{U'_j \cap U_k} d\mathbf{r} [\Phi' - \Phi] = \\ & \sum_j \int_{U_j} d\mathbf{r} [\Phi' - \Phi] - \sum_j \int_{U_j \setminus (U_j \cap U'_j)} d\mathbf{r} [\Phi' - \Phi] + \sum_{j \neq k} \int_{U'_j \cap U_k} d\mathbf{r} [\Phi' - \Phi] \end{aligned} \quad (\text{D.8})$$

Apparently, the areas of integration domains of second and third integral terms of (D.8) scale as ds , and, due to continuity of Φ , so does $\Phi' - \Phi$. Consequently, re-inserting the definition of Φ into (D.8) we find

$$\sum_j s_j \mathbf{f}_j = \sum_j \int_{U_j} d\mathbf{r} \partial_{\mathbf{s}_i} V(\mathbf{r}, \{\mathbf{s}_k\}) \rho_0(\mathbf{r}) \quad (\text{D.9})$$

We shall decompose U_j as a (disjoint) union of two sets T_j and $U_j \setminus T_j$ that contain points whose closest point on domain boundary $\partial\Omega$ is \mathbf{s}_j and those whose closest point in $\partial\Omega$ lies on one of the edges, adjacent to \mathbf{s}_j respectively. (D.9) reads:

$$\sum_j s_j \mathbf{f}_j = \sum_j \int_{T_j} d\mathbf{r} \partial_{\mathbf{s}_i} V(\mathbf{r}, \{\mathbf{s}_k\}) \rho_0(\mathbf{r}) + \sum_j \int_{U_j \setminus T_j} d\mathbf{r} \partial_{\mathbf{s}_i} V(\mathbf{r}, \{\mathbf{s}_k\}) \rho_0(\mathbf{r}) \quad (\text{D.10})$$

But in T_j (according to its definition) $V(\mathbf{r}, \{\mathbf{s}_k\}) = V(\|\mathbf{r} - \mathbf{s}_j\|)$, and hence the first term in the right hand side of (D.10) reduces to $\sum_i \int_{T_i} d\mathbf{r} \partial_{\mathbf{s}_i} V(\|\mathbf{r} - \mathbf{s}_i\|) \rho_0(\mathbf{r}) = -\sum_i \int_{T_i} d\mathbf{r} \nabla_{\mathbf{r}} V(\|\mathbf{r} - \mathbf{s}_i\|) \rho_0(\mathbf{r})$. The second term on the right hand side of (D.10) simplifies to

$$\sum_i \int_{U_i \setminus T_i} d\mathbf{r} \rho_0(\mathbf{r}) [\partial_{\mathbf{s}_i} + \partial_{\mathbf{s}_{i'}}] V(\mathbf{r}, \{\mathbf{s}_k\}) \quad (\text{D.11})$$

where \mathbf{s}_i and $\mathbf{s}_{i'}$ are the vertices spanning to edge, containing the closest point to \mathbf{r} in $\partial\Omega$. Somewhat lengthy but straightforward explicit calculation shows that $[\partial_{\mathbf{s}_i} + \partial_{\mathbf{s}_{i'}}] V(\mathbf{r}) = -\nabla_{\mathbf{r}} V(\mathbf{r})$ which together with (D.9), (D.10) and (D.11) gives

$$\begin{aligned} \sum_i s_i \mathbf{f}_i &= - \sum_i \int_{T_i} d\mathbf{r} \rho_0(\mathbf{r}) \nabla V(\mathbf{r}) - \sum_i \int_{U_i \setminus T_i} d\mathbf{r} \rho_0(\mathbf{r}) \nabla V(\mathbf{r}) = \\ &= - \sum_i \int_{U_i} d\mathbf{r} \rho_0(\mathbf{r}) \nabla V(\mathbf{r}) = - \int d\mathbf{r} \rho_0(\mathbf{r}) \nabla V(\mathbf{r}) \end{aligned} \tag{D.12}$$

i.e. force balance (D.5) holds.

E Integrating the membrane dynamics

In this section we describe the algorithm that we used to numerically integrate the dynamics of the moving boundary, Sec. 6.4. To this end we shall need explicit expressions for force density at the boundary due to (i) bending and stretching of the membrane, (ii) external pressure, and (iii) boundary-filament interactions as well as a couple of useful subroutines.

E.1 Force density at the boundary

We start by noting that total force density at the boundary comprises two contributions: one associated with the fictitious potential that captures membrane-filament interactions \mathcal{F}_f and the one due to membrane deformations \mathcal{F}_h . The latter comprises bending energy, surface tension, and external pressure:

$$\mathcal{F}_h = pV + \tau S + \kappa \int (H^2/2) dS \quad (\text{E.1})$$

Here, p is pressure, V is vesicle volume, τ is membrane surface tension, κ is bending modulus and $H^2/2$ is mean square curvature of the membrane. The boundary Γ is assumed to enclose a simply-connected domain, whose boundary is approximated by a polygon with vertices \mathbf{s}_i . The index i increases in the counter-clockwise direction. Then, the discretized force density at vertex i is determined by

$$\mathbf{f}_i = \frac{\delta \mathcal{F}}{\delta \Gamma} \frac{1}{s_i} \frac{\partial (\mathcal{F}_f + \mathcal{F}_h)}{\partial \mathbf{s}_i} \quad (\text{E.2})$$

For later convenience, we shall introduce the following quantities:

$$\begin{aligned} v_{i+1} &= \|\mathbf{s}_{i+1} - \mathbf{s}_i\| = \sqrt{(s_{i+1}^x - s_i^x)^2 + (s_{i+1}^y - s_i^y)^2} \\ v_{i-1} &= \|\mathbf{s}_i - \mathbf{s}_{i-1}\| = \sqrt{(s_i^x - s_{i-1}^x)^2 + (s_i^y - s_{i-1}^y)^2} \\ s_i &= \frac{v_{i+1} + v_{i-1}}{2} \end{aligned} \quad (\text{E.3})$$

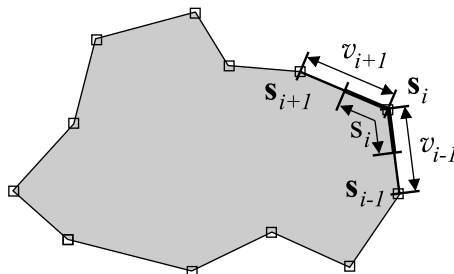


Figure 47: Schematic explanation of the notation in the text.

Here, $v_{i\pm 1}$ are the lengths of the edges adjacent to vertex i , whereas s_i is the length of the boundary element, corresponding to the respective vertex, which defined as half of the sum of lengths of the adjacent edges, see Fig. 47. Discretized expressions for the three contributions to the membrane free energy \mathcal{F}_h in (E.1) are

$$V \simeq \frac{1}{2} \left(\frac{s_{i+1}^x + s_i^x}{2} \right) (s_{i+1}^y - s_i^y) + \frac{1}{2} \left(\frac{s_{i+1}^y + s_i^y}{2} \right) (s_i^x - s_{i-1}^x) \quad (\text{E.4})$$

$$S \simeq \sum_i s_i \quad (\text{E.5})$$

$$\begin{aligned} H^2 \simeq & \frac{1}{s_{i-1}} \left[\left\{ \frac{s_i^x - s_{i-1}^x}{v_{i-1}} - \frac{s_{i-1}^x - s_{i-2}^x}{v_{i-2}} \right\}^2 + \left\{ \frac{s_i^y - s_{i-1}^y}{v_{i-1}} - \frac{s_{i-1}^y - s_{i-2}^y}{v_{i-2}} \right\}^2 \right] + \\ & \frac{1}{s_i} \left[\left\{ \frac{s_{i+1}^x - s_i^x}{v_{i+1}} - \frac{s_i^x - s_{i-1}^x}{v_{i-1}} \right\}^2 + \left\{ \frac{s_{i+1}^y - s_i^y}{v_{i+1}} - \frac{s_i^y - s_{i-1}^y}{v_{i-1}} \right\}^2 \right] + \\ & \frac{1}{s_{i+1}} \left[\left\{ \frac{s_{i+2}^x - s_{i+1}^x}{v_{i+2}} - \frac{s_{i+1}^x - s_i^x}{v_{i+1}} \right\}^2 + \left\{ \frac{s_{i+2}^y - s_{i+1}^y}{v_{i+2}} - \frac{s_{i+1}^y - s_i^y}{v_{i+1}} \right\}^2 \right] \equiv \\ & \frac{1}{s_{i-1}} g_{i-1} + \frac{1}{s_i} g_i + \frac{1}{s_{i+1}} g_{i+1} \end{aligned} \quad (\text{E.6})$$

Expression (E.5) is obvious. Eq. (E.6) is the discrete approximation of the polygon curvature that follows immediately from curvature definition

$$H^2 = \left\| \frac{d\hat{\mathbf{T}}}{ds} \right\|^2, \quad (\text{E.7})$$

where $\hat{\mathbf{T}}(s)$ is unit vector, tangential to the curve, parameterized by the length along the curve s .

Equation (E.4) gives polygon area as a function of coordinates of its vertices. To derive Eq. (E.4) note that

$$\int d\hat{\mathbf{n}} (x\hat{\mathbf{x}} + y\hat{\mathbf{y}}) = \int dS \nabla \cdot (x\hat{\mathbf{x}} + y\hat{\mathbf{y}}) = 2V \quad (\text{E.8})$$

according to Gauss theorem. The line integral on the left-hand side of (E.8) may be approximated as

$$\sum_i (\mathbf{s}_{i+1} - \mathbf{s}_i)^\perp \cdot \left(\frac{\mathbf{s}_{i+1} + \mathbf{s}_i}{2} \right) \quad (\text{E.9})$$

where the second factor approximates the vector in the integrand in the left hand side of (E.8) by its value at the middle of the edge between the vertices \mathbf{s}_i and \mathbf{s}_{i+1} . In the first factor \mathbf{s}^\perp denotes the vector, orthogonal to \mathbf{s} . Equation (E.4) is (E.9), explicitly re-written in terms of the Cartesian coordinates of the polygon vertices.

Total discretized force density (not involving filament-boundary interactions) \mathbf{f}_i at vertex i is determined by

$$s_i \mathbf{f}_i = p \frac{\partial V}{\partial \mathbf{s}_i} + \tau \frac{\partial S}{\partial \mathbf{s}_i} + \frac{\kappa}{2} \frac{\partial \int H^2 dS}{\partial \mathbf{s}_i} \quad (\text{E.10})$$

Left is to specify the expression for the gradients in (E.10) in terms of coordinates of the vertices \mathbf{s}_i . To this end we will use the following derivatives:

$$\begin{aligned} \frac{\partial v_{i\pm 2}}{\partial s_i^{x,y}} &= 0 & \frac{\partial v_{i+1}}{\partial s_i^{x,y}} &= -\frac{s_{i+1}^{x,y} - s_i^{x,y}}{v_{i+1}} & \frac{\partial v_{i-1}}{\partial s_i^{x,y}} &= \frac{s_i^{x,y} - s_{i-1}^{x,y}}{v_{i-1}} \\ \frac{\partial s_i}{\partial s_i^{x,y}} &= \frac{1}{2} \left\{ \frac{s_i^{x,y} - s_{i+1}^{x,y}}{v_{i+1}} + \frac{s_i^{y,x} - s_{i-1}^{y,x}}{v_{i-1}} \right\} \end{aligned} \quad (\text{E.11})$$

Force density contribution due to bending is determined from $\partial \int H^2 dS / \partial \mathbf{s}_i$:

$$\partial_{s_i^{x,y}} \int H^2 dS = \sum_{j=i-1}^{i+1} -s_j^{-2} \frac{\partial s_j}{\partial s_j^{x,y}} g_j^{x,y} + \frac{1}{s_j} \partial g_j / \partial s_i^{x,y} \quad . \quad (\text{E.12})$$

Explicitly

$$\begin{aligned}
\partial g_i / \partial s_i^{x,y} &= 2 \left\{ \frac{s_{i+1}^{x,y} - s_i^{x,y}}{v_{i+1}} - \frac{s_i^{x,y} - s_{i-1}^{x,y}}{v_{i-1}} \right\} \times \\
&\left(\frac{-v_{i+1} - (s_{i+1}^{x,y} - s_i^{x,y}) \frac{\partial v_{i+1}}{\partial s_i^{x,y}}}{v_{i+1}^2} - \frac{v_{i-1} - (s_i^{x,y} - s_{i-1}^{x,y}) \frac{\partial v_{i-1}}{\partial s_i^{x,y}}}{v_{i-1}^2} \right) \\
\partial g_{i+1} / \partial s_i^{x,y} &= 2 \left\{ \frac{s_{i+2}^{x,y} - s_{i+1}^{x,y}}{v_{i+2}} - \frac{s_{i+1}^{x,y} - s_i^{x,y}}{v_{i+1}} \right\} \left(\frac{-v_{i+1} - (s_{i+1}^{x,y} - s_i^{x,y}) \frac{\partial v_{i+1}}{\partial s_i^{x,y}}}{v_{i+1}^2} \right) \\
\partial g_{i-1} / \partial s_i^{x,y} &= 2 \left\{ \frac{s_i^{x,y} - s_{i-1}^{x,y}}{v_{i-1}} - \frac{s_{i-1}^{x,y} - s_{i-2}^{x,y}}{v_{i-2}} \right\} \left(\frac{v_{i-1} - (s_i^{x,y} - s_{i-1}^{x,y}) \frac{\partial v_{i-1}}{\partial s_i^{x,y}}}{v_{i-1}^2} \right)
\end{aligned} \tag{E.13}$$

The force density contribution due to stretching is determined from $\partial S / \partial \mathbf{s}_i$:

$$\partial_{s_i^{x,y}} S = \left\{ \frac{s_{i+1}^{x,y} - s_i^{x,y}}{v_{i+1}} + \frac{s_i^{x,y} - s_{i-1}^{x,y}}{v_{i-1}} \right\} \tag{E.14}$$

Finally, the contribution due to expansion against the external pressure is determined from $\partial V / \partial \mathbf{s}_i$:

$$\partial_{s_i^x} V = \frac{1}{2} (s_{i+1}^y - s_{i-1}^y) \quad \partial_{s_i^y} V = \frac{1}{2} (s_{i-1}^x - s_{i+1}^x) \tag{E.15}$$

In summary, the "passive contribution" to force density at a vertex as a function of vertex coordinates is explicitly given by (E.10)-(E.15).

Now consider the force contribution due to filaments treadmilling against the boundary surface. We assume that the density of the filament tips ρ (as well as all other relevant concentrations) is specified on a 2-dimensional grid with vertices, indexed by (j, k) , having cartesian coordinates $\mathbf{r}_{j,k} = (j\Delta_x, k\Delta_y)$. In the simulations, we used the same lattice spacing for both, x and y , coordinates, i.e. $\Delta_x = \Delta_y = \Delta$. The discrete approximation of the total energy that corresponds to the fictitious potential, confining the filaments is

$$\mathcal{F}_f = \sum_{j,k} \rho_{jk} H(d(\mathbf{r}_{j,k})) \quad , \tag{E.16}$$

where $d(\mathbf{r}_{i,j})$ is the signed distance from $\mathbf{r}_{j,k}$ to the boundary (henceforth denoted by Γ), H is a sigmoidal function, parameterizing the potential step at the boundary (see App. D), $\rho_{j,k}$ is the discretized density of the filament tips at $d(\mathbf{r}_{i,j})$.

We shall now derive the contribution to force density due to treadmilling filaments, given by $s_i^{-1} \partial \delta \mathcal{F}_f / \partial \mathbf{s}_i$. As has already been mentioned in Appendix D, the set U of grid points $\mathbf{r}_{j,k}$ may be subdivided into two sets, see Fig. 48. One set, T , contains the points whose closest point at the boundary is one of the vertices. Its complement, $U \setminus T$, contains the points, whose closest point on the boundary is on one of the

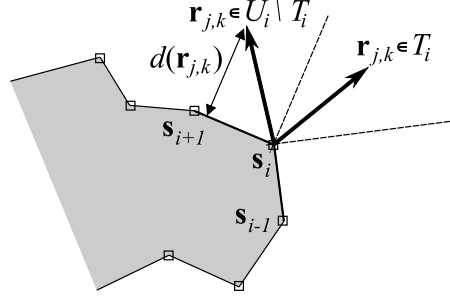


Figure 48: Illustration of the two possible expressions for the distance to the boundary, see text.

edges. Let us introduce the following notation. U_i shall denote the set of points $\{\mathbf{r}_{j,k}\}$ whose closest point on the boundary Γ is on one of the two edges, adjacent to vertex i (possibly, the vertex itself). T_i are points whose closest point is vertex i . For $\mathbf{r}_{i,j} \in T_i$ the distance to Γ is $d(\mathbf{r}_{i,j}) = \|\mathbf{r}_{j,k} - \mathbf{s}_i\|$. In this case

$$\nabla_{\mathbf{s}_i} d(\mathbf{r}_{j,k}) = (\mathbf{s}_i - \mathbf{r}_{j,k}) / d(\mathbf{r}_{j,k}) \quad (\text{E.17})$$

For $\mathbf{r}_{j,k} \in U_i \setminus T_i$ the distance to Γ is the length of the line, perpendicular to one of the edges, adjacent to vertex i , through $\mathbf{r}_{j,k}$. This equals the scalar product of $\mathbf{r}_{j,k} - \mathbf{s}_i$ with a unit vector, perpendicular to one of the edges, adjacent to \mathbf{s}_i . Explicitly, the signed distance from Γ to \mathbf{s}_i is

$$d(\mathbf{r}_{j,k}) = \left\{ (r_{j,k}^x - s_i^x) (s_{i+1}^y - s_i^y) + (r_{j,k}^y - s_i^y) (s_i^x - s_{i+1}^x) \right\} \frac{1}{v_{i+1}} \equiv h_{i+1} / v_{i+1} \quad (\text{E.18})$$

if the closest point is on the edge, spanned by the vertices i and $i + 1$, see Fig. 48. In this case

$$\begin{aligned} \partial_{s_i^x} d(\mathbf{r}_{j,k}) &= -h_{i+1} \frac{1}{v_{i+1}^2} \frac{\partial v_{i+1}}{\partial s_i^x} + \frac{1}{v_{i+1}} (r_{j,k}^y - s_{i+1}^y) \\ \partial_{s_i^y} d(\mathbf{r}_{j,k}) &= -h_{i+1} \frac{1}{v_{i+1}^2} \frac{\partial v_{i+1}}{\partial s_i^y} + \frac{1}{v_{i+1}} (s_{i+1}^x - r_{j,k}^x) \quad . \end{aligned} \quad (\text{E.19})$$

If the closest edge is spanned by the vertices i and $i - 1$, than

$$\begin{aligned} d(\mathbf{r}_{j,k}) &= \left\{ (r_{j,k}^x - s_i^x) (s_i^y - s_{i-1}^y) + (r_{j,k}^y - s_i^y) (s_{i-1}^x - s_i^x) \right\} \frac{1}{v_{i+1}} \\ &\equiv h_{i-1} / v_{i-1} \quad , \end{aligned} \quad (\text{E.20})$$

see Fig. 48. In this case

$$\begin{aligned}\partial_{s_i^x} d(\mathbf{r}_{j,k}) &= -h_{i-1} \frac{1}{v_{i-1}^2} \frac{\partial v_{i-1}}{\partial s_i^x} + \frac{1}{v_{i-1}} (s_{i-1}^y - r_{j,k}^y) \\ \partial_{s_i^y} d(\mathbf{r}_{j,k}) &= -h_{i-1} \frac{1}{v_{i-1}^2} \frac{\partial v_{i-1}}{\partial s_i^y} + \frac{1}{v_{i-1}} (r_{j,k}^x - s_{i-1}^x) \quad .\end{aligned}\tag{E.21}$$

The components of force density \mathbf{f}_i at vertex i , due to treadmilling filaments is determined by $\nabla_{\mathbf{s}_i} \mathcal{F}_f$:

$$\begin{aligned}s_i f_i^{x,y} = \partial_{s_i^{x,y}} \mathcal{F}_f &= \sum_{\mathbf{r}_{j,k} \in U_i} \rho_{j,k} \partial_{s_i^{x,y}} d(\mathbf{r}_{j,k}) = \sum_{\mathbf{r}_{j,k} \in T_i} \rho_{j,k} \partial_{s_i^{x,y}} d(\mathbf{r}_{j,k}) + \\ &\quad \sum_{\mathbf{r}_{j,k} \in U_i \setminus T_i} \rho_{j,k} \partial_{s_i^x} d(\mathbf{r}_{j,k})\end{aligned}\tag{E.22}$$

Equation (E.22), together with Eqs. (E.17), (E.19), and (E.21) gives the force density due to treadmilling filaments at each vertex in terms of filament plus end density and the coordinates of the boundary vertices.

E.2 Three subroutines

Before giving the algorithm for integrating time-evolution of the moving boundaries, we shall describe three important subroutines it comprises.

E.2.1 Subroutine *closest_distance*

Thus far we have seen that in order to evaluate the force density at the boundary one needs to know the signed distances $d(\mathbf{r}_{j,k})$ from every point of the grid $\mathbf{r}_{j,k}$ to the boundary Γ . The subroutine *closest_distance* evaluates the closest distance transform, i.e. the distance from grid points $\mathbf{r}_{j,k}$ to the polygon, parameterized by the vertices \mathbf{s}_i . A "brute force" approach would involve looping through all boundary points for every grid point. A much more efficient algorithm (used in all simulations) is described in Ref. [55].

E.2.2 Subroutine *remesh*

In the course of the time-evolution of the coordinates of the boundary vertices $\{\mathbf{s}_i\}$, the distances between two subsequent vertices may change. Indeed, there is no energy penalty, associated with the merging of vertices,

since the energy of the membrane can not possibly depend on the choice of its parameterization. However, numerical integration of boundary dynamics turns unstable if adjacent vertices come too close. This problem may be overcome by remeshing the boundary in every time step. That is, one can determine the total length of the boundary L (sum of the edge lengths) and move edge i to the point on the boundary, whose distance from vertex 1, measured along the boundary, is iL/N (N being the number of boundary points). This remeshing procedure, however, systematically decreases the area of convex polygons. To avoid this artificial decrease in the area one can scale the polygon slightly upon remeshing so as to keep its area unchanged. Subroutine *remesh* redistributes the vertices along the length of the boundary so as to make any two subsequent vertices equidistant and scales the polygon slightly, to keep the volume.

E.2.3 Subroutine *shift*

If the center of mass of the polygon ("boundary interior") drifts, the polygon might eventually start to cross the boundary of the grid, on which the density of filaments (and those of other molecule types) is defined. In principle, this is not a problem since boundary conditions in our simulation are invariably periodic. However, implementing such a situation might be rather tedious. A simple way around this difficulty is to resort to the coordinate frame, co-moving with the center of mass of the polygon. In practice, one simply shifts the vesicle to the center of the integration domain every now and then. However, as doing so, the length of these shifts can not be made a multiple of grid spacing Δ , the shifts will lead to numerical diffusion, contributing to numerical error.

Here is a way to shift the grid, avoiding numerical diffusion. Suppose the length of the domain is $L = N\Delta$. Suppose the mass center of the vesicle has just advanced more than m grid points in the positive x -direction. Instead of shifting the vesicle, one can shift the grid, see Fig. 49. This is done by increasing the x -coordinates of grid points (j, k) by $m\Delta$, at the same time changing the value of density $\rho_{j,k}$ at the corresponding grid point to $\rho_{j+m,k}$. If $j + m > N$ for some j , the density value at the corresponding point is set to $\rho_{j+m-N+1}$ (since the domain is periodic). In this way, the length of domain shift ($= m\Delta$) is necessarily a multiple of Δ , and does not contribute to numerical diffusion. Shifting the grid by m lattice spacings in this way is implemented in the subroutine *shift*.

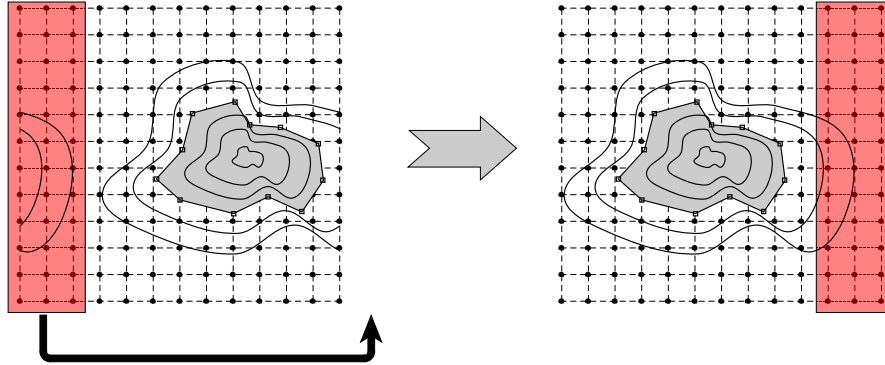


Figure 49: Illustration of the *shift* subroutine. If the vesicle (gray polygon) shifts too far to the right, the leftmost grid points are concatenated at the right domain edge. Black circles are the grid points. Smooth full lines are the level curves of the filament density distribution.

E.3 The algorithm

We are now in position give the algorithm for for integrating the dynamics of the moving boundary.

for i from 0 to ∞ // loop time steps

Call *closest_distance* to compute $d(\mathbf{r}_{i,j})$ at every grid point $\mathbf{r}_{i,j}$

Use the result to compute the potential as $H[d(\mathbf{r}_{i,j})]$

Compute the force density at the boundary due to filaments from $\rho_{i,j}$, vertex coordinates $\{\mathbf{s}_i\}$ from the previous iteration as well as $d(\mathbf{r}_{i,j})$ from *closest_distance*

Compute the force density contributions, not involving filament density from vertex coordinates $\{\mathbf{s}_i\}$ from the previous iteration

Add the two force density contribution, to obtain the total force density \mathbf{f}_i

Update coordinates of the vertices \mathbf{s}_i to $\mathbf{s}_i + dt \mathbf{f}_i / \zeta$, ζ is edge mobility

Call *remesh*

If mass-center shifted more than m grid points away from the center of the current grid, update the grid by calling *shift*

Update all densities, according to the finite difference scheme

endfor

References

- [1] B. Alberts, A. Johnson, J. Lewis, M. Raff, K. Roberts, and P. Walter. *Molecular Biology of the Cell*. Garland, New York, 4th edition, 2002.
- [2] I. Aranson and L. Tsimring. Pattern formation of microtubules and motors: inelastic interaction of polar rods. *Phys. Rev. E.*, 71:050901(R), 2005.
- [3] I. Aranson and L. Tsimring. Theory of self-assembly of microtubules and motors. *Phys. Rev. E.*, 74:031915, 2006.
- [4] B. P. Belousov. A periodic reaction and its mechanism, in *Collection of short papers on radiation medicine for 1958*, Med. Publ., Moscow, 1959.
- [5] H. Benard. Les tourbillons cellulaires dans une nappe liquide. *Rev. Gen. Sci. Pures Appl.*, 11:12611271 and 13091328, 1900.
- [6] C. Beta. private communication.
- [7] R. B. Bird, C. F. Curtiss, R. C. Armstrong, and O. Hassager. *Dynamics of Polymeric Liquids*. Wiley-Interscience, New York, 2nd edition, 1989.
- [8] D. Bray. *Cell Movements: From Molecules to Motility*. Garland, New York, 2nd edition, 2001.
- [9] N. Brilliantov and T. Pöschel. *Kinetic Theory of Granular Gases*. Oxford University Press, USA, 2004.
- [10] N. Carter and R. Cross. Mechanics of the kinesin step. *Nature*, 435:308-312, 2005.
- [11] E. Cytrinbaum, V. Rodionov, and A. Mogilner. Computational model of dynein-dependent self-organization of microtubule asters. *J. Cell Sci.*, 117:1381-1397, 2004.
- [12] P. G. de Gennes and J. Prost. *The Physics of Liquid Crystals*. Clarendon Press, Oxford, 2nd edition, 1993.

- [13] S. R. de Groot and P. Mazur. *Non-Equilibrium Thermodynamics*. Dover Publications, New York, 1984.
- [14] Dictybase. <http://dictybase.org/>
- [15] M. Dogterom, A. Maggs, and S. Leibler. Diffusion and formation of microtubule asters: Physical processes versus biochemical regulation. *Proc. Natl. Acad. USA*, 92:6683-6688, 1995.
- [16] M. Dogterom and B. Yurke. Measurement of the force-velocity relation for growing microtubules. *Science*, 278:856, 1997.
- [17] H.-G. Döbereiner, B. Dubin-Thaler, G. Giannone, H. Xenias, and M. Sheetz. Dynamic phase transitions in cell spreading. *Phys. Rev. Lett.*, 93:108105, 2004.
- [18] H.-G. Döbereiner, B. Dubin-Thaler, J. Hofman, H. Xenias, T. Sims, G. Giannone, M. Dustin, C. Wiggins, and M. Sheetz. Lateral membrane waves constitute a universal dynamic pattern of motile cells. *Phys. Rev. Lett.*, 97:038102, 2006.
- [19] M. Doi and S. F. Edwards. *The Theory of Polymer Dynamics (International Series of Monographs on Physics)*. Oxford University Press, USA (November 24, 1988).
- [20] U. Euteneuer and M. Schliwa. Persistent, directional motility of cells and cytoplasmic fragments in the absence of microtubules. *Nature*, 310:58-61, 1984.
- [21] D. J. Evans and G. P. Morriss. *Statistical Mechanics of Nonequilibrium Liquids*. Academic Press, 1990.
- [22] G. Giannone, B. Dubin-Thaler, H.-G. Döbereiner, N. Kieffer, A. Bresnick and M. Sheetz. Periodic lamellipodial contractions correlate with rearward actin waves. *Cell*, 116:431-443, 2004.
- [23] G. Giannone, B. Dubin-Thaler, O. Rossier, Y. Cai, O. Chaga, G. Jiang, W. Beaver, H.-G. Döbereiner, Y. Freund, G. Borisy, and M. Sheetz. Lamellipodial actin mechanically links myosin activity with adhesion-site formation. *Cell*, 128:561575, 2007.

- [24] I. Gibbons. Chemical dissection of cilia. *Arch. Biol. (Liege)*, 76:317-352, 1965.
- [25] F. Gittes, B. Mickey, J. Nettleton, and J. Howard. Flexural rigidity of microtubules and actin filaments measured from thermal fluctuations in shape. *J. Cell Biol.*, 120:923, 1993.
- [26] S. Günther and K. Kruse. Spontaneous waves in muscle fibres. *New J. Phys.*, 9:417, 2007.
- [27] M. L. Gupta Jr., P. Carvalho, D. M. Roof and D. Pellman. Plus end-specific depolymerase activity of Kip3, a kinesin-8 protein, explains its role in positioning the yeast mitotic spindle. *Nature Cell Biology*, 8:913-923, 2006.
- [28] T. L. Hill. *Linear Aggregation Theory in Cell Biology* (Springer-Verlag, New York, 1987).
- [29] N. Hirokawa, L. G. Tilney, K. Fujiwara, and J. E. Heuser. Organization of actin, myosin, and intermediate filaments in the brush border of intestinal epithelial cells. *J. Cell. Biol.* 91:425-443, 1981.
- [30] J. Howard. *Mechanics of motor proteins and the cytoskeleton*. Sinauer Associates, Sunderland, 2001.
- [31] M. Hrabe de Angelis, J. McIntyre, and A. Gossler. Maintenance of somite borders in mice requires the Delta homologue DII1. *Nature* 386:717-721, 1997.
- [32] A. Hunt, F. Gittes, and J. Howard. The force exerted by a single kinesin molecule against a viscous load. *Biophys. J.*, 67:766-781, 1994.
- [33] H. E. Huxley. The double array of filaments in cross-striated muscle. *J. Biophys. Biochem. Cytol.*, 3:631, 1957.
- [34] H. Isambert, P. Venier, A. C. Maggs, A. Fattoum, R. Kassab, D. Pantaloni, and M. F. Carrier. Flexibility of actin filaments derived from thermal fluctuations. Effect of bound nucleotide, phalloidin, and muscle regulatory proteins. *J. Biol. Chem.*, 270:11437, 1995.

- [35] J.-F. Joanny, F. Jülicher, K. Kruse, and J. Prost. Hydrodynamic theory for multi-component active polar gels. *New J. Phys.*, 9:422, 2007.
- [36] E. Kant. *Kritik der reinen Vernunft*, 1971. http://gutenberg.spiegel.de/?id=5&xid=1368&kapitel=1#gb_found
- [37] R. H. Kessin. *Dictyostelium: evolution, cell biology, and the development of multicellularity (Developmental and Cell Biology Series)* Cambridge University Press; 1 edition (January 15, 2001).
- [38] T. Killich, P. Plath, X. Wei, H. Bultmann, L. Rensing, M. Vicker. The locomotion, shape and pseudopodial dynamics of unstimulated *Dictyostelium* cells are not random. *J. Cell Science*, 106:1005-1013, 1993.
- [39] T. Killich, P. Plath, X. Wei, E. Hass, H. Bultmann, L. Rensing, M. Vicker. Cell movement and shape are non-random and determined by intracellular, oscillatory and rotating waves in *Dictyostelium discoideum*. *Bio Systems*, 33:75-87, 1994.
- [40] T. E. Kreis and R. D. Vale. *Guidebook to the Cytoskeletal and Motor Proteins*. Oxford University Press, Oxford, 2nd edition, 1999.
- [41] P. Kropotkin. *Mutual Aid: A Factor of Evolution* (1902). http://dwardmac.pitzer.edu/Anarchist_Archives/kropotkin/mutaidcontents.html
- [42] K. Kruse, J. F. Joanny, F. Jülicher, J. Prost, and K. Sekimoto. Generic theory of active polar gels: a paradigm for cytoskeletal dynamics. *Eur. Phys. J. E*, 16:5, 2005.
- [43] K. Kruse, J.-F. Joanny, F. Jülicher, and J. Prost. Contractility and retrograde flow in lamellipodium motion. *Phys. Biol.*, 3:130-137, 2006.
- [44] K. Kruse, J. F. Joanny, F. Jülicher, J. Prost, and K. Sekimoto. Asters, vortices, and rotating spirals in active gels of polar filaments. *Phys. Rev. Lett.*, 92:078101, 2004.

- [45] K. Kruse and F. Jülicher. Actively contracting bundles of polar filaments. *Phys. Rev. Lett.*, 85:1778, 2000.
- [46] K. Kruse and F. Jülicher. Self-organization and mechanical properties of active filament bundles. *Phys. Rev. E*, 67:051913, 2003.
- [47] K. Kruse and F. Jülicher. Dynamics and mechanics of motor-filament systems. *Eur. Phys. J. E*, 20:459-465, 2006.
- [48] J. Lee, A. Ishihara, and K. Jacobson. The fish epidermal keratocyte as a model system for the study of cell locomotion. *Symp. Soc. Exp. Biol.*, 47:73-89, 1993.
- [49] Lauren M. Sompayrac. *How the Immune System Works*. Wiley-Blackwell; 3d edition (March 21, 2008).
- [50] H. Lee and M. Kardar. Macroscopic equations for pattern formation in mixtures of microtubules and molecular motors. *Phys. Rev. E*, 64:056113, 2001.
- [51] T. B. Liverpool and M. C. Marchetti. Instabilities of isotropic solutions of active polar filaments. *Phys. Rev. Lett.*, 90:138102, 2003.
- [52] T. Liverpool and M. Marchetti. Bridging the microscopic and the hydrodynamic in active filament solutions. *Europhys. Lett.*, 69:846, 2005.
- [53] H. Meinhardt and M. Kilinger. A model of pattern formation on the shells of molluscs. *J. Theor. Biol.*, 126:63-89, 1986.
- [54] V. Malikov, A. Kashina, and V. Rodionov. Cytoplasmic dynein nucleates microtubules to organize them into radial arrays in vitro. *Mol. Biol. Cell*, 15:2742-2749, 2004.
- [55] S. Mauch. Doctoral Thesis. <http://www.cacr.caltech.edu/~sean/thesis.pdf>.
- [56] A. Moore and L. Wordeman. The mechanism, function and regulation of depolymerizing kinesins during mitosis. *Trends Cell. Biol.*, 14:537, 2004.

- [57] F. Nédélec. Computer simulations reveal motor properties generating stable antiparallel microtubule interactions. *J. Cell Biol.*, 158:6, 2002.
- [58] F. J. Nédélec, T. Surrey, A. C. Maggs, and S. Leibler. Self-organization of microtubules and motors. *Nature*, 389:305, 1997.
- [59] F. Nédélec, T. Surrey. Dynamics of microtubule aster formation by motor complexes. *C. R. Acad. Sci. Paris t.2, Série IV*, 841-847, 2001.
- [60] A. Oates, R. Ho. Hairy/E(spl)-related (Her) genes are central components of the segmentation oscillator and display redundancy with the Delta/Notch signaling pathway in the formation of anterior segmental boundaries in the zebrafish. *Development*, 129(12):2929-2946, 2002.
- [61] P. Oswald and P. Pieranski. *Nematic and Cholesteric Liquid Crystals: Concepts and Physical Properties Illustrated by Experiments*. Taylor & Francis Group, 2006.
- [62] A. Ott, M. Magnasco, A. Simon, and A. Libchaber. Measurement of the persistence length of polymerized actin using fluorescence microscopy. *Phys. Rev. E*, 48:R1642, 1993.
- [63] N. T. Peters and D. L. Kropf. Kinesin-5 motors are required for organization of spindle microtubules in *Silvetia compressa* zygotes. *BMC Plant Biology*, 6:19, 2006.
- [64] I. Prigogine and G. Nicolis. *Self-Organization in Non-Equilibrium Systems*, Wiley, ISBN 0-471-02401-5, 1977.
- [65] J. Prost, C. Barbetta and J.-F. Joanny. Dynamical control of the shape and size of stereocilia and microvilli. *Biophys. J.*, 93:1124-1133, 2007.
- [66] L. Rayleigh. On convection currents in a horizontal layer of fluid when the higher temperature is on the other Side. *Philos. Mag.*, 32:529-43, 1916.
- [67] V. I. Rodionov and G. G. Borisy. Self-centring activity of cytoplasm. *Nature*, 386:170, 1997.

- [68] V. Rodionov and G. Borisy. Microtubule treadmilling in vivo. *Science*, 275:215, 1997.
- [69] V. Rodionov, A. Hope, T. Svitkina, and G. Borisy. Functional Coordination of Microtubule and Actin Based Motility in Melanophores. *Curr. Biol.*, 8(3):165-168, 1998.
- [70] A. Rzdzinska, M. Schneider, C. Davies, G. Riordan, and B. Kachar. An actin molecular treadmill and myosins maintain stereocilia functional architecture and self-renewal. *J. Cell. Biol.*, 164:887-897, 2004.
- [71] G. Salbreux, J.-F. Joanny, J. Prost, and P. Pullarkat. Shape oscillations of non-adhering fibroblast cells. *Phys. Biol.*, 4:268-284, 2007.
- [72] U. Seifert. Configurations of fluid membranes and vesicles. *Adv. Phys.*, 46:13-137, 1997.
- [73] U. Seifert. Lecture Notes: Physics meets Biology. From Soft Matter to Cell Biology. http://www.theo2.physik.uni-stuttgart.de/institut/seifert/d3_useifert_web.pdf
- [74] T. Surrey, F. Nédélec, S. Leibler, and E. Karsenti. Physical properties determining selforganization of motors and microtubules. *Science*, 292:1167, 2001.
- [75] T. Svitkina, A. Verkhovsky, K. McQuade, and G. Borisy. Analysis of the actin-myosin II system in fish epidermal keratocytes: mechanism of cell body translocation. *J. Cell Biol.*, 139:397, 1997.
- [76] K. Takiguchi. Heavy meromyosin induces sliding movements between antiparallel actin filaments. *J. Biochem. (Tokyo)*, 109:520, 1991.
- [77] K. Takiguchi, H. Hayashi, and E. Kurimoto and S. Higashi-Fujime. *In vitro* motility of skeletal muscle myosin and its proteolytic fragments. *J. Biochem.*, 107:671-679, 1990.
- [78] K. Tawada and K. Sekimoto. Protein friction exerted by motor enzymes through a weak-binding interaction. *J. Theor. Biol.*, 150(2):193-200, 1991.

- [79] S. Toba, T. Watanabe, L. Yamaguchi-Okimoto, Y. Toyashima, and H. Higuchi. Overlapping hand-over-hand mechanism of single molecular motility of cytoplasmic dynein. *Proc. Natl. Acad. Sci. USA*, 103:5741-5745, 2006.
- [80] M. Tomishige and R. Vale. Conversion of Unc104/KIF1A kinesin into a processive motor after dimerization. *Science*, 297:2263-2267, 2002.
- [81] J. Toner, Y. Tu and S. Ramaswamy. Hydrodynamics and phases of flocks. *Ann. Phys.*, 318:170, 2005.
- [82] A. M. Turing. The Chemical Basis of Morphogenesis, *Philosophical Transactions of the Royal Society B (London)*, 237:37-72, 1952.
- [83] P. Umbanhowar, F. Melo and H. Swinney. Localized excitations in a vertically vibrated granular layer. *Nature*, 382:793-796, 1996.
- [84] R. D. Vale, T. S. Reese, and M. P. Sheetz. Identification of a novel force-generating protein, kinesin, involved in microtubule-based motility. *Cell*, 42:39, 1985.
- [85] P. Venier, A. C. Maggs, M. F. Carrier, and D. Pantaloni. Analysis of microtubule rigidity using hydrodynamic flow and thermal fluctuations. *J. Biol. Chem.*, 269:13353, 1994.
- [86] A. Verkhovsky, T. Svitkina, and G. Borisy. Self-polarization and directional motility of cytoplasm. *Curr. Biol.*, 9:11, 1999.
- [87] A. Verkhovsky, T. Svitkina, and G. Borisy. Polarity sorting of actin filaments in cytochalasin-treated fibroblasts. *J. Cell. Sci.*, 110:1693-1704, 1997.
- [88] M. Vicker. F-actin assembly in Dictyostelium cell locomotion and shape oscillations propagates as a self-organized reaction-diffusion wave. *FEBS Letters*, 510:5-9, 2002.
- [89] M. Vicker. Reaction-diffusion waves of actin filament polymerization-depolymerization in Dictyostelium pseudopodium extension and cell locomotion. *Biophysical Chemistry*, 84:87-98, 2000.

- [90] I. Vorobjev, V. Malikov, and V. Rodionov. Self-organization of a radial microtubule array by dynein-dependent nucleation of microtubules. *Proc. Natl. Acad. Sci. USA*, 98:10160, 2001.
- [91] O. Weiner, W. Marganski, L. Wu, S. Altschuler, and M. Kirschner. An actin-based wave generator organizes cell motility. *PLoS Biol.*, 5:e221, 2007.
- [92] A. M. Zhabotinsky. Periodical oxidation of malonic acid in solution (a study of the Belousov reaction kinetics), *Biofizika*, 9:306-11, 1964.
- [93] A. M. Zhabotinsky and A. N. Zaikin. Autowave processes in a distributed chemical system, *J. Theor. Biol.*, 40:45-61, 1973.
- [94] F. Ziebert and W. Zimmermann. Nonlinear competition between asters and stripes in filament-motor systems. *Eur. Phys. J. E*, 18:41-54, 2005.
- [95] F. Ziebert and W. Zimmermann. Pattern formation driven by nematic ordering of assembling biopolymers. *Phys. Rev. E*, 70:022902, 2004.
- [96] F. Ziebert and W. Zimmermann. Comment on "Instabilities of Isotropic Solutions of Active Polar Filaments", *Phys. Rev. Lett.* 93:159802, 2004.
- [97] A. Zumdick, M. Cosentino Lagomarsino, C. Tanase, K. Kruse, B. Mulder, M. Dogterom, and F. Jülicher. Continuum description of the cytoskeleton: ring formation in the cell cortex. *Phys. Rev. Lett.*, 95:258103, 2005.

Acknowledgements

First of all I thank my supervisor Prof. Dr. Kartsen Kruse who introduced me to the coarse-grained mean-field descriptions of the cytoskeleton.

Furthermore, I thank the people of our research group for a pleasant working environment. In particular, I shall like to thank Stefan Günther for the German translation of the abstract.

Finally, I shall like to express my gratitude to the people of the MPI-PKS biophysics group of Prof. Frank Jülicher.